UCLouvain

École polytechnique de Louvain

U-shaped Reinforced Concrete Walls with Shape Memory Alloys

Large Scale Tests on LNEC-3D Shake Table and Numerical Modelling

Author: **Basile Payen**
Supervisors: **João Pacheco de Almeida, António Correia, Ryan Hoult**
Readers: **Catherine Doneux, Dan Palermo**
Academic year 2022–2023
Master [120] in Civil Engineering

Abstract

In the pursuit of advancing our understanding of concrete structure behavior during seismic events and mitigating potential construction pitfalls, the necessity for extensive large-scale experimental tests becomes evident.

This master thesis aims to numerically analyse the behavior of two walls that will be tested in a European project denoted ALL4wALL. The two walls of 40 tons and more than 6 m high will be subjected to dynamic loading on the shake table at LNEC in Lisbon. The first wall, UWS1, is designed according to the Eurocode 8 using RC, and the second unit, UWS2, is the exact similar wall, except that the bottom boundary regions of the wall will contain shape memory alloy (SMA), a superelastic material. The primary objective of this experimental campaign is to investigate the impact of SMA in reducing residual displacement and analyse the torsional response of U-shaped walls under bidirectional dynamic loading.

To numerically simulate the behavior of these walls, beam-truss modelling was employed and validated according to many previous experimental testing of quasi-static and dynamic planar or non-planar walls. The results of this model validation demonstrated a generally accurate representation of the walls' behavior despite some challenges regarding the influence of the top of the wall on torsion and the inaccurate material model of SMA.

This results in modelling and predicting the behavior of UWS1 and UWS2 units under many static and dynamic loading. The inclusion of SMA indeed led to a notable reduction in residual displacement. An analysis of the influence of the position of the masses was also concluding with a reduction of the residual and maximal displacement. These results will have to be validated with the forthcoming results of the ALL4wALL experimental campaign.

Acknowledgements

This master would not have been possible without the help of certain individuals.

I would like to express my sincere gratitude to my three supervisors, João Almeida, António Correia, and Ryan Hoult, for their invaluable guidance and support throughout this journey. In the years to come, it is both an honor and a joy to continue working alongside João and Ryan, thank you for not only sharing your passion in civil engineering but also for spreading your enthusiasm beyond the classroom.

My thanks go to Mathis Keirle and Christophe Saegerman for their assistance with beam-truss modelling.

Special thanks to Lucie Deconninck for her meticulous proofreading and unwavering encouragement.

Last but certainly not least, I extend my gratitude to my family and for their motivation and their funny distractions.

Contents

Abstract i

Acknowledgements ii

Table of Contents v

List of Figures ix

List of Tables x

1 Motivation, Objectives and Organization 1
- 1.1 Motivation . . . 1
- 1.2 Objectives and research novelties . . . 2
- 1.3 Organization . . . 3

2 State of the Art and Project All4wAll 4
- 2.1 Project description . . . 4
  - 2.1.1 Eries . . . 4
  - 2.1.2 ALL4wALL . . . 6
  - 2.1.3 Description of the transnational access facility . . . 8
- 2.2 Previous experimental tests . . . 9
  - 2.2.1 Quasi-static tests on U-shaped wall . . . 9
  - 2.2.2 Dynamic tests on U-shaped wall . . . 13
  - 2.2.3 Tests on walls with shape memory alloys . . . 14
- 2.3 Numerical modelling . . . 17
  - 2.3.1 General overview of nonlinear models . . . 18
  - 2.3.2 Beam-Truss Model (BTM) . . . 20
- 2.4 Seismostruct, material models and performance criteria . . . 23
  - 2.4.1 Material models . . . 24
  - 2.4.2 Performance criteria and failure mode . . . 29

3 Model Validation **31**
3.1 Quasi-static cyclic and torsional tests with UW1 and UW2 31
3.1.1 Geometry 32
3.1.2 Material properties 34
3.1.3 BTM results and comparison for UW1 36
3.1.4 BTM results and comparison for UW2 37
3.2 Quasi-static uniaxial and biaxial tests with IR1, IR2 and IR3 39
3.2.1 Geometry 39
3.2.2 Material properties 41
3.2.3 BTM results and comparison for IR1 42
3.2.4 BTM results and comparison for IR2 43
3.2.5 BTM results and comparison for IR3 44
3.3 Quasi-static cyclic test with RC+SMA 46
3.3.1 Geometry 47
3.3.2 Material properties 48
3.3.3 BTM results and comparison 49
3.4 Dynamic tests with CEA1 and CEA3 51
3.4.1 Geometry 51
3.4.2 Material properties 53
3.4.3 Ground motion input 54
3.4.4 BTM results and comparison 55

4 BTM Analysis of ALL4wALL Units **60**
4.1 Units description and test set up 60
4.1.1 Units description 60
4.1.2 Test setup and limitation of the table 65
4.1.3 Instrumentation 67
4.1.4 Loading protocol 67
4.2 Numerical static analysis 71
4.2.1 Static pushover 72
4.2.2 Torsional analysis 75
4.2.3 Cyclic loading 77
4.3 Nonlinear static analysis 80
4.3.1 Bilinearization 80
4.3.2 N2 method and performance point 82
4.4 Dynamic characterization 84
4.5 Nonlinear dynamic analysis 84
4.5.1 Damping model 84
4.5.2 Comparison of dynamic loading with static pushover 85
4.5.3 Dynamic analysis 87
4.5.4 Torsional dynamic analysis 91

4.6 Influence of mass position 92
4.6.1 Static analysis 92
4.6.2 Dynamic analysis 93
4.7 Blind prediction 95
4.7.1 UWS1 prediction 95
4.7.2 UWS2 prediction 96

5 Conclusion and Further Developments **97**

A Literature Experimental Results **100**

B Seismostruct 3D Model **109**

Bibliography **117**

List of Figures

2.1 ERIES logo. 4
2.2 Expected difference for RC and SMA wall from project submission by Almeida et al.. 7
2.3 Picture of the LNEC 3D shake table from the author (29-03-2023). 8
2.4 UW1 unit (a) 3D view [Unit: mm] and (b) picture of the testing campaign, both from Hoult et al. (2023). 10
2.5 Section of the test specimen IR [Unit: mm] from Ile and Reynouard (2005). 11
2.6 Loading protocol of IR3 from Ile and Reynouard (2005). 12
2.7 Elevation plan of CEA walls from Combescure et al. (1999) [Unit: mm]. . 13
2.8 (a) Geometry and reinforcement layout of the two test units, including cross-section close-up. (b) SMA-steel rebar assembly and mechanical coupler photo. (c) Instrumentation with the laser measurement position from Almeida et al. (2020). [Units in mm.] 15
2.9 Bridge geometric details from Noguez and Saiidi (2012). 16
2.10 Side view of the SMA column from Noguez and Saiidi (2012). 17
2.11 Elevation view of stick model for a rectangular cross-section wall from M. Keirle thesis (2022). 18
2.12 Wide column model of (a) coupled walls and of (b) a U-shaped wall from Beyer et al. (2008). 19
2.13 Schematic illustration of (a) a U-shaped wall and (b) its beam-truss model from Hoult et al. (2023). 21
2.14 Representation of the beam-truss model from Hoult et al. (2023). 22
2.15 Representation of the diagonal element in BTM from Hoult et al. (2023). . 22
2.16 Strain-stress relationship of unconfined concrete, numerical model and experimental test. 25
2.17 Strain-stress diagram of confined (1.2) and unconfined concrete model. . . 26
2.18 Strain-stress diagram of steel, numerical model and experimental test. . . . 27
2.19 Strain-stress diagram of SMA, numerical model and experimental test. . . 28

3.1 Cross section and reinforcement of UW1 and UW2 [Unit: mm]. 32
3.2 Plan and elevation views of the beam-truss model of UW1 [Unit: mm]. . . 33
3.3 Plan and elevation views of the beam-truss model of UW2 [Unit: mm]. . . 34

3.4 Force-displacement relationship of UW1, North-South cyclic loading. . . . 36
3.5 Torque-rotation relationship of UW2, torsional cyclic loading. 38
3.6 Cross section and reinforcement of IR [Unit: mm]. 40
3.7 Plan and elevation views of the beam-truss model for IR [Unit: mm]. . . . 41
3.8 Force-displacement relationship of IR1, North-South cyclic loading. 43
3.9 Force-displacement relationship of IR2, East-West cyclic loading. 44
3.10 Force-displacement relationship in North-South direction of IR3, biaxial cyclic loading. 45
3.11 Force-displacement relationship in East-West direction of IR3, biaxial cyclic loading. 45
3.12 Forces in X and Y direction of IR3, biaxial cyclic loading. 46
3.13 Cross section and reinforcement of RC+SMA wall [Unit: mm]. 47
3.14 Plan and elevation views of the beam-truss model for RC+SMA [Unit: mm]. 48
3.15 Force-displacement relationship of RC+SMA unit, quasi-static cyclic loading. 50
3.16 Cross section and reinforcement of CEA1 [Unit: mm]. 51
3.17 Plan and elevation views of the beam-truss model of CEA1 [Unit: mm]. . . 53
3.18 Ground motion (a) from Combescure et al. (1999) and (b) digitized. 55
3.19 Force-displacement relationship of CEA1, pushover from North-to-South and experimental results comparison. 56
3.20 Experimental and simulate force-displacement relationship of CEA1 with test (a) 1, (b) 3, (c) 4 and (d) CEA3 with test 3. 57
3.21 (a) Maximum displacement at 4.14 [m] and (b) maximum base shear for different PGA of CEA1. 58
3.22 (a) Maximum displacement at 4.14 [m] and (b) maximum base shear for different PGA of CEA3. 58

4.1 Three-dimensional elevation view of UWS1 from Blind Prediction - Test description. 61
4.2 Cross section and reinforcement UWS1 and UWS2 [Unit: mm]. 62
4.3 Plan and elevation views of the beam-truss model for UWS1 and UWS2 in red [Unit: mm]. 63
4.4 (a) Elevation view and (b) plan view of the top of the wall of UWS1 and UWS2 from Blind Prediction - Test description [unit: mm]. 66
4.5 Time-acceleration of the HNN ground motion. 68
4.6 Time-acceleration of the HNE ground motion. 69
4.7 Total dynamic loading in the EW direction (HNN). 70
4.8 Total dynamic loading in the NS direction (HNE). 71
4.9 Force-displacement relationship of UWS1, West-to-East pushover. 72
4.10 Force-displacement relationship of UWS1, East-to-West pushover. 72
4.11 Force-displacement relationship of UWS1, North-South pushover. 73
4.12 Force-displacement relationship of UWS2, West-to-East pushover. 74

4.13 Force-displacement relationship of UWS2, East-to-West pushover. 74
4.14 Force-displacement relationship of UWS2, South-North pushover. 75
4.15 Rotation-torque relationship of UWS1, torsional loading. 76
4.16 Rotation-torque relationship of UWS2, torsional loading. 77
4.17 Force-displacement relationship of UWS1 and UWS2, EW cyclic loading. . 78
4.18 Residual drift regarding in-plan drift at 4.29 [m]. 78
4.19 Force-displacement response of UWS1 and UWS2, NS cyclic loading. . . . 79
4.20 Residual drift regarding in-plan drift at 4.29 [m]. 79
4.21 Bilinear representation of a static pushover analysis. 81
4.22 Elastic spectra of HNN and design elastic spectra from Eurocode 8. 82
4.23 Performance Point Determination with the N2 Method. 83
4.24 Force-displacement relationship of UWS1, EW static pushover and dynamic response. 85
4.25 Force-displacement relationship of UWS1, NS static pushover and dynamic response. 86
4.26 Relative displacement-time relationship of UWS1, full dynamic response in EW direction. 87
4.27 Base shear-time relationship of UWS1, full dynamic response in EW direction. 87
4.28 Relative displacement-time relationship of UWS2, full dynamic response in EW direction. 88
4.29 Base shear-time relationship of UWS2, full dynamic response in EW direction. 88
4.30 Evolution of residual displacement in EW direction of UWS1 and UWS2. . 89
4.31 Evolution of (a) maximum displacement and (b) maximum base shear in EW direction of UWS1 and UWS2. 89
4.32 Evolution of residual displacement in NS direction of UWS1 and UWS2. . 90
4.33 Evolution of (a) maximum displacement and (b) maximum base shear in NS direction of UWS1 and UWS2 90
4.34 Time-rotation response at 4.29 $[m]$ response of UWS1. 91
4.35 Time-rotation response at 4.29 $[m]$ response of UWS2. 91
4.36 Force-displacement response of UWS1 with various positions of the top masses, West-to-East static pushover. 93
4.37 Evolution of residual displacement regarding the position of the axial load, dynamic analysis. 94
4.38 Evolution of (a) maximum displacement and (b) maximum base shear regarding the position of the axial load, dynamic analysis. 94

A.1 "Total force versus average drift, X (EW) direction test" from Ile and Reynouard (2005). 100
A.2 "Total force versus average drift, Y (NS) direction test" from Ile and Reynouard (2005). 101

A.3 "Total horizontal force versus drift - X (EW), XY direction test" from Ile and Reynouard (2005). 102
A.4 "Total horizontal force versus drift - Y (NS), XY direction test" from Ile and Reynouard (2005). 103
A.5 "X (EW) and Y (NS) loads, XY direction test" from Ile and Reynouard (2005). 104
A.6 "Measure : shear force-top horiz displ, wall 1 test 1" from Combescure et al. (1999). 105
A.7 "Measure : shear force-top horiz displ, wall 1 test 3" from Combescure et al. (1999). 106
A.8 "Measure : shear force-top horiz displ, wall 1 test 4" from Combescure et al. (1999). 107
A.9 "Measure : shear force-top horiz displ, wall 3 test 3" from Combescure et al. (1999). 108

B.1 Beam-truss model of UW1, Seismostruct 3D view. 109
B.2 Beam-truss model of UW2, Seismostruct 3D view. 110
B.3 Beam-truss model of IR, Seismostruct 3D view. 111
B.4 Beam-truss model of RC+SMA, Seismostruct 3D view. 112
B.5 Beam-truss model of CEA, Seismostruct 3D view. 113
B.6 Beam-truss model of UWS1/UWS2, Seismostruct 3D view. 114

List of Tables

2.1 UW1 concrete mechanical properties 24
2.2 UW1 steel mechanical properties 26
2.3 RC+SMA shape memory alloy mechanical properties 28

3.1 UW1 and UW2 concrete mechanical properties. 35
3.2 UW1 and UW2 steel mechanical properties. 35
3.3 IR concrete mechanical properties. 42
3.4 IR steel mechanical properties. 42
3.5 RC+SMA concrete mechanical properties. 49
3.6 RC+SMA steel mechanical properties. 49
3.7 RC+SMA shape memory alloy mechanical properties. 49
3.8 Spacing of the hoops for each CEA unit. 52
3.9 CEA1 concrete mechanical properties. 54
3.10 CEA1 steel mechanical properties. 54

4.1 UWS1 and UWS2 concrete mechanical properties. 64
4.2 UWS1 and UWS2 steel mechanical properties. 64
4.3 UWS2 shape memory alloy mechanical properties. 65
4.4 Ground motion scaling factor from blind prediction. 70

Chapter 1

Motivation, Objectives and Organization

1.1 Motivation

Reinforced concrete cores, particularly in the widely used U-shaped form, serve for withstanding horizontal seismic loads, catering to both low and high-intensity regions. The increasing global construction demand, projected to double by 2060 [1], underscores the vital role of core walls in enhancing built environment resilience.

While concrete stands as an efficient and cost-effective construction material, the carbon dioxide emissions associated with its cement production are substantial. The persistent challenge of recycling concrete underscores the imperative to extend the longevity of buildings. Nevertheless, elongating a building's lifespan, such as from 50 to 100 years, subjects it to a wider array of unpredictable events, with earthquakes being a key concern.

To increase the lifespan of buildings and reduce the failure risk, an augmented level of confidence in the comprehension and simulation of reinforced concrete (RC) structures is indispensable. The ALL4wALL project, funded by the European Commission and initiated under the leadership of Prof. Almeida and a worldwide academic team, seeks to enhance the seismic resilience of core walls. The experimental campaign involves subjecting two half-scale RC U-shaped walls, denoted as UWS1 and UWS2, to testing on the shake table of LNEC, Lisbonne. This thesis, under the guidance of J.P. Almeida, R. Hoult, and A.A. Correia, all members of ALL4wALL, contributes to numerically model and analyse the behavior of the two units using beam-truss modelling (BTM) on the commercial software Seismostruct [2].

Both U-shaped walls, of more than 6 $[m]$ high and 40 $[ton]$, have the same geometry. UWS1 will exemplify the traditional RC composition designed according to Eurocode 8 [3], while UWS2 will incorporate strategically placed shape memory alloys (SMA) to minimize residual displacements. The aftermath of earthquakes often translates into huge financial losses attributed to residual displacements, leading to buildings and bridges tilting. Even if structures were well-designed and managed to withstand a seismic event, a slight residual inclination can result in discomfort, necessitating the demolition of the building.

An essential element of the ALL4wALL initiative is the prior modelling of U-shaped walls, to predict the future tests. Along this master thesis, other searchers will try to model UWS1 and UWS2 unit with various modelling techniques before the forthcoming experimental campaign.

1.2 Objectives and research novelties

The primary aim is to accurately predict and analyze the behavior of the future experimental tested walls, UWS1 and UWS2, within the framework of the ALL4wALL project.

The first specific objective is to understand beam-truss modelling (BTM) using previous experimental testing of various walls under quasi-static or dynamic loading. These tests will be used to **validate the model**, understand the software Seismostruct and set all the parameters for an accurate prediction of UWS1 and UWS2. The results will help enhance the predictive capabilities of the beam-truss model.

Thereafter, the second specific objective is to **model UWS1 and UWS2** to predict their behavior, analyse the influence of shape memory alloys (SMAs) and examine the impact of the application of the axial loads.

By addressing these objectives, this thesis will contribute to the ALL4wALL project with wider purposes, such as contributing to the advancement of understanding and modelling of U-shaped core walls under seismic loading conditions; providing insights into the behavior of structures with shape memory alloys, laying the groundwork for more resilient and sustainable structural design practices.

The research novelties of this master thesis lie in a comprehensive model validation encompassing both static and dynamic loading, as well as the incorporation of shape memory alloy within BTMs. Additionally, it constitutes a comprehensive prediction of the forthcoming ALL4wALL experimental campaign and marks the inaugural numerical analysis of the first dynamic test involving U-shaped walls with SMA.

1.3 Organization

Following this introduction chapter, the Chapter 2 delves into the current state of the art of previous experimental tests. This chapter also covers existing numerical models to represent nonlinearity and beam-truss model in more detail. Subsequently, the Seismostruct software and its material models will be discussed.

To ensure precise predictions of UWS1 and UWS2, the validation, calibration, and analysis of beam-truss modelling are essential. In Chapter 3, the experimental testing previously presented will be simulated using BTM approach and compared with their respective experimental results. This analyse will illuminate both the strengths and limitations of the model, setting the stage for the subsequent chapter.

Chapter 4 serves as the main chapter of this thesis, encompassing a comprehensive description of the two units as the testing setup and the loading protocol of the forthcoming experimental campaign. Afterwards, various static and dynamic analyses of UWS1 and UWS2 units will be conducted, spotlighting the influence of SMA and the impact of the position of the axial load. The chapter will conclude with the simulation of requisite data for the blind prediction competition, i.e., an open challenge to predict the response of the experimental testing.

The final chapter, Chapter 5, will conclude the thesis by summarizing the attained results and providing suggestions for the continuation of this research.

Chapter 2

State of the Art and Project All4wAll

2.1 Project description

Before getting to the heart of the matter of numerical modelling, an explanation of the European project is necessary to put the rest of the work into context. The project ERIES, from the European Commission, provides funding for the ALL4wALL project for the obtaining of a Transnational Access (TA) to run a dynamic test campaign on U-shaped walls. This thesis is strictly related to the project ALL4wALL whose reinforced concrete (RC) walls will be modelled and for which numerical results of the further tests will be presented using beam-truss model.

2.1.1 Eries

ERIES, or Engineering Research Infrastructures for European Synergies [4], is a project funded by the European Commission. Its primary objective is to provide TA to advanced research infrastructures in structural, seismic, wind, and geotechnical engineering. By granting access to experimental facilities, ERIES enables researchers to conduct studies and tests aimed at reducing damages and losses caused by natural hazards. The objective is to effectively manage risks and develop innovative solutions that contribute to a more sustainable society. The project also aims to assist in the adaptation of the European Seismic building code, Eurocode 8 [3].



Figure 2.1: ERIES logo.

ERIES encompasses three main research goals and four research areas. The first goal focuses on addressing the limitations of current seismic design and retrofit approaches for post-World War II existing structures against natural hazards.

The second goal centers around risk quantification to enhance societal resilience against natural hazards. By conducting additional experimental tests and collecting more data, researchers can calibrate existing mathematical models, providing the necessary tools to support the implementation of a next-generation seismic risk mitigation approach.

The final goal of ERIES is to contribute to climate change mitigation and promote green and sustainable development. This entails testing innovative materials that improve the lifespan of structures.

To achieve these goals, four research areas are described :

- **RA1: Built Environment**: This area examines the structures shape our everyday living and usage.
- **RA2: Critical Infrastructures**: This research area focuses on structures that have importance and impact life on a regional part.
- **RA3: Industrial Facilities**: This research area concentrates on structures that support industrial activities and have distinct characteristics not covered in RA1.
- **RA4: Advanced Technologies**: Different from the previous three research areas, RA4 focuses on advancing technologies. It explores the development and implementation of mitigation devices such as base isolation, viscous dampers, and innovative green and sustainable materials.

2.1.2 ALL4wALL

The project ALL4wALL, or by its full name, "Smart ALLoys for WALLS: towards durable structures with long service lives and minimal seismic residual displacements", is a high-level international collaborative research using TA facilities from ERIES. This project seeks to deepen the knowledge about the seismic behavior of RC U-shaped core walls by examining two factors that frequently contribute to poor structural response and hinder post-earthquake serviceability: torsional effects and excessive residual displacements.

To address the latter issue, an innovative approach has been devised, which involves partially substituting the base's longitudinal steel reinforcement with superelastic rebars made of shape memory alloys (SMA). The ALL4wALL project serves as a practical demonstration of this technological breakthrough, striving to ensure desired performance levels for buildings with significantly prolonged service lifespans, which should be an aim for sustainable design and assessment.

This experimental campaign is a continuation of quasi-static tests on U-shaped wall overseen by Hoult et al. at the UCLouvain, Belgium [5]. The objective was to investigate the in-plane and torsional seismic performance of two half-scale RC U-shaped walls, denoted UW1 and UW2, respectively. Further details about these test units can be found in Section 2.2.1.1.
Unfortunately, relying solely on quasi-static tests is inadequate. According to Park's study in 1989 [6], this approach fails to replicate the exact strain rate or displacement history of specific earthquakes. This tends to provide conservative estimations of a structure's actual strength. Dynamic tests become essential because genuine earthquake loads are inherently dynamic, and the materials' strength responds to elevated strain rates.

The objective of ALL4wALL project is to test on a shake table two slender U-shaped walls subjected to some ground motions designed to induce unidirectional flexure and torsion. The first unit, denoted as UWS1, will be made of traditional RC according to Eurocode 8. The second wall, UWS2, will be similar to UWS1 but specific rebars will be replaced locally by SMA rods. The test performed on UWS2 is expected to exhibit reduced residual displacements in comparison to UWS1. The illustrative influence of SMAs is depicted in Figure 2.2, from the project submission document [7].

These tests will represent the initial exploration in torsional nonlinear response of U-shaped wall. Additionally, they serve as the first experimental assessment of a wall tested experimentally, under realistic conditions of dynamic excitation, to verify the emulation of a superelastic plastic-hinge region. Given the scarcity of large-scale tests, this initiative contributes to the accumulation of additional data concerning the dynamic behavior of RC walls.

From an experimental perspective, an innovative and precise measurement approach will be employed. Distributed Fiber Optic Sensing (DFOS) will be utilized to accurately measure the strain in the steel rebars. Digital Image Correlation (DIC) based on tracking the motion of circular targets glued to the outer surface. This aims to capture both localized behavior using DFOS and the global response through DIC, providing a comprehensive evaluation of the U-shaped wall's performance, in addition to other usual measurement sensors.

To complete the description, a good numerical simulation will be needed to estimate the response of the units and furthermore for calibration after the tests. This is a main part of the project using plenty of different modelling approaches such as nonlinear beam-truss models, i.e. the subject of this master thesis.

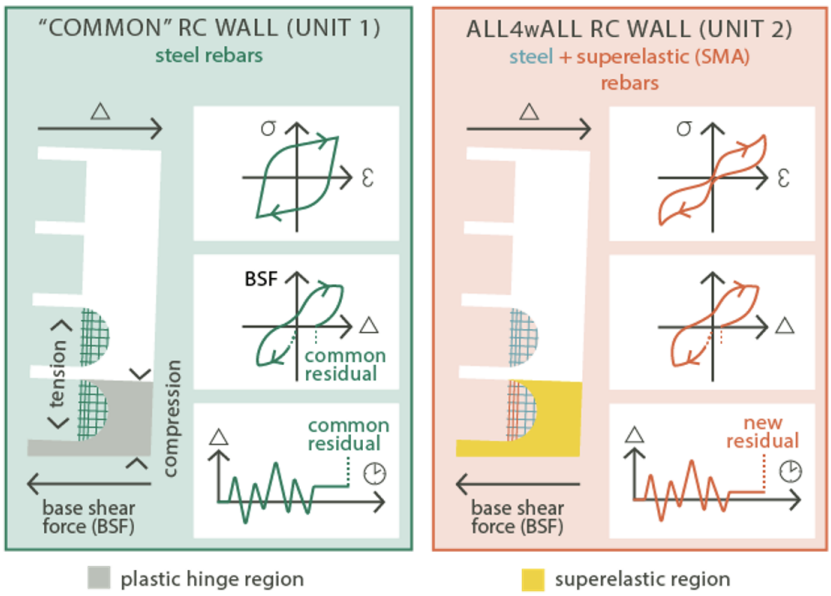


Figure 2.2: Expected difference for RC and SMA wall from project submission by Almeida et al..

This project is a collaborative effort involving over 14 individuals, including professors, postdocs, and PhD students spread across seven universities: Université catholique de Louvain, ENPC ParisTech, ISAE-Supméca Institut supérieur de mécanique de Paris, University of Liège, University of Ljubljana, University of Pavia, and York University. Additionally, the project benefits from the expertise of the LNEC (Laboratório Nacional de Engenharia Civil) and the LEMSC (Laboratoire essais mécaniques, structures et Génie civil) from Louvain-la-Neuve.

ALL4wALL is relevant in two research areas and two research goals addressed by ERIES. RA1 "Built Environment", more and more people live in RC buildings with core walls at the periphery of the building. Understand the implication of torsional core wall response on the structural part is required to improve Eurocode-compliance. RA4 "Advanced Technologies" is reached on different points: a novel seismic mitigation approach with SMA will advance its technology readiness level (TRL) and will be tested for the first time on RC walls under dynamic response; a recent fiction-weld will also advance its TRL; the instrumentation of measure in LNEC3D will also be completed by DFOS and cameras for dynamic application. It encompasses the Research Goal 1 about "Loss-driven design and mitigation approaches" and Research Goal 3, "perspective of sustainable development" is the general motivation which is to improve the lifespan of structures.

2.1.3 Description of the transnational access facility

The TA facility used for the tests will be the three-dimension shake table (ST3D) [8], a shake table allowed to vibrate in three transversal directions in LNEC, Lisbon, Portugal. A snapshot of the site during a final year trip for civil engineering students at UCLouvain is illustrated in Figure 2.3.

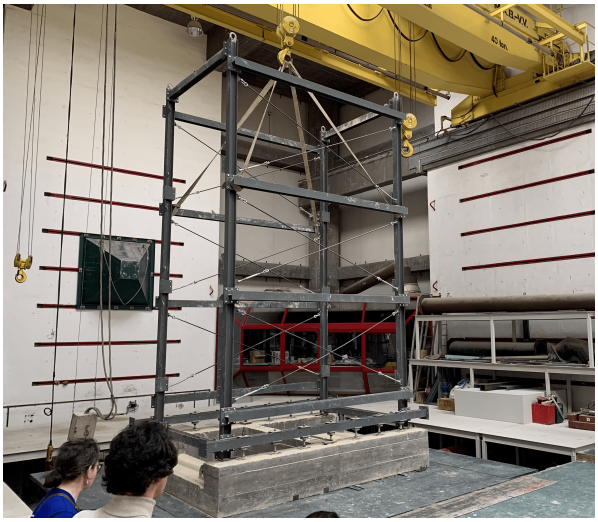


Figure 2.3: Picture of the LNEC 3D shake table from the author (29-03-2023).

This facility will permit to work with two dynamic directions on a large scaled model with important loading. Further details are provided about the limitation of the table in Section 4.1.2.

2.2 Previous experimental tests

The upcoming tests involving a U-shaped wall with shape memory alloy on a shake table constitute a novel experimental campaign that has not been conducted previously. To ensure the execution of dependable tests yielding pertinent data, it becomes imperative to draw upon prior experimental campaigns. A concise overview of these campaigns and their conclusions will be provided. Model validation of these experiments will be undertaken in Chapter 3, as well as more complete information about materials and geometry of the structures.

2.2.1 Quasi-static tests on U-shaped wall

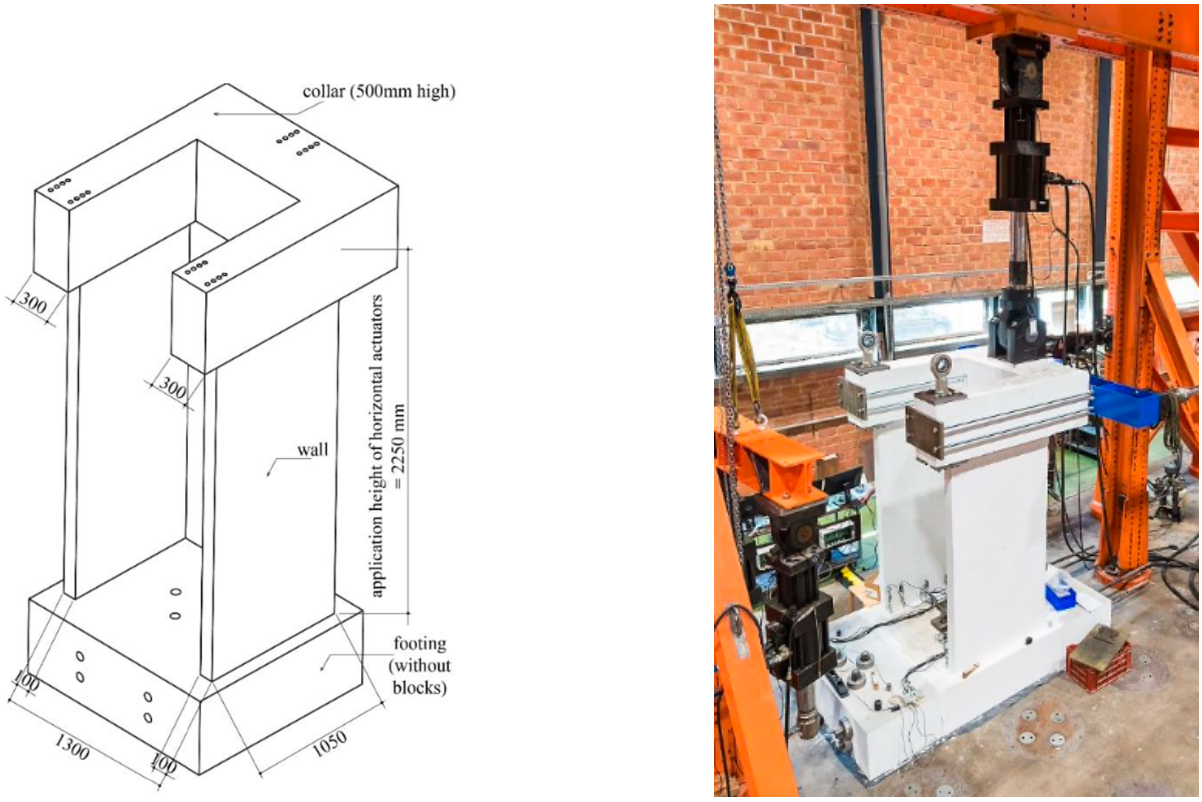
2.2.1.1 Units UW1 and UW2 from Hoult et al. (2022)

Hoult et al. conducted an experimental campaign [5] at the Institute of Mechanics, Materials and Civil Engineering (IMMC) to investigate the in-plane and torsional behavior of two half-scale U-shaped walls in reinforced concrete, denoted UW1 and UW2 respectively. Both units have the same dimensions but will be tested under distinct loading conditions.

The first test unit, UW1, was subjected to quasi-static reverse-cycling loading with bending about its minor axis. An overturning moment was applied to UW1 to increase the shear span, i.e., the effective height of application of the horizontal loading, to approximately 6.32 $[m]$. The axial load being not exactly at the center of gravity, it has an influence on the shear span. At the peak of the horizontal loading, the shear span was founded to be 5.7 $[m]$ and 7.9 $[m]$ pushing from North-to-South and South-to-North respectively.

The second unit, UW2, was subjected to quasi-static reverse-cyclic rotation, i.e., torsional twist. No additional overturning moment was applied to modify the shear span. The height from the foundation to the center of the collar (head) of UW1 and UW2 was 2.25 $[m]$. The wall is depicted in Figure 2.4, more information, such as material properties will be presented in Chapter 3 during the model validation.

An axial load ratio (ALR) of 5% was applied to both UW1 and UW2. The ALR can be defined as the ratio between the applied normal force and the resisting concrete force : $\frac{N}{f_c A_g}$, with N as the axial load in kN, f_c as the concrete compressive strength in kPa and A_g as the gross area in m^2.



(a) (b)

Figure 2.4: UW1 unit (a) 3D view [Unit: mm] and (b) picture of the testing campaign, both from Hoult et al. (2023).

The experimental response of these two walls was the object of an international blind prediction competition. As it will be the case for the walls of the All4wAll project, UWS1 and UWS2. These walls will have the exact same geometry and longitudinal reinforcement as the UW1 and UW2 wall, the spacing between the stirrups and the transversal reinforcement are slightly different.

The wall units were extensively instrumented including digital image correlation (DIC), distributed fiber optic sensors (DFOS). These precise data were readily available and can be downloaded from the publicly accessible platform Dataverse [5].

2.2.1.2 Units IR from Ile and Reynouard (2005)

An experimental and numerical campaign to investigate the behavior of U-shaped walls subjected to lateral uniaxial and biaxial cyclic loading was conducted by Ile and Reynouard in 2005 [9]. A total of three full-scale walls were fabricated according to Eurocode 8 [3] tested at the ELSA laboratory. They all have the same dimensions and reinforcement, despite some small changes in concrete strength, but the direction of loading is different at each test. A total vertical force of 2 $[MN]$ is applied at the gravity center to avoid spurious bending of the structure. A clear representation of the wall and directions is depicted in Figure 2.5 from Ile and Reynouard (2005) [9].

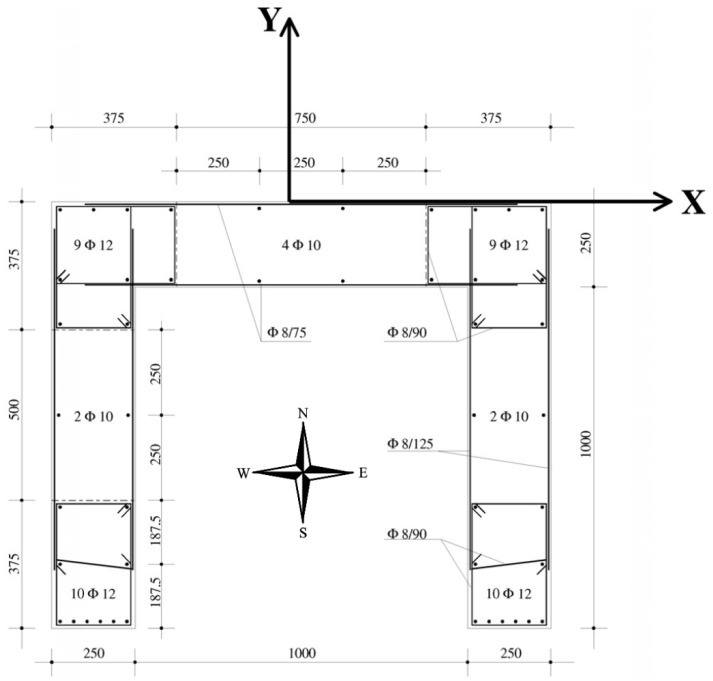


Figure 2.5: Section of the test specimen IR [Unit: mm] from Ile and Reynouard (2005).

In this thesis the walls will be denoted as:

- **IR1**: for the wall tested in the North-South (NS) direction along the minor (weak) axis. The sense of pushing is called minor because the strength of the unit is lower in this direction (NS) than the other (EW). This can be observed in the experimental and numerical results at Section 3.2.
- **IR2**: for the wall tested in the East-West (EW) direction along the major (strong) axis.
- **IR3**: for the wall tested in both directions, going from its initial position, to the North, then, to Northeast, to East, to center and repeating this with each direction like represented in Figure 2.6 from Ile and Reynouard (2005) [9]. This loading protocol is referred as "butterfly path" in the paper.

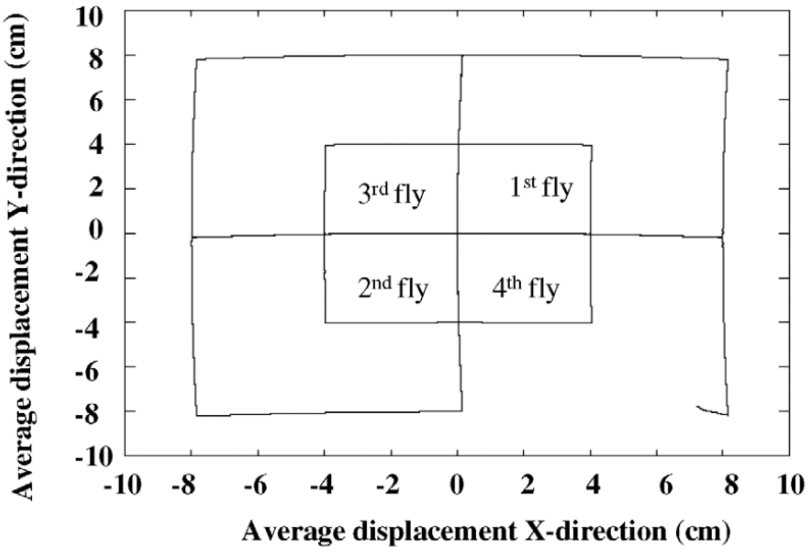


Figure 2.6: Loading protocol of IR3 from Ile and Reynouard (2005).

These tests concluded that the use of boundary confinement let obtain a more ductile deformation. They are also verifying their tests with a shell element on finite elements. A model validation will be performed in Section 3.1 to validate the beam-truss model with another U-shaped wall under quasi static-loading then UW1.

2.2.2 Dynamic tests on U-shaped wall

Dynamic testing holds significant importance in comprehending and validating the beam-truss model. Regrettably, such tests are scarce, with only one identified in the available literature.

2.2.2.1 Units CEA from Combescure et al. (1999)

Between 1996 and 1999, an experimental campaign to investigate the influence of boundary confinement of a U-shaped wall under dynamic loading was conducted by Combescure et al. [10]. A total of four U-shaped walls were tested on the AZALEE shake table at the Seismic Mechanic Study Laboratory of CEA, at Saclay in France. The four walls, denoted in this study as CEA0, CEA1, CEA2 and CEA3, have the same geometry but a different spacing of the stirrups in the boundary regions. They have 3 masses of 6.45 tons on their top as shown in Figure 2.7. For each wall, a series of increasing level seismic tests between 0.10 $[g]$ and 1 $[g]$ has been realised.

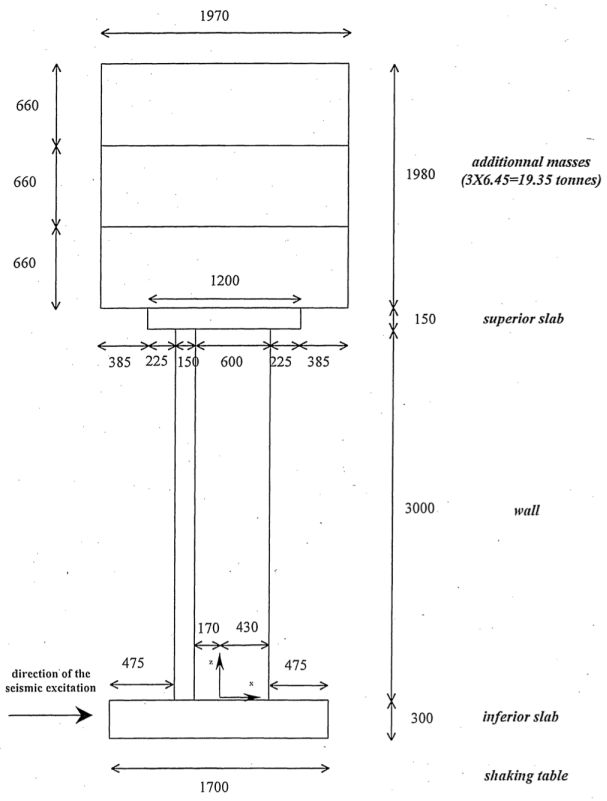


Figure 2.7: Elevation plan of CEA walls from Combescure et al. (1999) [Unit: mm].

The ultimate strain of the steel was notably lower than the recommendation compared to the recommendation of Eurocode 8 [3], this resulted in poor ductility. In spite of limited data availability and challenges posed by the quality of the paper figures, a model validation has been performed in Section 3.4, which includes additional details about the material properties.

2.2.3 Tests on walls with shape memory alloys

Numerous recent tests have aimed to improve the performance of RC elements by incorporating SMA rebars. However, for the sake of conciseness of this thesis, the author will focus on salient experimental tests, which will serve for validating numerical models in Section 3.3.

2.2.3.1 Unit "RC+SMA" from Almeida et al. (2020)

An experimental campaign was conducted by Almeida et al. [11] in the iMMC, Louvain-la-Neuve, Belgium to investigate the influence of shape memory alloy on RC walls. Two planar shear walls were tested with quasi-static reverse-cyclic loading in the in-plane direction.

The walls at scale 2:3 share the same geometry and reinforcement except that the first unit, denoted RC, has its reinforcement only made of steel reinforcing bars (rebars) and is designed in accordance to Eurocode 8 [3]. The second unit, denoted "RC+SMA", has 4 shape memory alloys rebars at the base of each boundary element. Both wall geometries are depicted in Figure 2.8 such as the coupler and the instrumentation. Due to laboratory constraints, the construction of taller and more expensive units is not always possible. The test is using an additional overturning moment to have a shear span ratio, i.e., the ratio between the height and the length of the wall, equal to 3.6 despite the dimensions of the wall of 1.2 $[m]$ long and 2.2 $[m]$ height (distance between the top of the foundation and the middle of the collar).

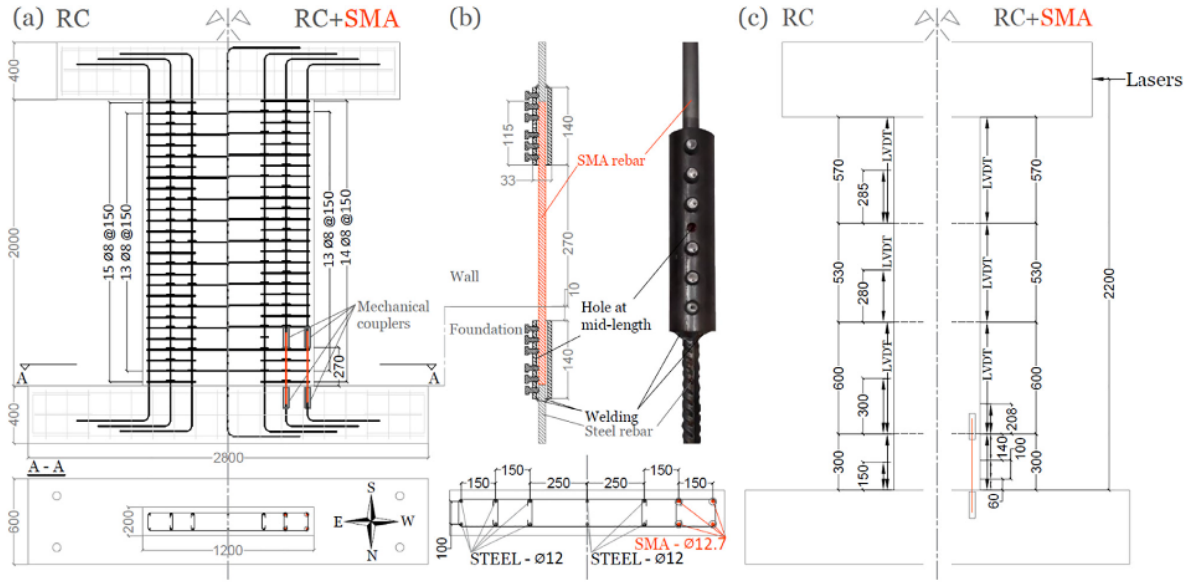


Figure 2.8: (a) Geometry and reinforcement layout of the two test units, including cross-section close-up. (b) SMA-steel rebar assembly and mechanical coupler photo. (c) Instrumentation with the laser measurement position from Almeida et al. (2020). [Units in mm.]

The RC wall, the first unit, experienced a foundation failure, rendering it unsuitable for model validation. This problem did not occur to the second unit which is interesting for model validation and is denoted "RC+SMA" in the paper.

The tests conclude to a large reduction of residual displacements, a reduction of around 67% and an increase of energy dissipation by using SMA. For small displacement demands below the yield displacement the presence of SMA alloy rebars logically does not contribute to minimise the residual displacements. This experimental testing will be utilized to validate the material model of the SMA implemented on Seismostruct in Section 2.4.1 and to validate the beam-truss model in Section 3.3.

All the dataset was readily available and can be downloaded from the publicly accessible platform Dataverse [11].

2.2.3.2 Bridge bent from Noguez and Saiidi (2012)

In 2012, Noguez and Saiidi proceeded to an experimental dynamic test [12] on a four-span bridge incorporating several innovative plastic hinges on a shake table at the University of Nevada, Reno. The bridge, at quarter-scale, is made of three pairs of two columns, each pair, denoted as bent in the paper, of which utilized a different unconventional detail at the bottom plastic hinges: the first bent, with SMAs and engineered cementitious composites (ECCs), i.e., concrete with fibers that can accept tensile strength, the second with elastomeric pads embedded into column and the third with posttensioning tendons. The bridge was subjected to horizontal simulated earthquake records applied by three shake tables at the base of each bent. A general view of the specimen is represented in Figure 2.9 from Noguez and Saiidi (2012) [12].

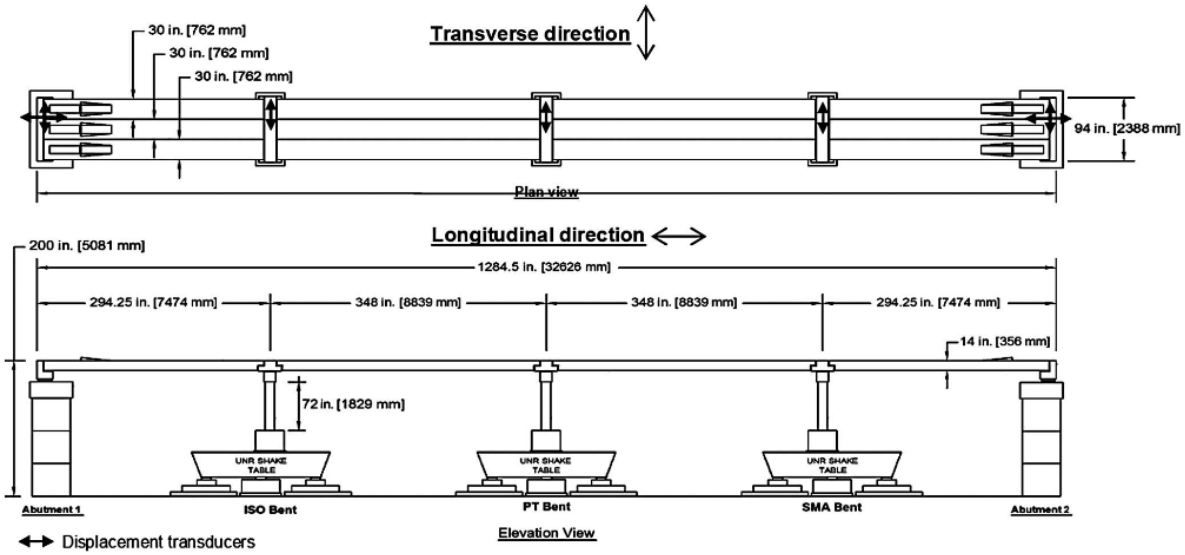


Figure 2.9: Bridge geometric details from Noguez and Saiidi (2012).

The particularly noteworthy column pair of column for this thesis is the one with SMAs, depicted in Figure 2.10. However, columns cannot be simulated using beam-truss modelling, which is for walls. The primary objective of modelling these column would be to examine SMA under dynamic loading. Unfortunately, due to the lack of data concerning the employed materials, the axial loading and the dynamic input of the shake tables, modelling was not possible.

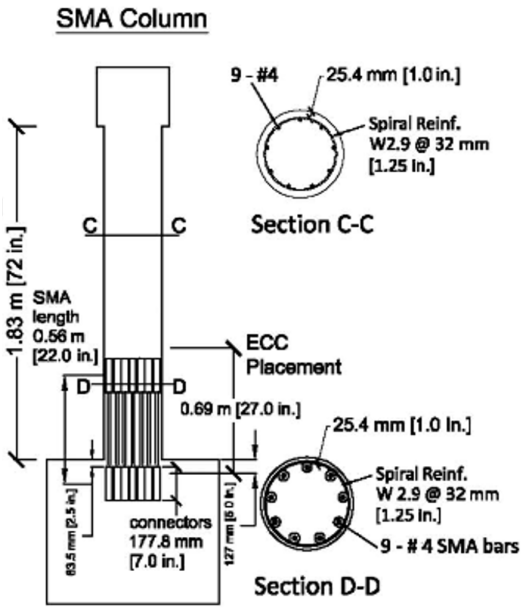


Figure 2.10: Side view of the SMA column from Noguez and Saiidi (2012).

Nevertheless, the findings presented in the paper are interesting and align with the previous test with SMA from Almeida et al. (2020). The results regarding SMAs demonstrate their capacity to minimize residual displacements under lateral loading conditions. The combination ECC and SMA was reducing earthquake damages. The use of advanced materials could keep the bridge in service after a maximum design earthquake, saving the cost of repair and replacement that would incur in a conventional RC bridge. This underscores the significance of investigating the influence of SMAs on UWS2 under dynamic scenarios.

2.3 Numerical modelling

When performing numerical analyses, accounting for nonlinearity becomes imperative to achieve computational results that closely mirror the actual structural behavior, particularly when dealing with extreme loads, deformations, or rotations. There exist two types of nonlinearities: geometric and material. Geometric nonlinearities are due to significant deformations, causing effects like buckling or P-delta effect. Material nonlinearities, occur at the section level regarding material model. This section will introduce various methods for modelling nonlinearity, including beam-truss modelling (BTM), employed for Chapter 3 and Chapter 4.

2.3.1 General overview of nonlinear models

This section draws on Mathis Keirle's thesis [13], who has realized an analysis of effective stiffness of I, T and U-shaped walls using stick modelling, wide-column modelling (WCM) and BTM. Further comparison between these models can be found in Mathis Keirle's thesis. Only beam-truss modelling will be employed in the further analysis, however stick model and wide-column model will be briefly presented. While other modelling approach to simulate the behavior of RC exists, such as the Multiple-Vertical-Line-Element-Model (MVLEM) discussed in Isakovic et al. (2019) [14], nonlinear finite element analysis like VecTor3 [15] and others, are outside of the scope of this research.

2.3.1.1 Stick Models

Stick models are a convenient and time-efficient method for numerical modelling of walls. The stick model approach involves the representation of a wall using a single vertical beam finite element positioned at the center of its cross-section. As a result, a one-dimensional model is obtained. An illustration of a stick model for a wall with a rectangular cross-section is presented in Figure 2.11 from M. Keirle's thesis (2022)[13].

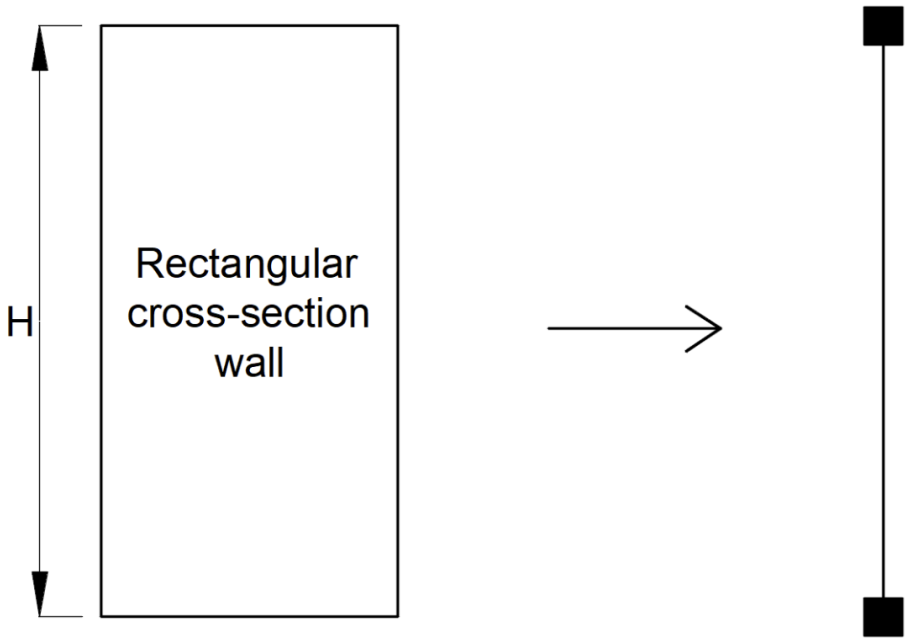


Figure 2.11: Elevation view of stick model for a rectangular cross-section wall from M. Keirle thesis (2022).

An inherent limitation of the stick model arises when attempting to simulate the behavior of a non-planar wall, such as a U-shaped wall. Simulating the distribution of shear forces becomes challenging, and there is no provision for warping, as indicated by Pelletier and Léger (2017) [16]. Another limitation resides in the application of the axial load which can only be applied at the geometric center of mass of the wall, e.g., UW1 cannot be modelled using stick model due to the load offset.

To overcome the drawbacks of stick models, other approaches are commonly used: wide-columns models (WCMs), beam-truss models (BTMs), multiple-vertical-line element model (MVLEM) or refined finite elements.

2.3.1.2 Wide-Column Models (WCMs)

According to Beyer et al. (2008) [17], the WCM , also known as wide-column analogy or equivalent frame method was originally developed for planar wall structures [e.g., Clough et al., (1964); MacLeod, (1973)] and was later extended to non-planar structures [e.g., MacLeod and Hosny, 1977; Stafford Smith and Abate, 1981].

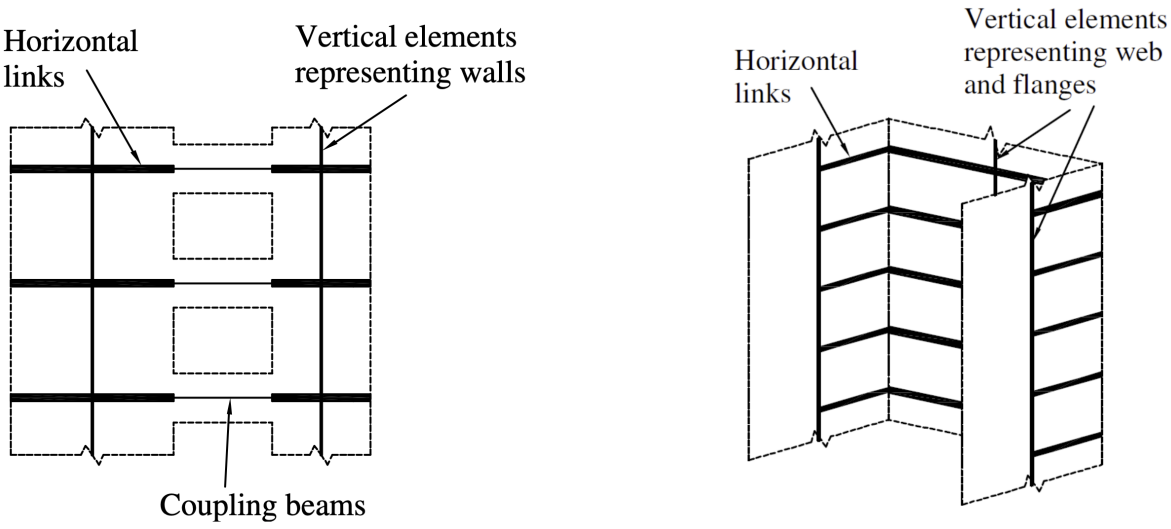


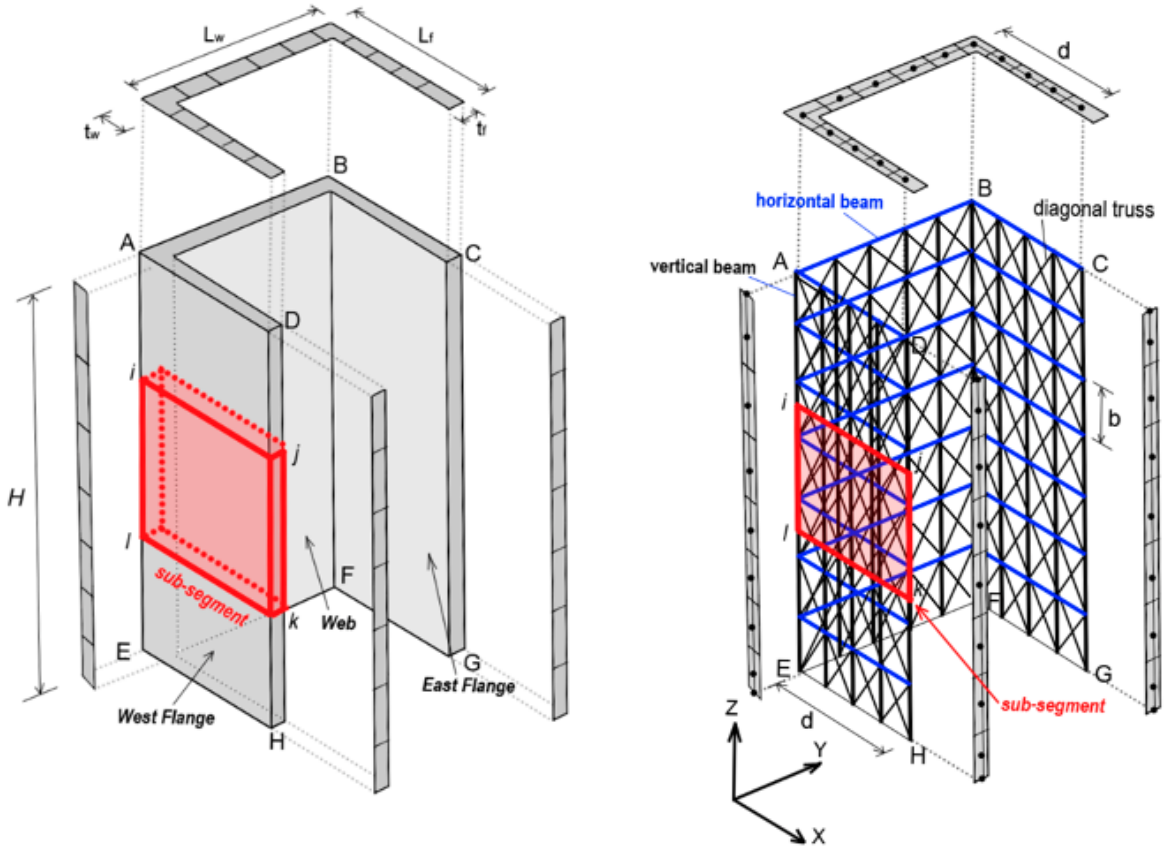
Figure 2.12: Wide column model of (a) coupled walls and of (b) a U-shaped wall from Beyer et al. (2008).

Examples of WCMs for structural walls coupled by deep beams and for U-shaped walls are respectively depicted in Figures 2.12a and 2.12b. When modelling non-planar walls, the web and flange sections are represented by vertical elements located at the centroid of the web and flange sections. These vertical elements are then connected by horizontal links running along the weak axis of the sections having common nodes at the corners. Except for a torsional flexibility, which they are typically assigned, these links are modelled as rigid.
As developed in Beyer et al. (2008) [17], WCMs have shown reasonable simulation accuracy for in-plane flexural behavior of U-shaped walls. However, assessing torsion precisely is challenging due to a lack of experimental data and complexities related to warping behavior. The truss action mechanism corresponding to shear forces poses another challenge for WCMs, as they use only one beam element per wall segment. Accurately modelling shear performance for non-planar walls is vital due to their increased shear deformation compared to planar walls. This underlines the significance of adopting beam-truss modelling techniques.

2.3.2 Beam-Truss Model (BTM)

The models presented previously are interesting and very useful in their domain, but, in order to be able to model non-planar walls, to consider torsion and warping, to compute it in a reasonable time and to maintain continuity with previous work of other students' thesis, beam-truss models are going to be used. For Further information, the ongoing thesis of Christophe Saegerman [18], is discussing more in detail BTM.

The beam-truss model was developed by Lu & al. (2014) [19] to simulate nonlinear flexure-shear interactions and seismic response of planar and non-planar RC walls. The BTM uses Euler-Bernoulli beam elements for the horizontal and vertical elements and nonlinear truss elements for the diagonal elements. Figure 2.13a from Hoult et al. (2023) [20] illustrates a U-shaped wall where the wall lengths in the x- and y-directions are L_f and L_w, respectively, corresponding to the wall segment definitions in Figure 2a (i.e., the flange and web lengths). The thicknesses of the planar wall segments parallel to the x- and y-directions correspond to t_w and t_f, respectively, whereas the height of the wall unit is H, not to be confused with point H, also in the same figure. The BTM of this wall is illustrated in Figure 2.13b from Hoult et al. (2023) [20], which consists of two types of elements: nonlinear fiber-section Euler–Bernoulli beam elements in the vertical and horizontal directions, and nonlinear truss elements in the diagonal directions.



(a) (b)

Figure 2.13: Schematic illustration of (a) a U-shaped wall and (b) its beam-truss model from Hoult et al. (2023).

The sub-segment "i-j-k-l", in red on Figure 2.13a and 2.13b, part of the web flange is extended in Figure 2.14c. Figure 2.14d and e illustrate the area of concrete and steel for the vertical and horizontal beam elements.

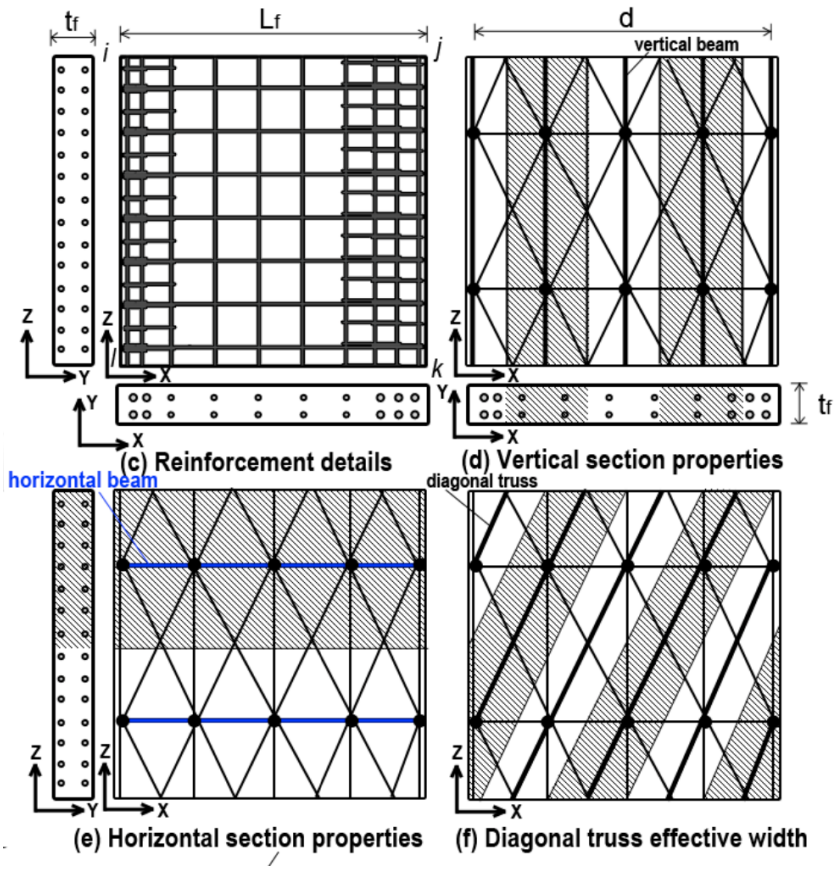


Figure 2.14: Representation of the beam-truss model from Hoult et al. (2023).

Diagonal elements, modelled by truss elements, are using a certain effective width of concrete which can be calculated as a function of the angle of the diagonal elements with the horizontal (θ_d) as represented in Figure 2.15: $b_{eff} = a \sin(\theta_d)$.

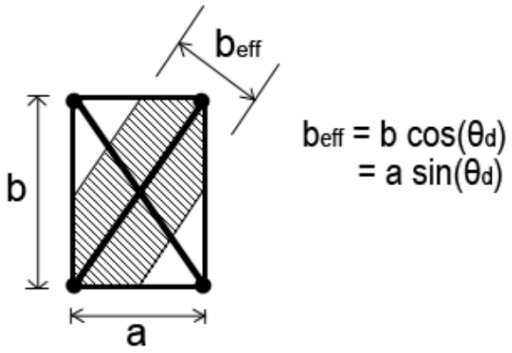


Figure 2.15: Representation of the diagonal element in BTM from Hoult et al. (2023).

This value of θ_d is developed by Lu et al. (2016) [21] and influences the mesh of the wall:

$$45^\circ \leq \theta_d = tan^{-1}(\frac{V_{max}}{f_{yt}\rho_t t_w d}) \leq 65^\circ \tag{2.1}$$

where f_{yt} is the yield strength of transversal reinforcement, ρ_t is the transverse reinforcement ratio, i.e., the ratio between the volume of horizontal steel rebars and the volume of concrete, t_w is the thickness of the wall, d is the distance between the outer vertical lines of the model in the direction of loading and V_{max} is the maximum shear force capacity. The shear capacity can be found in an experimental previous test if data are available and, in the absence of data, from moment-curvature analysis or by iteration, assuming a value of θ_d, model the wall and finding a value of V_{max} and iterate until convergence.

2.4 Seismostruct, material models and performance criteria

For all subsequent analyses, the beam-truss models were simulated using Seismostruct [2]. This commercial software is a 3D Finite Element package from Seismosoft capable of conducting static and dynamic analysis of framed structures. This program includes geometric nonlinearity and materials inelasticity through many elements type and material models. It is user-friendly, featuring a well-designed visual interface, and is comprehensively documented in the Seismostruct User Manual.

The inelastic frame displacement-based beam element with two nodes (infrmDB) was employed to model the vertical and horizontal beam elements. Inelastic truss elements were utilized for the diagonal components. It's worth noting that this approach diverges from the original method proposed by Lu et al. (2014) [19], where beam elements were used exclusively for vertical boundary regions such as corners and end flanges of U-shaped walls, while truss elements were employed for the rest of the vertical and horizontal elements, including diagonals. Although Seismostruct's limitations prevented an exact replication of this mesh configuration, the chosen approach—employing beam elements for all vertical and horizontal elements-yielded satisfactory results. Additionally, elastic elements (elfrm) were assigned with elevated rigidity values for rigid components like the top slab and collar, while mass elements were used to represent masses.

2.4.1 Material models

To ensure the highest quality results, the first critical aspect involves the material models. These models are already incorporated within Seismostruct and will undergo validation through actual experimental tests conducted on the UW1 wall concrete and steel rebars, as the SMA model will used the properties from the "SMA+RC" wall.

2.4.1.1 Concrete

The constitutive model adopted for the concrete comes from Mander et al. [22] and is denoted as "con_ma" in Seismostruct. The concrete confinement effects provided by the lateral transverse reinforcement are incorporated through the rules proposed by this model. The parameters applied for a complete model and the corresponding values for the UW1 wall can be found in Table 2.1

Table 2.1: UW1 concrete mechanical properties

Properties	f_c	f_t	E_c	ϵ_c	γ
Unit	MPa	MPa	GPa	%	kN/m^3
Value	38.2	3.07	29	0.2	21.7

With f_c as the concrete compressive cylinder strength at the day of testing, f_t as the tensile concrete strength, E_c as the concrete elastic modulus, ϵ_c as the strain at peak stress and γ as the specific weight.

The result of the tests and the numerical model of Mander et al. corresponding representation are depicted in Figure 2.16.

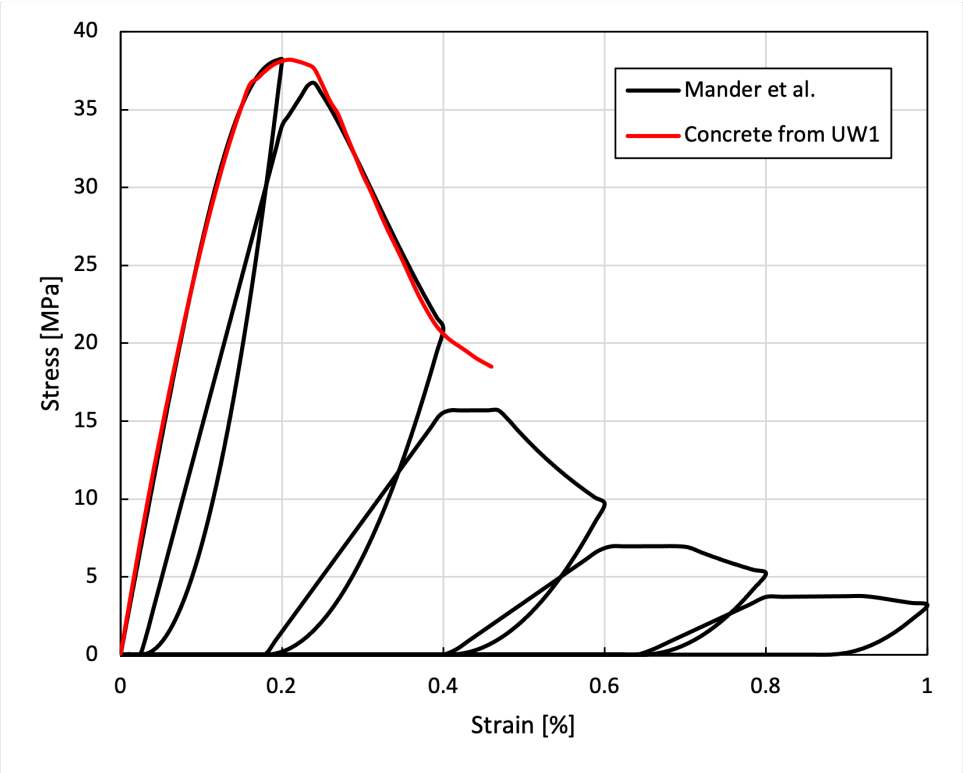


Figure 2.16: Strain-stress relationship of unconfined concrete, numerical model and experimental test.

Confined concrete, i.e., concrete restrained by hoops and stirrups in the boundary ends of walls, is much more ductile than unconfined concrete. This effect is represented in the model of Mander et al. with a confinement factor of 1.2 and can be observed in Figure 2.17. During all the analysis, the confinement factor will be automatically computed by Seismostruct regarding the geometry, the strength of the concrete and the reinforcement. Its value usually fluctuates between 1.0 and 2.0 for reinforced concrete members.

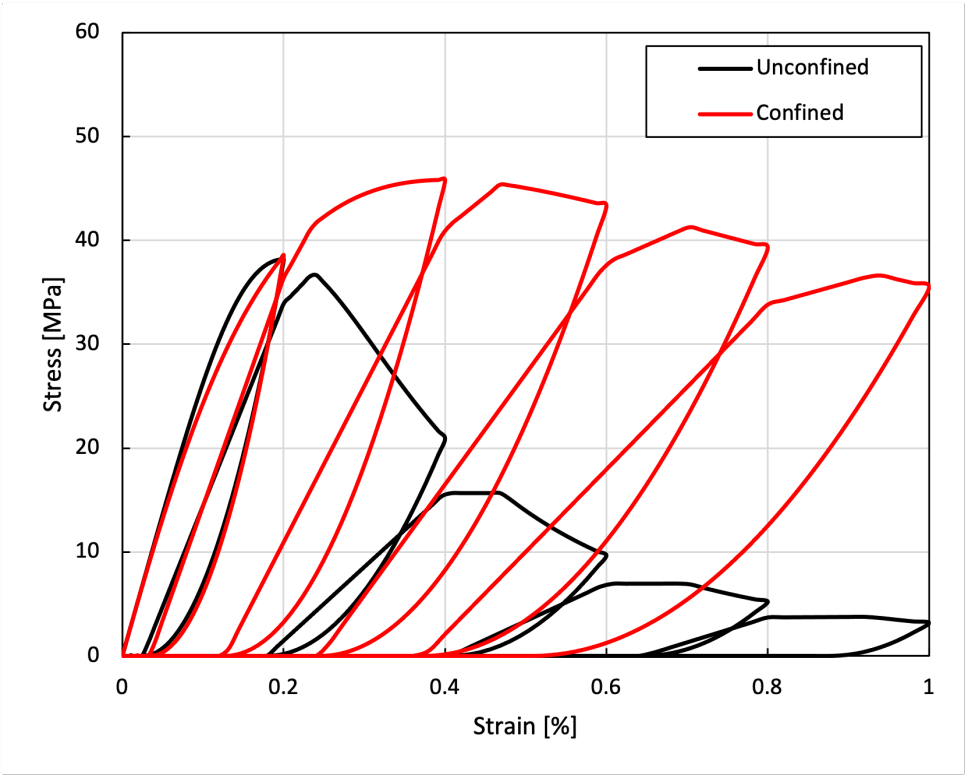


Figure 2.17: Strain-stress diagram of confined (1.2) and unconfined concrete model.

2.4.1.2 Steel model

The chosen constitutive model for the steel reinforcement bars (rebars) is the Menegotto-Pinto model [23], denoted as "stl_mp" in Seismostruct. The parameters employed for a comprehensive model, as well as the specific values corresponding to the 12 $[mm]$ rebars of the UW1 wall, are provided in Table 2.2. Default values are used for all other parameters.

Table 2.2: UW1 steel mechanical properties

Properties	d	f_y	f_u	E_s	ϵ_y	ϵ_u	α	γ
Unit	mm	MPa	MPa	GPa	%	%	%	kN/m^3
Value	12	580	690	199	0.29	10.1	0.56	78

With d as rebar diameter, f_y as the yield tensile strength, f_u as the ultimate strength, E_s as the Young's modulus, ϵ_y as the yield strain, ϵ_u as the ultimate strain, α as the strain hardening parameter and γ as the specific weight. The strain hardening ratio is a material

parameter representing the hardening of steel described in the formula 2.2.

$$\alpha = \frac{f_u - f_y}{(\epsilon_u - \epsilon_y) \cdot E_s} \tag{2.2}$$

The comparison of the result of the tensile test on 12 $[mm]$ rebars of UW1 and the Menegotto-Pinto model of Seismostruct is depicted on the Figure 2.18.

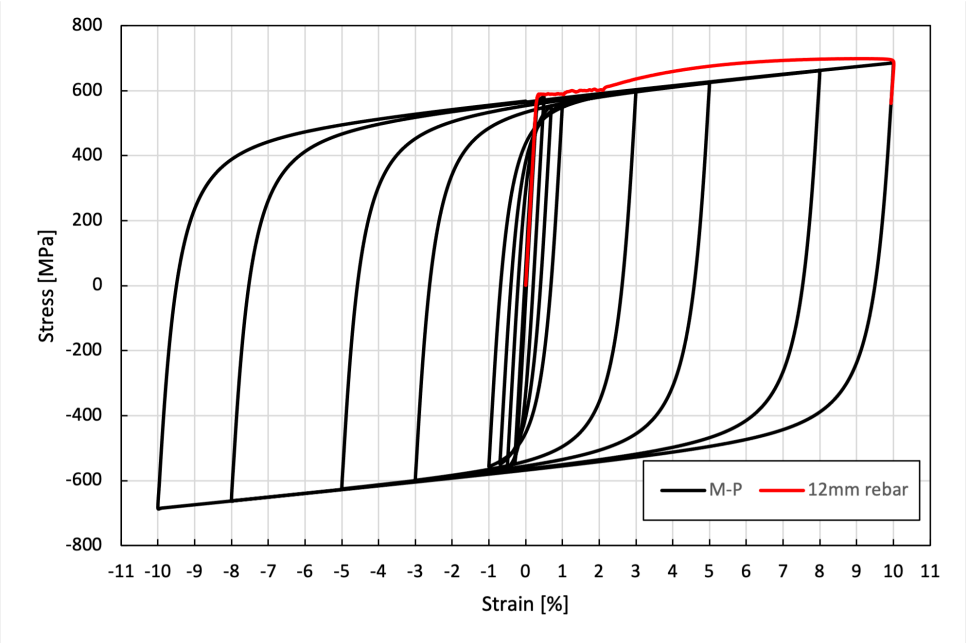


Figure 2.18: Strain-stress diagram of steel, numerical model and experimental test.

2.4.1.3 Shape Memory Alloy model

Shape memory alloys, specifically Nitinol (a Nickel titanium alloy), are known for their exceptional superelastic properties and their ability to exhibit reduced residual displacement after entering plasticity compared to steel rebars. In Seismostruct, a single model is available for shape memory alloys, known as the "se_sma" (for superelastic shape-memory alloys). This model assumes a constant stiffness for both fully austenitic and fully martensitic behaviors.

The experimental test conducted by Almeida et al. (2020) [11], as discussed in Section 3.3, employed shape memory alloy rebars with a diameter of 12.7 $[mm]$. The model parameters for this alloy can be found in Table 2.3. These rebars underwent a process of hot rolling

and subsequent heat treatment to attain the desired superelastic behavior suitable for regular ambient temperatures.

Table 2.3: RC+SMA shape memory alloy mechanical properties

Properties	d	E	σ_{AMs}	σ_{AMf}	σ_{MAs}	σ_{MAf}	γ
Unit	mm	GPa	MPa	MPa	MPa	MPa	kN/m^3
Value	12.7	31	319	349	73	32	65

Where d is rebar diameter, E is the modulus of elasticity, σ_{AMs} is the austenite to martensite start stress, σ_{AMf} is the austenite to martensite finish stress, σ_{MAs} is the martensite to austenite start stress, σ_{MAf} is the martensite to austenite finish stress, and γ is the specific weight.

Tensile cyclic loading tests were performed to demonstrate the superelastic hysteretic behavior of the SMA. The results of this test and the model is depicted in Figure 2.19.

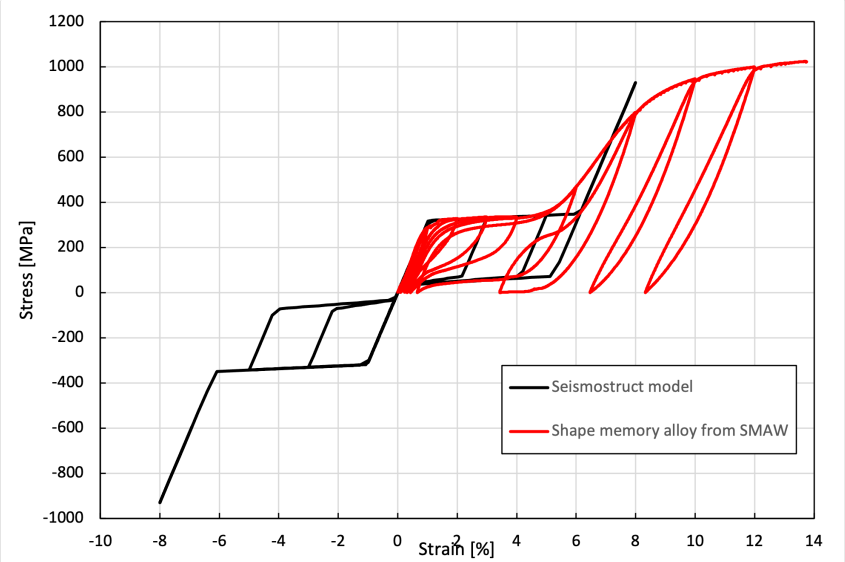


Figure 2.19: Strain-stress diagram of SMA, numerical model and experimental test.

The experimental superelasticity behavior is observed up to deformations of approximately 6%, resulting in a residual strain of around 0.75%. However, beyond this point, after the martensite phase, a significant reduction in the pseudo-elastic behavior of the SMA rebar is evident. For instance, unloading from an imposed deformation of approximately 8%

leads to a residual strain of around 3.6%. The difference with usual steel and its utility in future buildings is blatant.The cost of this material is still very expensive but with limited use, only at the bottom and in boundary regions for example, the cost of the SMA remains negligible regarding the overall construction cost.

Figure 2.19 highlights a notable limitation of the model: it predicts zero residual displacement, whereas the real material exhibits around 0.75%. This discrepancy can be attributed to the "flag shape" model used in Seismostruct. A comprehensive analysis of the structural behavior considering this limitation will be presented in Section 3.3. It's worth mentioning that a more realistic model will potentially be incorporated into Seismostruct in the future, although this is not currently the case.

2.4.2 Performance criteria and failure mode

The material models align closely with the actual values obtained from experimental tests. However, Seismostruct presents a limitation in effectively representing wall rupture through beam-truss modelling. In order to assess the behavior of the walls more effectively, it is beneficial to establish limit states that monitor tensile/compressive strain. These performance criteria enable the prediction of reinforcement failure or yielding, the occurrence of confined concrete crushing, and ultimately, the failure of the wall:

- **Crushing of confined concrete**: This state is reached when the first vertical element of confined concrete within the beam-truss model exhibits a compressive strain lower than a predetermined limit of $\epsilon_{lim} = -0.015$ or -1.5%. This criterion is applied solely to the vertical confined boundary elements of the walls.

- **Yielding of steel**: This condition is met when the first longitudinal steel rebar of the wall achieves its yield tensile strain in tension. Each wall's corresponding steel properties table provides the yield tensile strain denoted as ϵ_y. For example, for UW1's 12 $[mm]$ rebars, $\epsilon_{lim} = 0.0029$ or 0.29%.

- **Rupture of steel**: This limit is exceeded when the first longitudinal steel bar of the wall reaches 60% of its ultimate tensile strain in tension. The ultimate strain is given for each rebar in their respective steel properties table as ϵ_u, e.g., for UW1's 12 $[mm]$ rebars, $\epsilon_{lim} = 0.6 \times 0.101 = 0.06$ or 6%.

- The **SMA start of plateau** represents the beginning of the plateau of the SMA along vertical elements. The strain is $\epsilon_{lim} = 0.01$ or 1% and can be observed on the model of SMA in Figure 2.19. This particular criterion is exclusively applied to the elements containing SMA in order to visualize the behavior of the SMA rebar.

- The **SMA end of plateau** represents the end of the plateau of the SMA along vertical elements. The strain is $\epsilon_{lim} = 0.06$ or 6% and can be observed on the model of SMA in Figure 2.19. This particular criterion is exclusively applied to the elements containing SMA in order to visualize the behavior of the SMA rebar.
- **Spalling of diagonal concrete elements**: This criterion occurs when a diagonal concrete element displays a compressive strain lower than a predetermined value of $\epsilon_{lim} = -0.0035$ or -0.35%.

These criteria have been established based on those utilized in the work of Hoult et al. (2023) [20] to model the failure behavior of UW1 and UW2. It is crucial to note that these performance criteria do not necessarily signify failure, rather, they serve as indicators of the wall's behavior. The author acknowledges that these values are not accurate for all model, as using the same confined concrete criterion for UWS1 and UW1, despite differing confinements, is not ideal.

Paulay and Priestley [24] presented an equation in 1992 to determine strain values based on confinement factors, but its results were approximately twice the ϵ_{lim} of -0.015 for UW1, leading to overestimations and was not employed. Buckling criteria also exist but were not utilized.

Importantly, these criteria function as flags that inform the user of strain reaching certain levels. They do not directly influence the rest of the analysis. For other criteria, like buckling, or more precise ones, further researches are necessary, and consultation with Christophe Saegerman's parallel thesis work on BTM could provide valuable insights.

Chapter 3

Model Validation

Before modelling the UWS1 and UWS2 units for the All4wAll project, a series of validations must be conducted. These validations encompass selecting the optimal mesh for the beam-truss model, employing the appropriate material model, fine-tuning program parameters, and comprehensively understanding all the features of Seismostruct. Geometrical nonlinearities will be ignored to avoid a misunderstood behavior on ultimate loading of slender walls.

This chapter involves the numerical modelling of various walls, followed by a comparison of the results with their corresponding experimental outcomes. The units to be modelled include UW1 and UW2 from Hoult et al. (2022) [5]; IR1, IR2, and IR3 from Ile and Reynouard (2005) [9]; RC+SMA from Almeida et al. (2020) [11]; and CEA1 and CEA3 from Combescure et al. (1999) [10].

3.1 Quasi-static cyclic and torsional tests with UW1 and UW2

UW1 and UW2 are U-shaped walls tested at UClouvain, Louvain-La-Neuve, Belgium, at the Institute of Mechanics, Materials and Civil Engineering (IMMC). Like developed in Section 2.2.1.1, these geometrically identical walls were tested on a quasi-static cyclic North-South loading for UW1 and a quasi-static cyclic torsional loading for UW2. These U-shaped walls were tested by a part of the same team than UWS1 and UWS2 will be in the All4wAll project. Moreover, the section of UW1 and UW2 are similar to UWS1 and UWS2, while the reinforcement is slightly different (further details of the ALL4wALL units in Section 4.1.1.1).

3.1.1 Geometry

The properties of the walls were taken from Hoult et al. 2022 [5] and 2023 [20] and are depicted in Figure 3.1. The length of the flanges is 1050 [mm] and the length of the web is 1300 [mm]. The wall is 100 [mm] thick and has a height of 2250 [mm]. For reasons of clarity, a compass, with the cardinal directions, is represented on section views to differ the flanges and explain the loading directions.

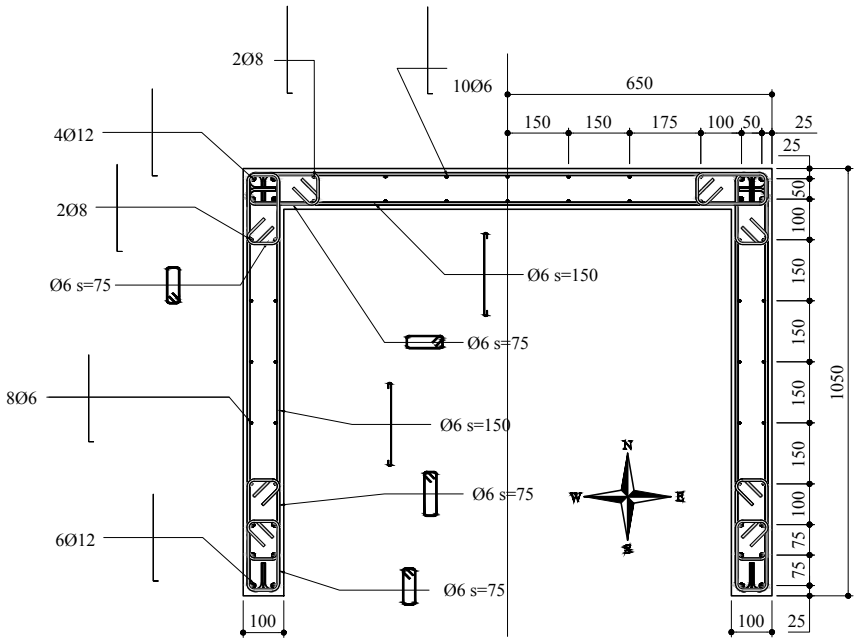


Figure 3.1: Cross section and reinforcement of UW1 and UW2 [Unit: mm].

Figure 3.1 also illustrates the reinforcement bars, i.e., rebars. In each flange, there are eight longitudinal rebars with a diameter of 6 [mm] and two longitudinal rebars with a diameter of 8 [mm]. In the web, there are ten longitudinal rebars with a diameter of 6 [mm] and four longitudinal rebars with a diameter of 8 [mm]. At the two intersections between the web and the flanges, i.e, the corners, there are four longitudinal rebars with a diameter of 12 [mm]. Additionally, at each flange boundary, there are six longitudinal rebars with a diameter of 12 [mm]. Regarding the transverse reinforcement, each corner of the wall and flanges boundary have two sets of hoops with a diameter of 6 [mm]. These hoops are spaced 75 [mm] apart. Furthermore, there are two sets of 6 [mm] rebars spaced 150 [mm] apart that cross the full length of the web and flanges.

During the UW1 test, the wall was subjected to an overturning moment to simulate a wall height of 6.72 $[m]$ so, the wall was modelled with a 6.72 $[m]$. It is easier and more accurate to model the real shear span wall and measure it at the tested height (2.25 $[m]$ for this wall) than trying to apply the right overturning moment with the real experimental size of the wall. An axial load ratio (ALR) of 5% was applied on three vertical actuators. The position of those, not exactly on the center of mass of the wall, changes the shear span or effective height to approximately 5.9 $[m]$ and 7.2 $[m]$ pushing towards North and South respectively.

The plan and elevation view of the beam-truss model for UW1 are depicted in Figure 3.2. The section is divided into eleven elements and the height is divided into twenty-one portions of 320 $[mm]$.

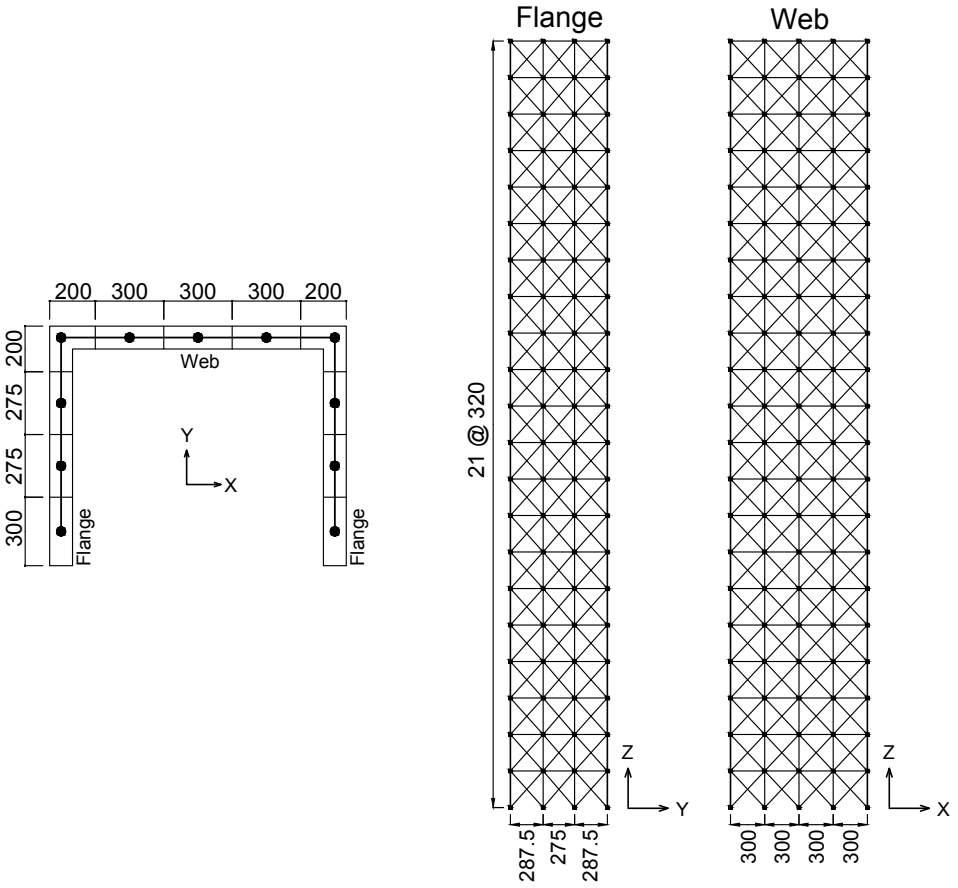


Figure 3.2: Plan and elevation views of the beam-truss model of UW1 [Unit: mm].

UW2 was modelled with its real height of 2.25 $[m]$ because in contrast to the wall UW1 in the Section 3.1, no additional overturning moment was added.

Figure 3.3 represents the plan and elevation view of the beam-truss model for UW2. The section is divided into eleven elements and the height is divided into three portions of 590 $[mm]$ and one of 480 $[mm]$.

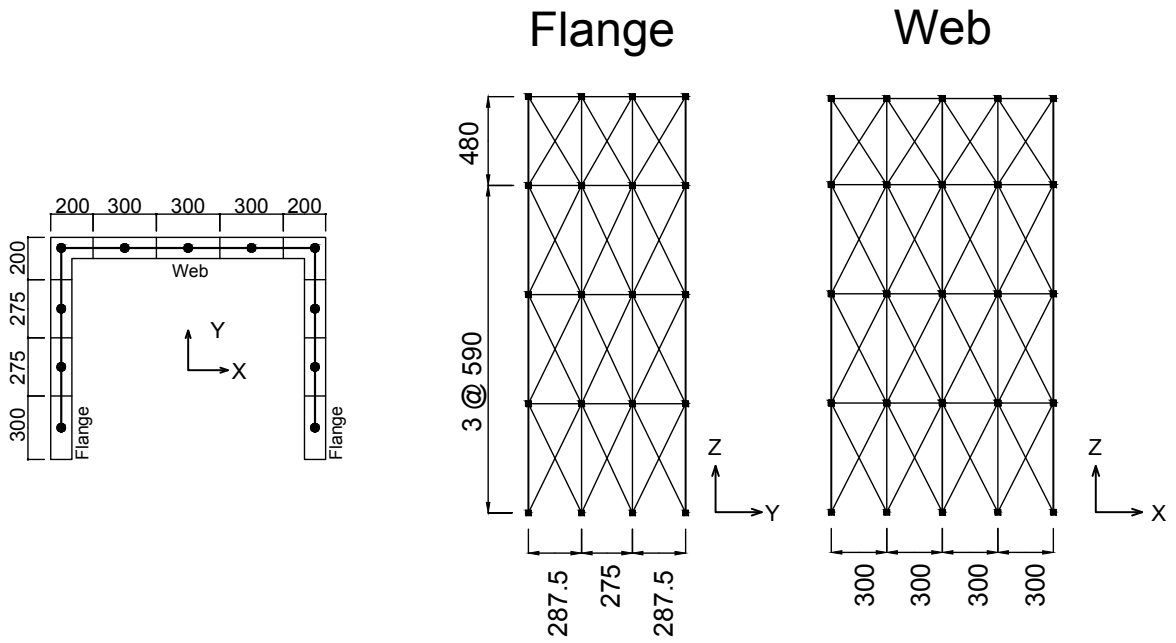


Figure 3.3: Plan and elevation views of the beam-truss model of UW2 [Unit: mm].

For both wall vertical and horizontal elements are modelled with inelastic displacement-based frame elements whereas the diagonal elements are modelled with nonlinear truss elements. Other elements such as elastic beam element with high rigidity are used to be able to apply the loads at the exact location or to represent the collar. A three-dimensional visualization of the modelled walls in Seismostruct is illustrated in Appendix B.

3.1.2 Material properties

The design concrete strength at 28 days was C30/37 $[MPa]$ but tests were conducted to determine the exact strength value at the moment of the experiment. Similarly, steel rebars were tested and the mean value of the results was utilized. These are class C steel to ensure ductility and energy dissipation. Values that are employed in the beam-truss

model are specified in Table 3.1 for the concrete of UW1 and UW2 and Table 3.2 for the steel of the rebars. The same steel for both wall were employed.

In Seismostruct, it's not possible to implement two distinct properties for longitudinal rebars within the same element. To address this limitation, 8 $[mm]$ rebars will have the same properties than the 6 $[mm]$ rebars. The difference is negligible.

Table 3.1: UW1 and UW2 concrete mechanical properties.

Properties	f_c	f_t	E_c	ϵ_c	γ
Unit	MPa	MPa	GPa	%	kN/m^3
UW1	38.2	3.07	29	0.2	21.7
UW2	37.1	2.88	25.9	0.2	22

Where f_c is the concrete compressive cylinder strength at the day of testing, f_t is the tensile concrete strength, E_c is the concrete elastic modulus, ϵ_c is the strain at peak stress and γ is the specific weight.

Table 3.2: UW1 and UW2 steel mechanical properties.

Properties	d	f_y	f_u	E_s	ϵ_y	ϵ_u	α	γ
Unit	mm	MPa	MPa	GPa	%	%	%	kN/m^3
Value	6	550	676	207	0.27	9.5	0.66	78
	8	550	676	207	0.27	9.5	0.66	78
	12	580	690	199	0.29	10.1	0.56	78

Where d is rebar diameter, f_y is the yield tensile strength, f_u is the ultimate strength, E_s is the Young's modulus, ϵ_y is the yield strain, ϵ_u is the ultimate strain, α is the strain hardening parameter (see Formula 2.2) and γ is the specific weight.

All values that were not mentioned in the papers were assumed, using default settings from Seismostruct.

3.1.3 BTM results and comparison for UW1

North-South cyclic loading was applied on UW1. The analysis output and the results from experimental test are depicted in Figure 3.4, representing the displacement in $[mm]$ at a height of 2.25 $[m]$ and the base shear in $[kN]$. The numerical results after the experimental failure are not represented.

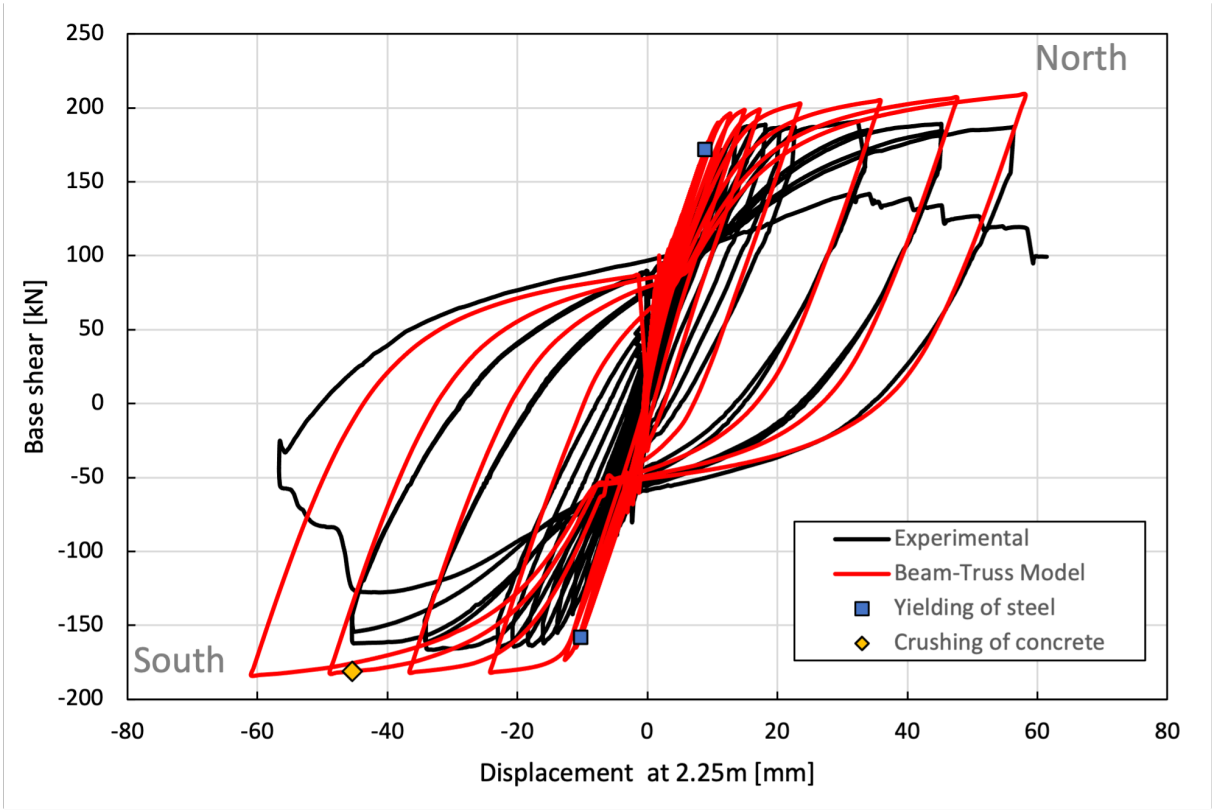


Figure 3.4: Force-displacement relationship of UW1, North-South cyclic loading.

Despite a relatively close correspondence, a small difference on either side of around 8% of the maximum value can be spotted. This disparity arises from the volunteer omission of geometrical nonlinearities, the impact on this wall is much more important than those analysed below because UW1 is taller. The P-delta effect omitted would have reduced the maximum base shear and would have result in a better correspondence.

According to Hoult et al. (2022) [5], the concrete in the bottom of the West flange is crushing during 1.5% and 2%, 33.75 $[mm]$ and 45 $[mm]$, cycles when the wall is going from North-to-South (negative base shear in Figure 3.4). These results match well with the performance criteria represented on the graph. The final rupture occurs when the

flange buckle and then, when the wall is coming at its initial position, the steel rebars reached the rupture. This mode of failure is not represented in the model because the criteria of 60% of the ultimate strain is not reached with such displacement.

The influence of the position of the application of axial loads can also be observed. The difference between North-to-South and South-to-North loading is noticeable due to the application of the load offset in the South direction.

3.1.4 BTM results and comparison for UW2

Torsional quasi-static cyclic loading was applied on UW2. Clockwise rotation being the positive sens. The incremental loading parameter was the imposed wall rotation (θ), measured by the two string pots, i.e., displacement sensors, at the ends of the flanges at a height of 2.25 $[m]$ during the experimental testing. The rotation can be calculated using Equation 3.1.

$$\theta = \frac{\delta_1 - \delta_2}{1.2} \tag{3.1}$$

where δ_1 and δ_2, in $[mm]$, correspond to the displacement of the West and East flange, and the 1.2 on the denominator is the lever arm distance, in $[m]$ between the two flanges (centre-to-centre); the resulting θ is in milliradian (i.e., $mrad = radian \times 10^3$).

The torque (T, in $[kNm]$) was calculated using Equation 3.2.

$$T = \frac{F_W - F_E}{2} \times 1.2 \tag{3.2}$$

where F_W and F_E are the forces, in $[kN]$, measured by the actuators from the flange to the West and East separated by a 2.4 $[m]$ lever arm in the model. During the numerical analysis, the lever arm was 1.2 $[m]$, this explains the value from Equation 3.2. This difference was considered to have a corresponding torque.

The analysis output and the results from experimental test are depicted in Figure 3.5, representing the rotation in $[mrad]$ at a height of 2.25 $[m]$ and the torque in $[kNm]$. The numerical results after the experimental failure are not represented.

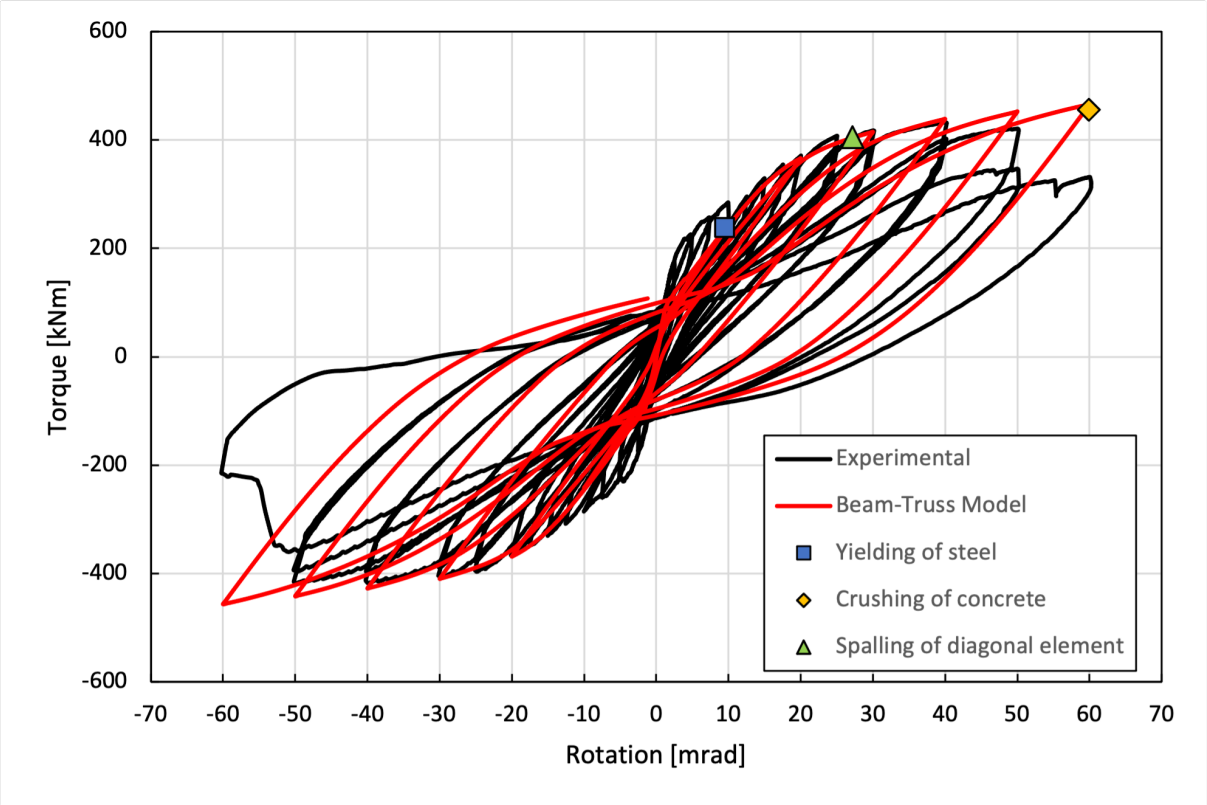


Figure 3.5: Torque-rotation relationship of UW2, torsional cyclic loading.

Despite a non exact initial stiffness, the results are globally satisfying regarding the resisting torque and are close to the numerical modelling of Hoult et al (2023) [20]. During the experimental campaign, unit UW2 was governed by shear cracks, in contrast to unit UW1, which was governed by flexural cracks.

During the modelling of the wall, an important influence of the elastic element strength located at the top of the wall to represent the collar was observed. The rigidity of these assumed rigid links are a prior element of modelling regarding wide-column modelling approach developed by Beyer et al., (2008) [17]. This paper describes formulas to set the rigidity of these elements to simulate the torsion. Unfortunately, these values cannot be calculated for the top of the collar in BTM, as the formula is specifically designed for WCM, e.g., using the spacing of the horizontal links not present in BTM, and does not consider the torsional strength present in the remaining portion of the wall.

To address this issue, two different approaches for modelling the top of the collar were examined, both yielding consistent results: the utilization of either a rigid diaphragm linking all the top nodes in both horizontal direction or employing elastic elements with manually

adjusted rigidity parameters. Because elastic frame elements where were implemented with other units without influencing the results, this approach was adopted. The main challenge is to have enough rigidity to support and transfer the top loads but not too much to avoid overestimating the torsion behavior.

This method was calibrated with the experimental result, which will not be possible for UWS1 because the experiment campaign has not started yet. But, in the UWS1 torsion analyses in Section 4.2.2, unlike with UW2, no influence of the rigidity of these links was perceived. Further investigation into the torsion behavior and the rigidity of elastic elements at the top of the wall would be worthwhile.

3.2 Quasi-static uniaxial and biaxial tests with IR1, IR2 and IR3

In 2005, Ile and Reynouard [9] described an experimental campaign of three U-shaped walls of real scale under quasi-static axial and biaxial loading. IR1, IR2 and IR3 wall were respectively tested on a cyclic North-South, East-West and biaxial "butterfly" (depicted in Figure 2.6) loading. They all have the identical section and reinforcement.

3.2.1 Geometry

Model a wall with a different scale, cross section, reinforcement and loading scenario than UW1 is also important for the model validation of quasi-static U-shaped wall. In the paper from Ile and Reynouard (2005) [9], X and Y direction are employed, X being positive in the West-to-East direction and Y positive in the South-to-North direction, it is represented in Figure 2.5 from Section 2.2.1.2.

The properties of the wall depicted in Figure 3.6. The length of the flanges is 1250 $[mm]$ and the length of the web is 1500 $[mm]$. The wall is 250 $[mm]$ thick and has a height of 3900 $[mm]$. For reasons of clarity, a compass representing the cardinal directions will be put on section views, this is mainly to differ the flanges and explain the loading direction and sense.

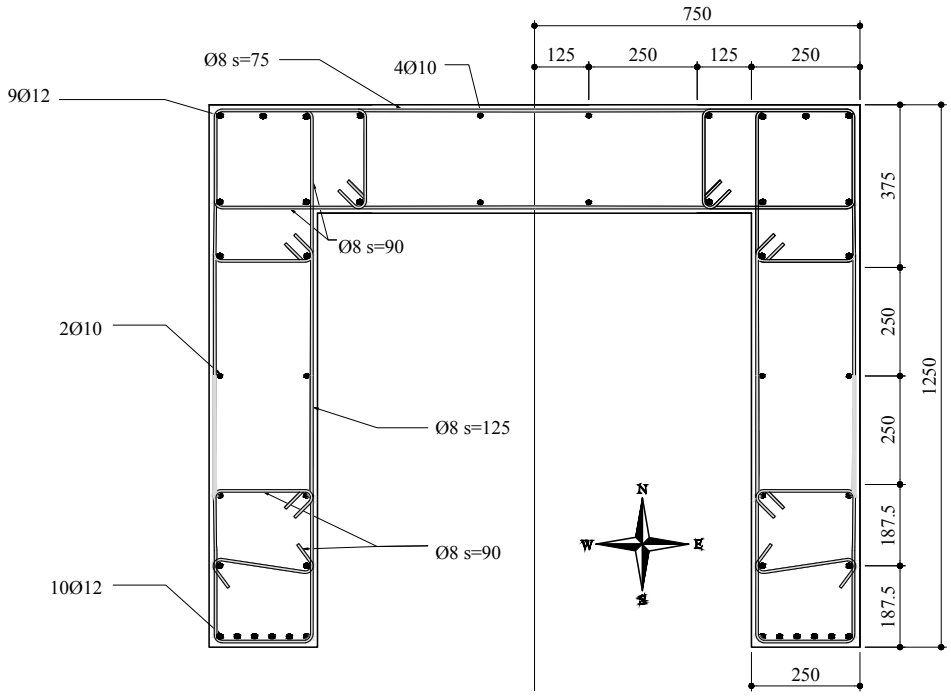


Figure 3.6: Cross section and reinforcement of IR [Unit: mm].

Figure 3.6 also illustrates the reinforcement. In each flange, there are two longitudinal rebars with a diameter of 10 [mm]. In the web, there are four longitudinal rebars with a diameter of 10 [mm]. At the two intersections between the web and the flanges, i.e, the corners, there are nine longitudinal rebars with a diameter of 12 [mm]. Additionally, at each flange boundary, there are ten longitudinal rebars with a diameter of 12 [mm].

Regarding the transverse reinforcement, each corner of the wall and flanges boundary have two sets of hoops with a diameter of 8 [mm]. These hoops are spaced 90 [mm] apart. Furthermore, there are two sets of 8 [mm] rebars spaced 75 [mm] apart that cross the full length of the web and spaced 125 [mm] apart in the flanges.

Figure 3.7 represents the plan and elevation view of the beam-truss model for this wall. The section is divided into eleven elements and the height is divided into ten portions of 360 [mm] and one of 300 [mm]. Vertical and horizontal parts are modelled with inelastic displacement-based frame elements whereas the diagonal elements are modelled with nonlinear truss elements. A three-dimensional visualization of the modelled walls in Seismostruct is illustrated in Appendix B.

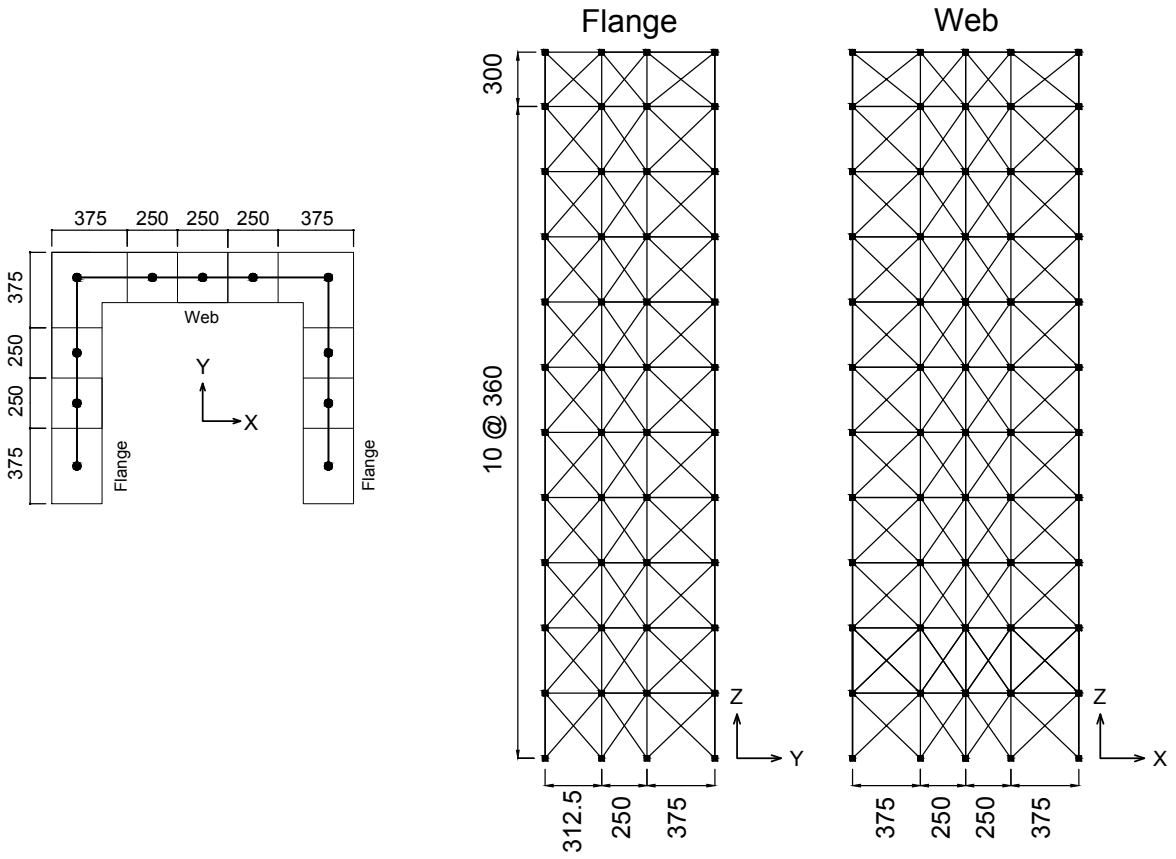


Figure 3.7: Plan and elevation views of the beam-truss model for IR [Unit: mm].

A three-dimensional visualization of the modelled walls in Seismostruct is illustrated in Appendix B.

3.2.2 Material properties

The design concrete strength at 28 days was C20/25 $[MPa]$ but tests were conducted to determine the exact strength value at the moment of the experiment. Similarly, steel rebars were tested and the mean value of the results were employed. Inputs employed in the beam-truss model are specified in Table 3.3 for the concrete and Table 3.4 for the steel of the rebars.

Table 3.3: IR concrete mechanical properties.

Properties	f_c	f_t	E	ϵ	γ
Unit	MPa	MPa	GPa	%	kN/m^3
IR1 and IR2	23.73	2.2	22.9	0.2	24
IR3	20.83	2.2	21.5	0.2	24

Table 3.4: IR steel mechanical properties.

Properties	d	f_y	f_u	E_s	ϵ_y	ϵ_u	α	γ
Unit	mm	MPa	MPa	GPa	%	%	%	kN/m^3
Value	8	557	642	207	0.2	25	0.17	78
	10	525	617	207	0.2	24.2	0.18	78
	12	516	615	199	0.2	24.8	0.2	78

3.2.3 BTM results and comparison for IR1

North-South quasi-static cyclic loading was applied on IR1 along its weak axis. The results of the analysis, along with the results from experimental test are displayed in Figure 3.8, representing the displacement in $[mm]$ at a height of 3.9 $[m]$ and the base shear in $[kN]$. Three cycles of 40, 80 and 120 $[mm]$ were applied on the specimen. The experimental curve is a digitization of a figure from Ile and Reynouard (2005) [9], with the original experimental results figures provided in Appendix A.

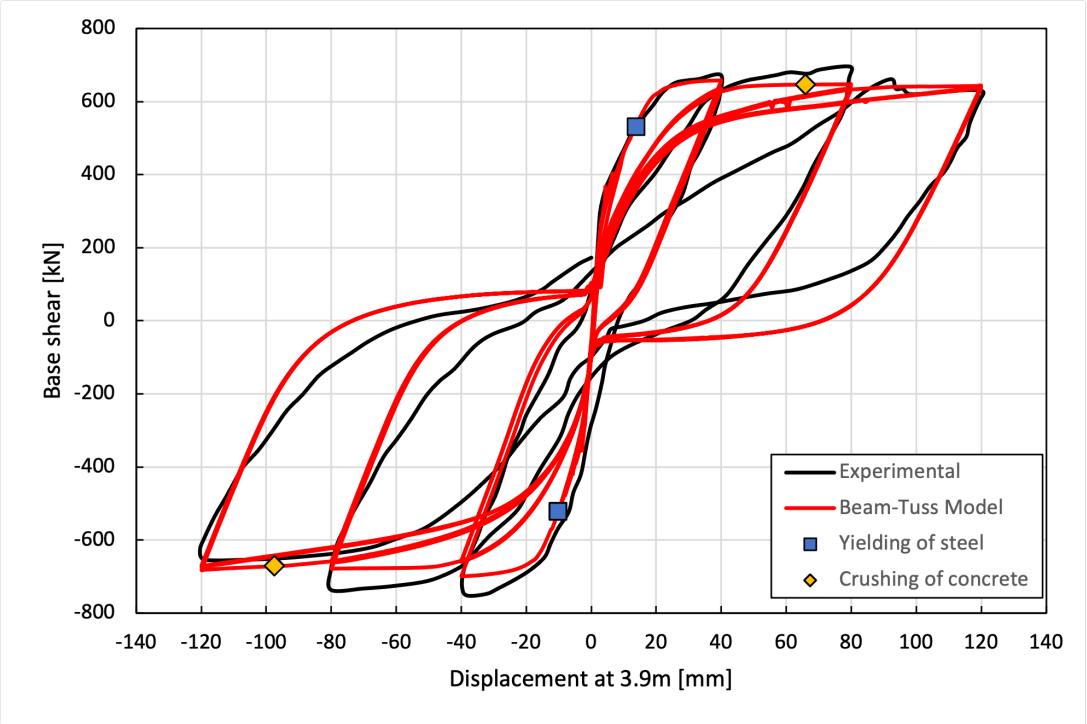


Figure 3.8: Force-displacement relationship of IR1, North-South cyclic loading.

As indicated in the experimental paper, the crushing of the confined concrete occurs during the 80 $[mm]$ and was correctly simulated by the performance criteria. The following of the experimental results are influence by this failure but are still well represented by the model. The axial load being applied exactly at the geometrical center of mass of the wall, the results are slightly symmetrical unlike for UW1 in Section 3.1.

3.2.4 BTM results and comparison for IR2

East-West quasi static cyclic loading was applied on IR2 along its strong axis. The results of the analysis, along with the results from experimental test are displayed in Figure 3.9, representing the displacement in $[mm]$ at a height of 3.9 $[m]$ and the base shear in $[kN]$. The wall being symmetrical along the NS axis, pushing through East or West is similar. Three cycles of 40, 80 and 120 $[mm]$ were applied on the specimen. The experimental curve is a digitization of a figure from Ile and Reynouard (2005) [9], with the original experimental results figures provided in Appendix A.

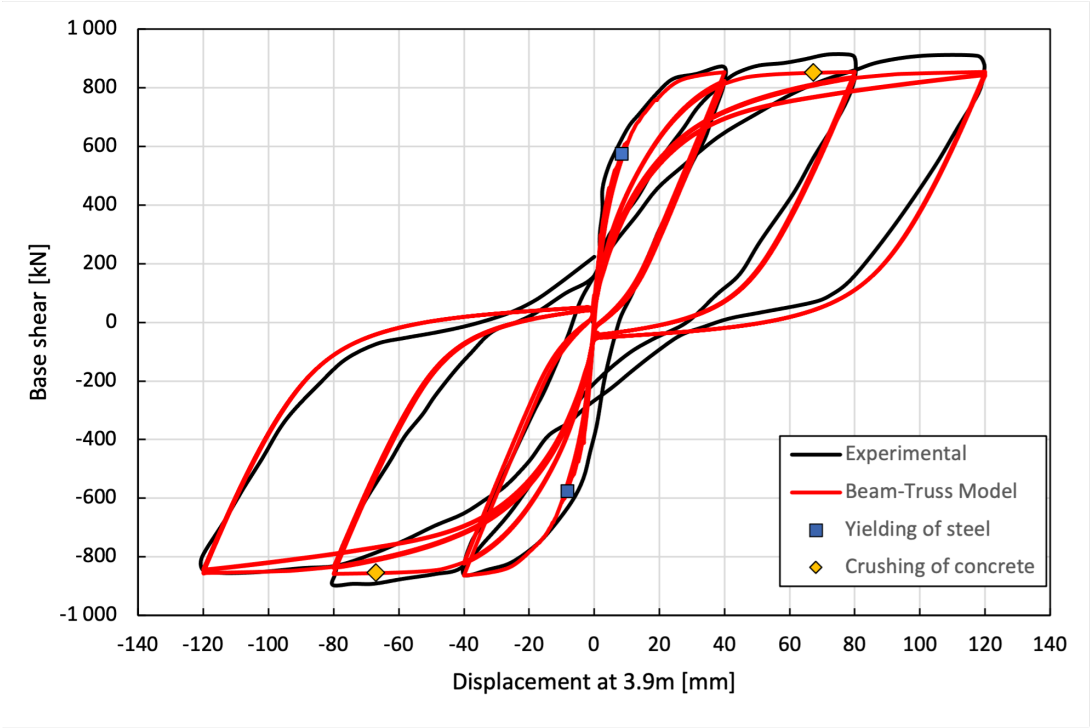


Figure 3.9: Force-displacement relationship of IR2, East-West cyclic loading.

As indicated in the experimental paper, the wall failure was due to the steel rebars failure in the flange. This behavior is not correctly depicted on the Figure 3.9, even if the performance criteria had reached 96%, so a good numerical simulation of the failure can be assumed. The difference between strong/major and weak/minor axis can be spotted easily regarding IR1 and IR2 results.

3.2.5 BTM results and comparison for IR3

Biaxial quasi static cyclic loading was applied on IR3 along a "butterfly" path depicted previously in Figure 2.6. The results of the analysis, along with the results from experimental test are displayed in Figure 3.10 and 3.11. These are represented the NS (Y in the paper) and the EW (X) displacement in $[mm]$ at a height of 3.9 $[m]$ and the base shear in $[kN]$, while Figure 3.12 depicted the base shear in the NS (Y) direction regarding the EW (X) direction. It should be noted that in the analyses, a positive convention is adopted for pushing towards the South and East. Two cycles of 40 and 80 $[mm]$ were applied on the specimen. The experimental curve are a digitization of the envelope of figures from Ile and Reynouard (2005) [9], with the original experimental results figures provided in Appendix A.

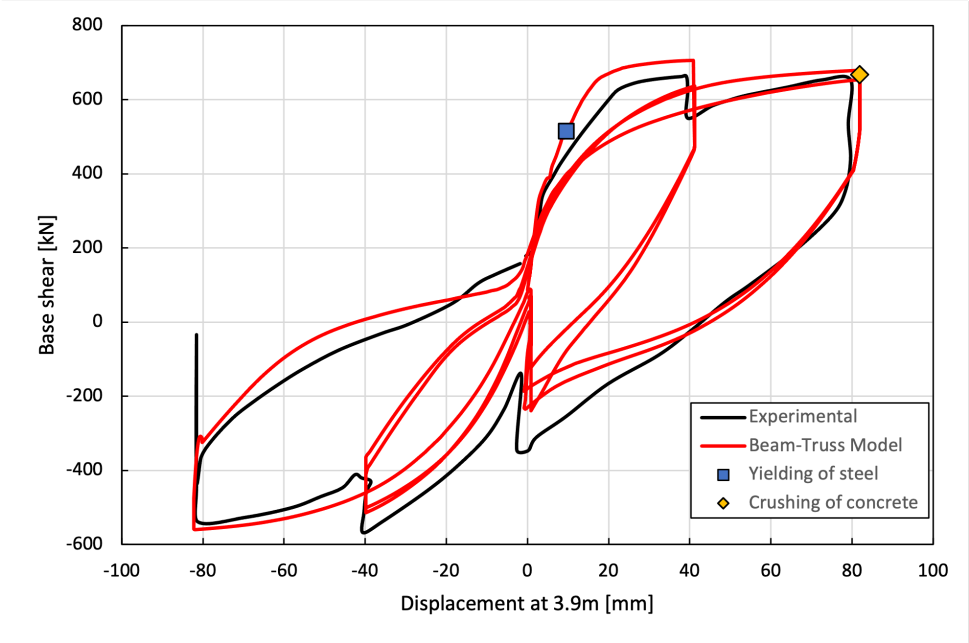


Figure 3.10: Force-displacement relationship in North-South direction of IR3, biaxial cyclic loading.

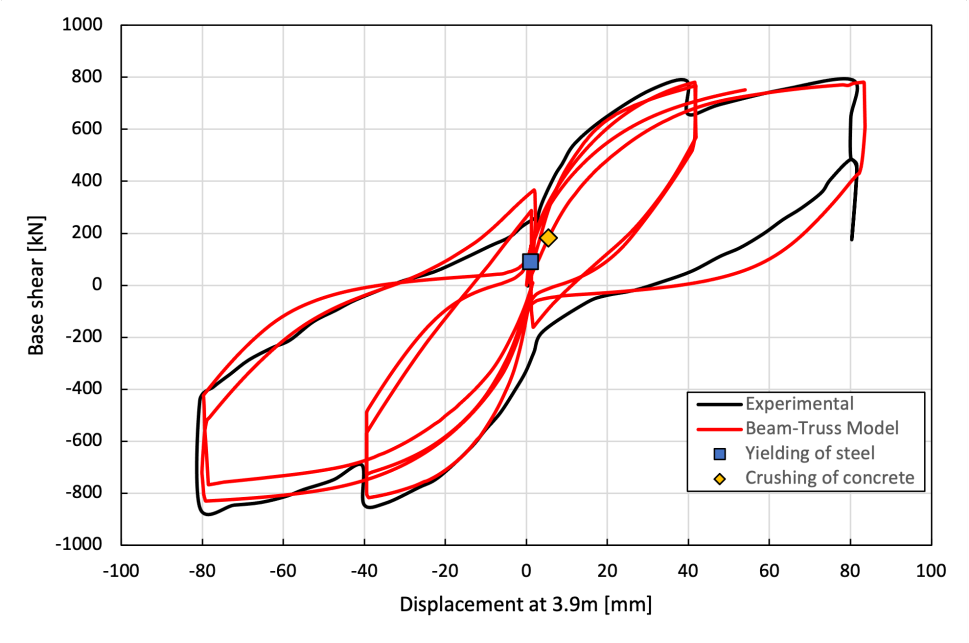


Figure 3.11: Force-displacement relationship in East-West direction of IR3, biaxial cyclic loading.

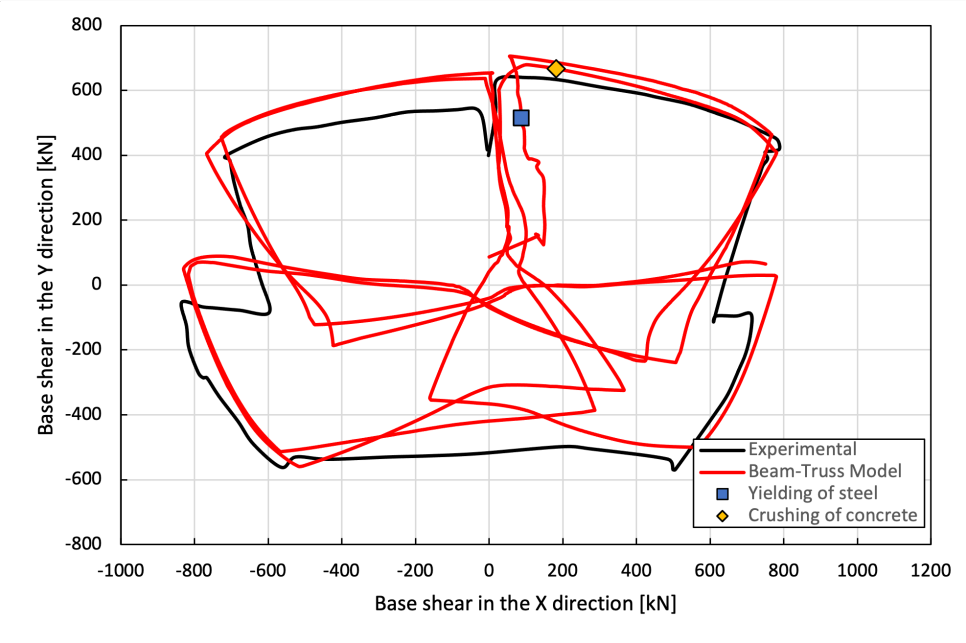


Figure 3.12: Forces in X and Y direction of IR3, biaxial cyclic loading.

As indicated in the experimental paper, the failure of the wall was due to cyclic degradation and buckling of the rebars, two performance criteria not employed in this thesis, the simulation of failure could not be performed. The numerical modelling of tests IR1, IR2 and IR3, along the UW1 and UW2, yielded highly satisfactory results, thus validating the utilization of BTMs to simulate the behavior UWS1 and UWS2 under quasi-static loading. Further exploration of dynamic tests and the effects of SMA will be discussed in the upcoming sections.

3.3 Quasi-static cyclic test with RC+SMA

An experimental campaign described by Almeida et al. (2020) [11] investigated I-shaped planar shear walls with and without shape memory alloy rebars (SMA). The RC-only wall, referred to as "RC", experienced foundation failure, which affected the results. Due to this reason, no further analysis will be conducted on this wall. The other wall including SMAs, referred to as "RC+SMA", provides valuable insights into the influence of SMA under cyclic loading and assesses the SMA model in Seismostruct.

This wall is planar, which deviates from the main focus of this study on non-planar walls. Nonetheless, due to the scarcity of experimental data for non-planar RC walls with SMAs, the dataset obtained from the experiments on this planar wall is utilized for validation purposes.

3.3.1 Geometry

The properties of the wall were taken from Almeida et al. (2020) [11] and are represented in Figure 3.13. The thickness of the wall is 200 [mm] and its length is 1200 [mm]. The wall has a height of 1200 [mm] but its effective height is 4320 [mm] due to a shear span ratio of 3.6. An additional overturning moment was applied to recreate this shear span ratio.

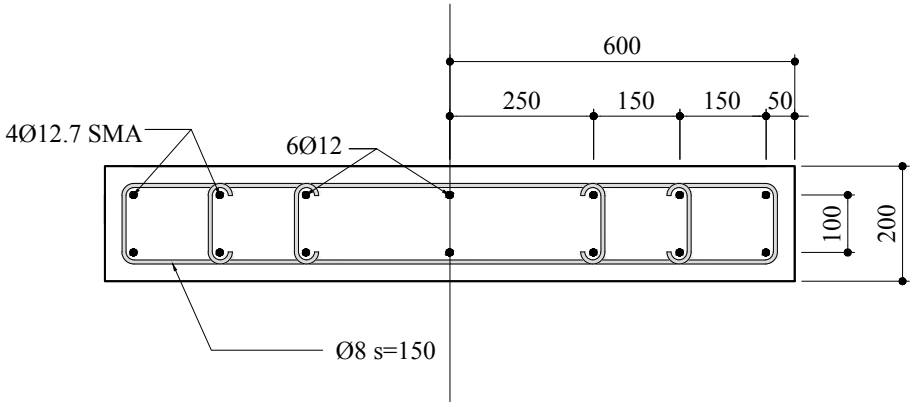


Figure 3.13: Cross section and reinforcement of RC+SMA wall [Unit: mm].

Figure 3.13 also illustrates the reinforcement. In each boundary region, there are four longitudinal SMA rebars with a diameter of 12.7 [mm] and six longitudinal steel rebars with a diameter of 12 [mm] in the center of the wall.

Regarding the transverse reinforcement, each pair of transversal rebar has a stirrup of 8 [mm]. Furthermore, there are two sets of 8 [mm] rebars spaced 150 [mm] apart that cross the full length of the wall.

Figure 3.7 represents the plan and elevation view of the beam-truss model for this wall. The section is divided into four elements and the height is divided into eleven portions of 385 [mm] and one of 85 [mm]. These values comes from the height of the SMA rebars of 385 [mm]. Vertical and horizontal elements are modelled with inelastic displacement-based frame elements whereas the diagonal elements are modelled with nonlinear truss elements. Other elements such as elastic beam element with high rigidity are used to be able to apply the loads at their exact location or to represent the collar. A three-dimensional visualization of the modelled walls in Seismostruct is illustrated in Appendix B.

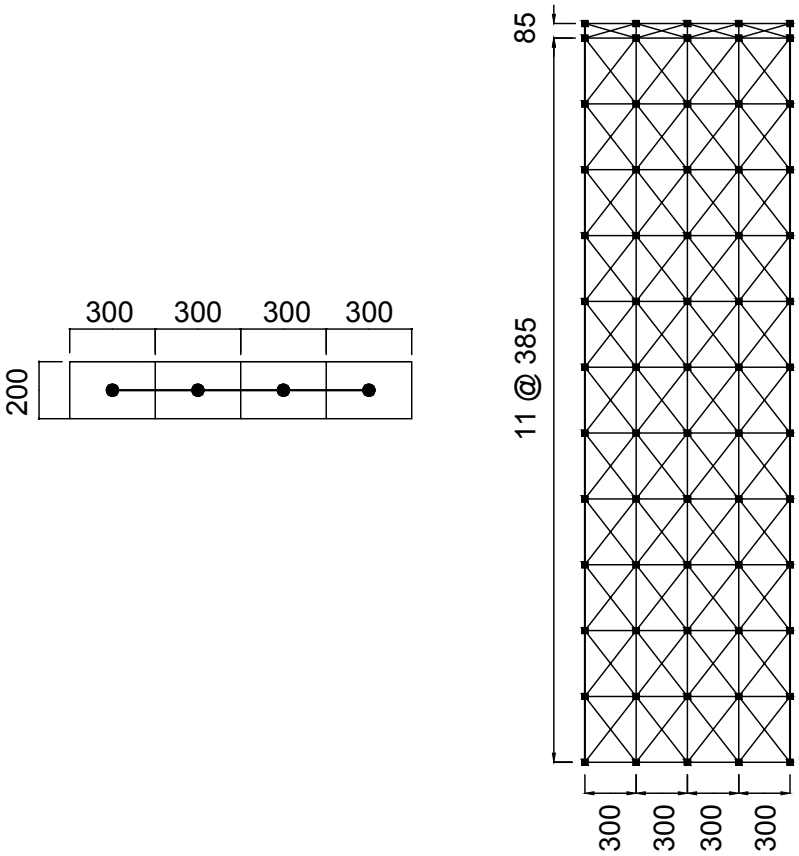


Figure 3.14: Plan and elevation views of the beam-truss model for RC+SMA [Unit: mm].

3.3.2 Material properties

Tests were conducted to determine the exact strength of the concrete at the moment of the experiment. Similarly, steel rebars were tested and the mean value of the results were used. Values that are employed in the beam-truss model are specified in Table 3.5 for the concrete, Table 3.6 for the steel rebars and Table 3.7 for the SMA the rebars.

Table 3.5: RC+SMA concrete mechanical properties.

Properties	f_c	f_t	E	ϵ	γ
Unit	MPa	MPa	GPa	%	kN/m^3
Value	39.36	3.9	35.1	0.23	24

Table 3.6: RC+SMA steel mechanical properties.

Properties	d	f_y	f_u	E_s	ϵ_y	ϵ_u	α	γ
Unit	mm	MPa	MPa	GPa	%	%	%	kN/m^3
Value	12	517	635	205	0.2	7.6	0.78	78

Table 3.7: RC+SMA shape memory alloy mechanical properties.

Properties	d	E	σ_{AMs}	σ_{AMf}	σ_{MAs}	σ_{MAf}	γ
Unit	mm	GPa	MPa	MPa	MPa	MPa	kN/m^3
Value	12.7	31	319	349	73	32	65

Where d is rebar diameter, E is the modulus of elasticity, σ_{AMs} is the austenite to martensite start stress, σ_{AMf} is the austenite to martensite finish stress, σ_{MAs} is the martensite to austenite start stress, σ_{MAf} is the martensite to austenite finish stress, and γ is the specific weight.

3.3.3 BTM results and comparison

The RC+SMA planar wall was tested under quasi-static cyclic loading in the in-plan direction of the unit. The results of the analysis, along with the results from experimental test are depicted in Figure 3.15, representing the displacement in $[mm]$ at a height of 2.2 $[m]$ and the base shear in $[kN]$. Several cycles up to 60 $[mm]$ were applied on the specimen. The experimental curve comes from the Dataverse [11] The numerical results after the experimental failure are not represented.

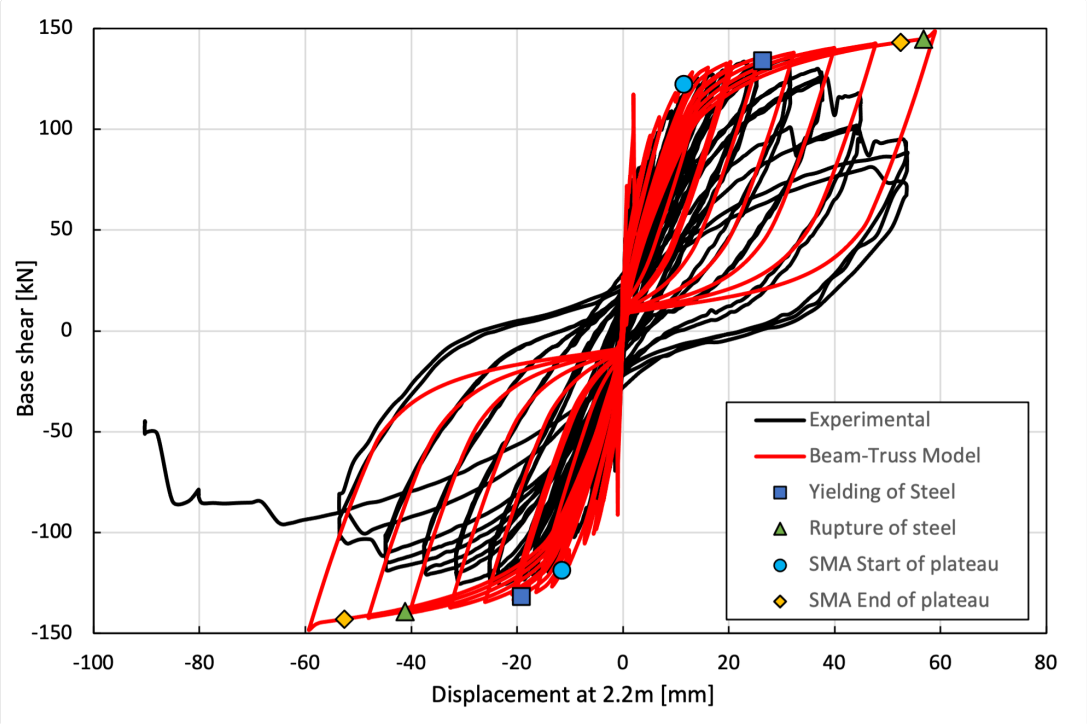


Figure 3.15: Force-displacement relationship of RC+SMA unit, quasi-static cyclic loading.

Although the effective stiffness and maximum base shear strength are well represented in the BTM analysis, the absence of residual displacement is notable. This is due to the model of shape memory alloy available in Seismostruct. During a 40 $[mm]$ cycle, a distinct sound of a steel rebar rupturing was audible. This behavior is aptly captured by the "rupture of steel" criterion. Furthermore, it's noteworthy that the first broken rebar in the numerical model aligns with that observed during the experimental campaign.

Residual displacement of UWS2 will not be considered as fully reliable with this SMA model. But, UWS2 being very different in loading, geometry and reinforcement than RC+SMA, the influence of the SMA model regarding the experimental results would be insightful to observe.

3.4 Dynamic tests with CEA1 and CEA3

The experimental campaign described by Combescure et al. (1999) [10] was a program of four walls with the same cross section but different stirrups spacing under dynamic loading. Tests were carried out at the CEA center, the four units will be denoted as CEA0, CEA1, CEA2 and CEA3. For the sake of brevity, only CEA1 and CE3 will be modelled.

This experiment was relevant for the model validation because it is one of the only U-shaped wall tested with a dynamic loading, on a shake table. The campaign had problems during construction phase because the footing of the walls was lacking of concrete and inappropriate steel rebars were employed, as developed in Section 2.2.2.1. Moreover, the tests are not recent and the experimental data, like ground motion input or corresponding results, come from the poor quality figures of the paper and digitization was not very accurate. Despite that, results are interesting but have to be taken for what it's worth.

3.4.1 Geometry

The properties of the CEA1 wall were obtained from Combescure et al. (1999) [10] and are represented in Figure 3.16. The length of the flanges is 750 $[mm]$ and the length of the web is 900 $[mm]$. The wall is 150 $[mm]$ thick and has a height of 3000 $[mm]$.

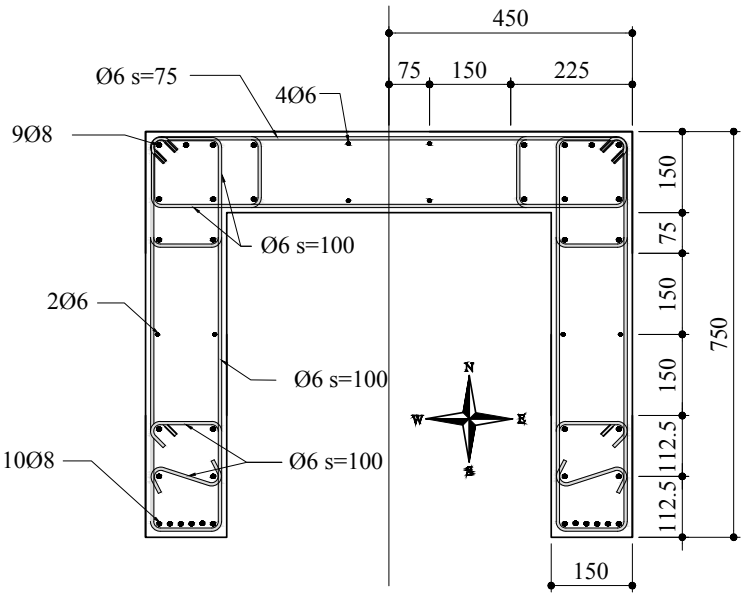


Figure 3.16: Cross section and reinforcement of CEA1 [Unit: mm].

For reasons of clarity, a compass representing the cardinal directions will be put on section views, this is mainly to differ the flanges and explain the loading direction and sense. Figure 3.6 also illustrates the reinforcement. In each flange, there are two longitudinal rebars with a diameter of 6 $[mm]$. In the web, there are four longitudinal rebars with a diameter of 6 $[mm]$. At the two intersections between the web and the flanges, i.e, the corners, there are nine longitudinal rebars with a diameter of 8 $[mm]$. Additionally, at each flange boundary, there are ten longitudinal rebars with a diameter of 8 $[mm]$.

Regarding the transverse reinforcement for CEA1, each corner of the wall and flanges boundary have sets of hoops with a diameter of 6 $[mm]$. These hoops are spaced 100 $[mm]$ apart. Furthermore, there are two sets of 100 $[mm]$ rebars spaced 100 $[mm]$ apart that cross the full length of the web and the flanges.

Table 3.8 describes the other units with a different spacing of the confinement reinforcement in the boundary regions.

Table 3.8: Spacing of the hoops for each CEA unit.

Wall	Spacing at flange ends	Spacing at corners.
CEA1	100	100
CEA2	40	100
CEA0 & CEA3	40	40

Figure 3.7 represents the plan and elevation view of the beam-truss model for this wall. The section is divided into eleven elements and the height is divided into twelve portions of 250 $[mm]$. Vertical and horizontal parts are modelled with inelastic displacement-based frame elements whereas the diagonal elements are modelled with nonlinear truss elements. The wall has three additional masses of 6.45 $[ton]$ each on its top, as depicted in Figure 2.7 from Section 2.2.2.1. The measurement point of the wall is considered at the center of the second mass so 4.14 $[m]$. All the elements to link the center of the masses, represented by mass elements, are elastic beam elements with high rigidity values that do not influence the results. A three-dimensional visualization of the modelled walls in Seismostruct is illustrated in Appendix B.

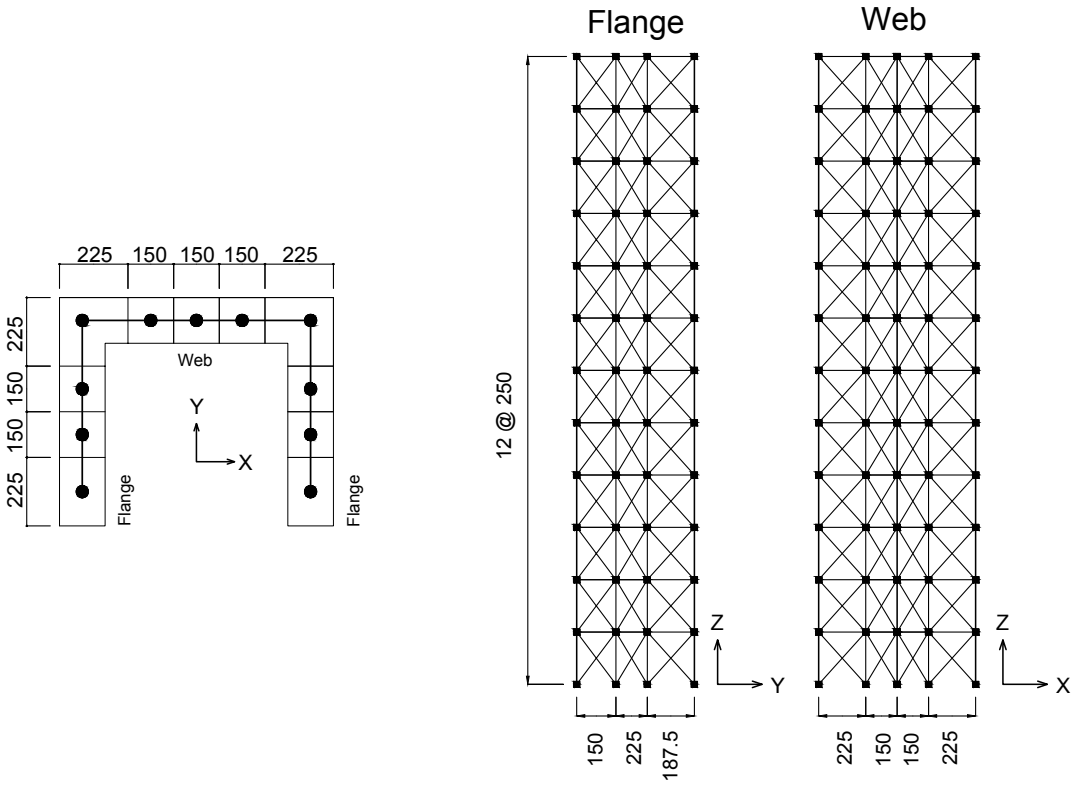


Figure 3.17: Plan and elevation views of the beam-truss model of CEA1 [Unit: mm].

3.4.2 Material properties

The design concrete strength at 28 days was C25/30 [MPa] but tests were conducted to determine the exact strength value at the moment of the experiment. Similarly, steel rebars were tested and the mean value of the results were used. Values that are employed in the beam-truss model of CEA1 are specified in Table 3.9 for the concrete and Table 3.10 for the steel of the rebars. The emphasis here lies in the low ultimate strain of the steel, which does not conform to the Eurocode 8 recommendations for C class rebars in high seismic areas.

Table 3.9: CEA1 concrete mechanical properties.

Properties	f_c	f_t	E	ϵ	γ
Unit	MPa	MPa	GPa	%	kN/m^3
Value	32.3	3.64	25.9	0.2	24

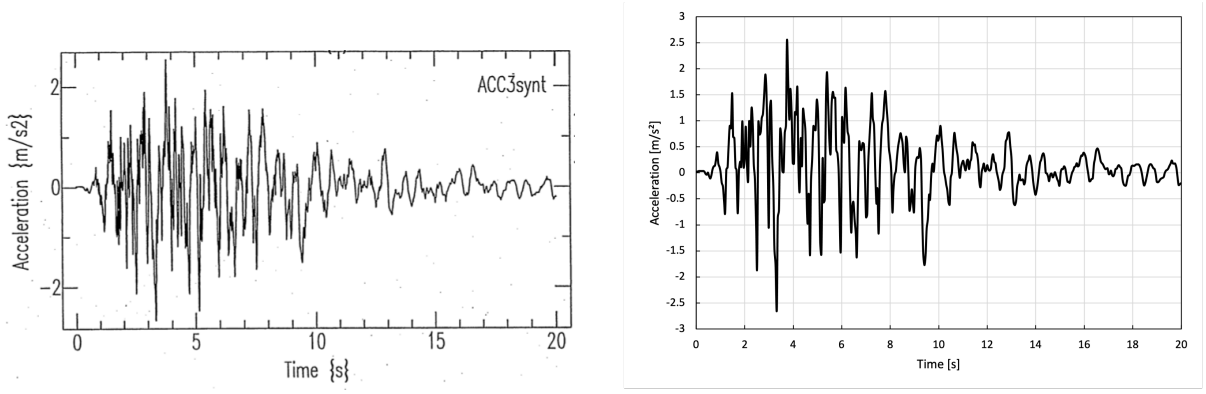
Table 3.10: CEA1 steel mechanical properties.

Properties	d	f_y	f_u	E_s	ϵ_y	ϵ_u	α	γ
Unit	mm	MPa	MPa	GPa	%	%	%	kN/m^3
Value	6	604	625	190.7	0.2	2.47	0.49	78
	8	643	660	206.3	0.2	2.61	0.37	78

3.4.3 Ground motion input

The data for the dynamic input of the shake table was not available. A digitization of the ground motion picture was performed using a Matlab program developed by R. Hoult. The applied ground motion was not clearly mentioned but it was inspired from the earthquake of San Fernando, February 09, 1971, at the station 900 South Fremont Av., Basement, Alhambra. A main assumption during this analysis is to use this dynamic input even if it is not exactly the one applied during the test, but a very close one.

Furthermore, the loss of precision during image digitization creates unwanted frequencies. In Figure 3.18a, the Figure available from Combescure et al. (1999) [10] and in Figure 3.18b, its digitization. The latter is then scaled by a factor of $\sqrt{0.6}$ in time, 0.6 being the scale, to have a total time of 15.5 $[s]$. With this similitude law, the acceleration remains unchanged but the time scale is contracted in order to reduce the displacement. Further details about the similitude law for earthquake scale model are available in Pinho (2000) [25]. The ground motion is finally scaled in amplitude regarding the test, i.e., for a test of 0.2 $[g]$, the ground motion will be scaled to have a peak ground acceleration (PGA) of $0.2 \cdot g = 1.962[m/s^2]$.



(a) (b)

Figure 3.18: Ground motion (a) from Combescure et al. (1999) and (b) digitized.

The digitization procedure involves transforming a figure into a numerical dataset that can be used for plotting, analysis, and other purposes. This can be achieved manually using tools like WebPlotDigitizer [26]. However, for larger datasets or cases where precision is crucial, as with ground motion records manual, methods can be time-consuming or insufficient. In such cases, specialized programs can be developed to analyze images and perform digitization with a certain level of accuracy. It is important to note that the effectiveness of this approach depends on the quality of the figure and the presence of potential distortions or obstructions.

3.4.4 BTM results and comparison

A first analysis was conducted on CEA1, to see the influence of the cumulative loading and almost no difference was perceived between a wall that has undergone only a test at 0.63 $[g]$ and a wall (CEA1) that has undergone a test of 0.2 $[g]$, then a test of 0.26 $[g]$ and finally the test of 0.63 $[g]$. This effect may be linked with the poor steel ductility. To solve this problem, the coefficient of the Rayleigh damping model was adjusted regarding each test to simulate the cumulative damages. The damping model was calculated using the first modal frequency of 0.17 $[s]$ and the third modal frequency of 0.019 $[s]$. The first mode being along the weak axis and the third is torsion. These results come from eigenvalues analysis in Seismostruct, further details about the damping model are presented in Section 4.5.1

Given the challenge of accurately fitting the displacement-time graph due to inaccuracy in the dynamic input, a comparison will be made based on the shear force-displacement graph. The envelope of the experimental results, as presented by Combescure et al. (1999) [10], is used for this purpose. Before conducting dynamic tests, a pushover analysis can be interesting to verify the model, the results are illustrated in Figure 3.19.

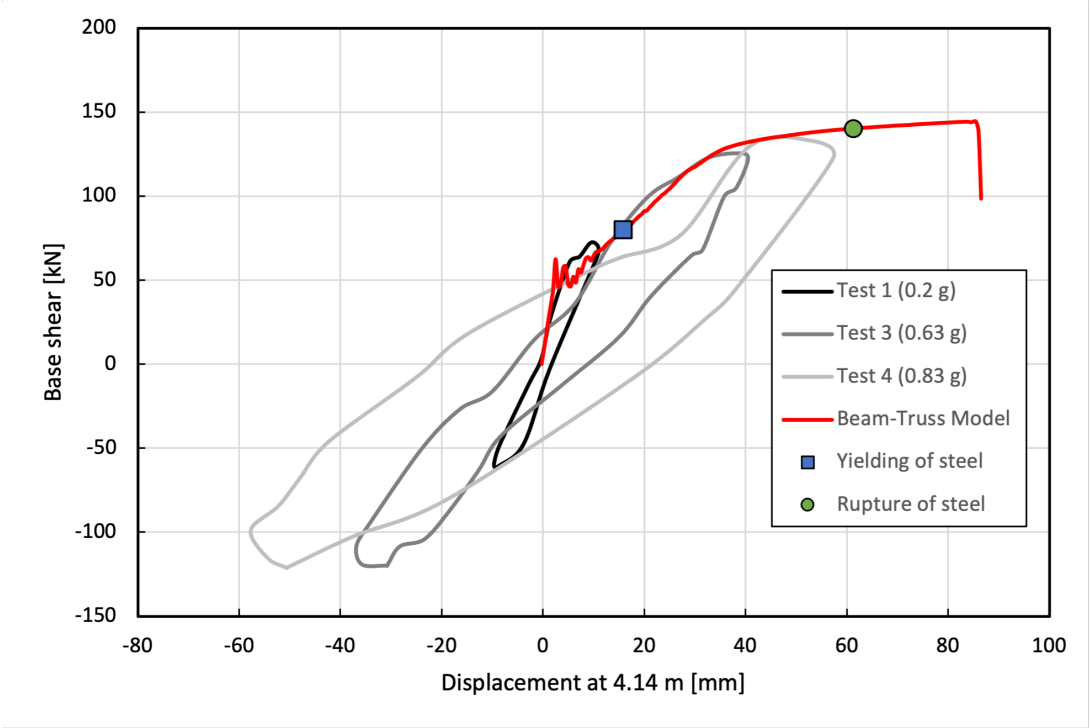


Figure 3.19: Force-displacement relationship of CEA1, pushover from North-to-South and experimental results comparison.

Only experimental results for test 1, 3 and 4 of CEA1 are available in Combescure et al. (1999), their envelope was digitized manually, with the original experimental results figures provided in Appendix A. The results are very promising because each experimental envelope sticks to the numerical pushover analysis.

A dynamic analysis was performed with CEA1 for all the tests, for test 1 to 5 (PGA of 0.2 $[g]$, 0.26 $[g]$, 0.63 $[g]$, 0.83 $[g]$ and 1 $[g]$) and with CEA3 for test 1 to 5 (PGA of 0.1 $[g]$, 0.25 $[g]$, 0.61 $[g]$, 0.82 $[g]$ and 1.05 $[g]$). For example, a PGA of 0.63 $[g]$ represent the ground motion developed in Figure 3.18b, that has been scaled in amplitude to obtain a PGA of 0.63$[g]$.

The comparison between the experimental envelope results and those obtained from the numerical simulation for CEA1 under tests 1, 3, and 4 are illustrated in Figures 3.20a, b, and c, respectively. The results for CEA3 under test 3 are presented in Figure 3.20d.

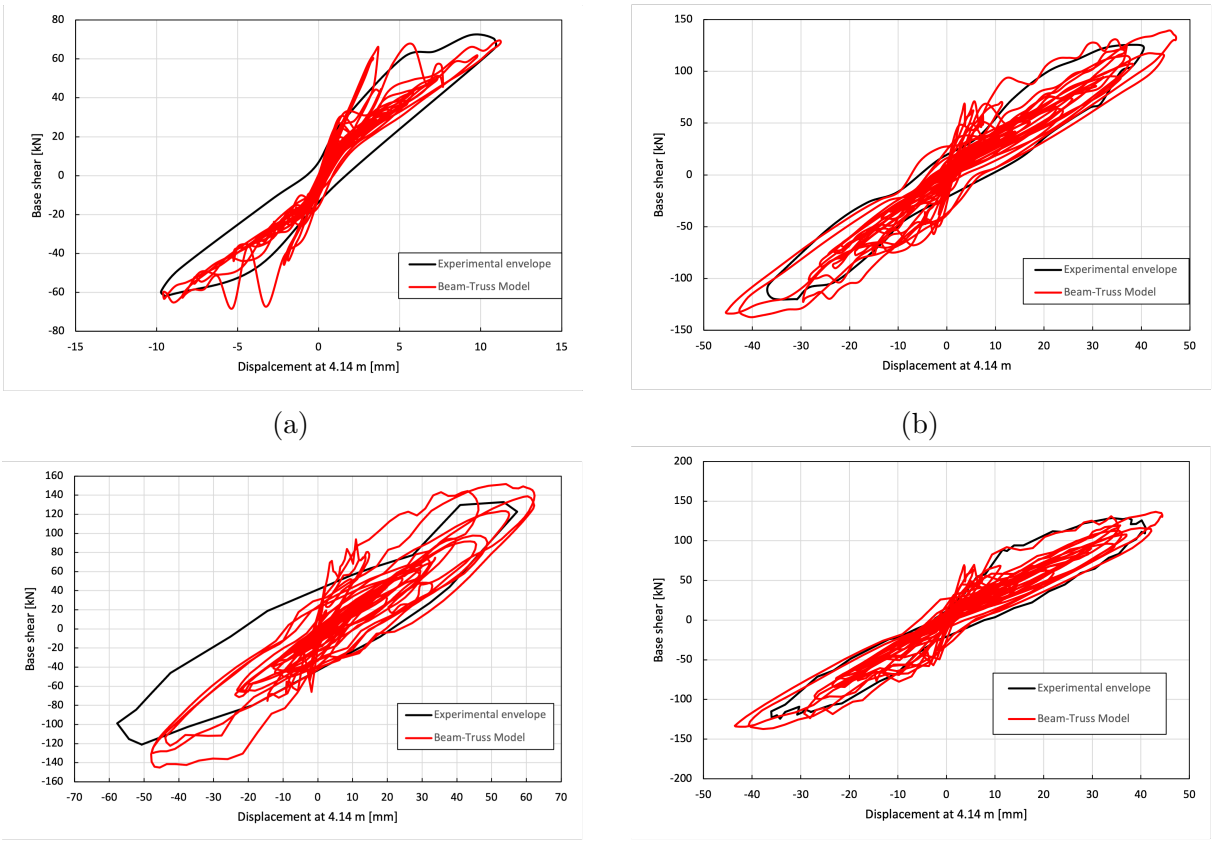
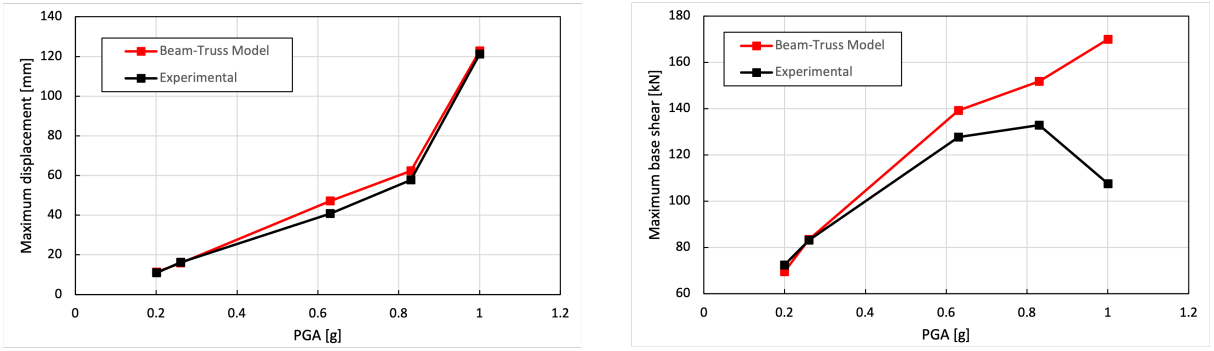


Figure 3.20: Experimental and simulate force-displacement relationship of CEA1 with test (a) 1, (b) 3, (c) 4 and (d) CEA3 with test 3.

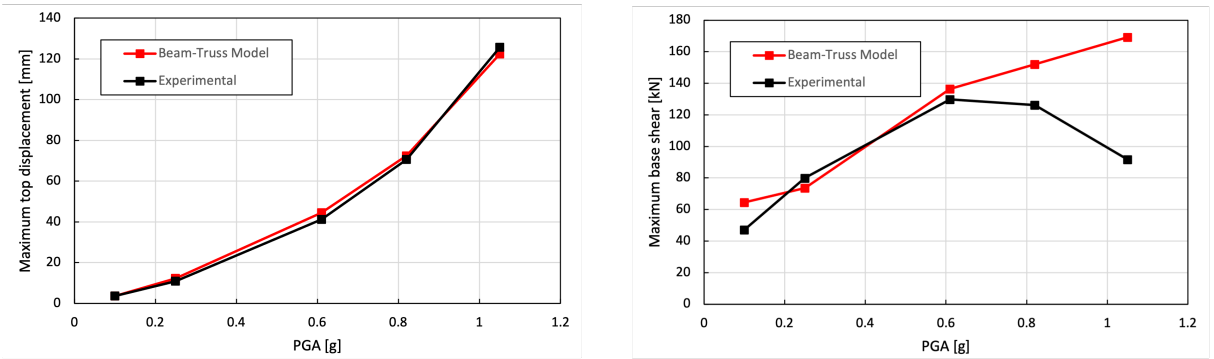
For all tests conducted from 1 to 5, the maximum displacement at 4.14 $[m]$ and the maximum base shear of CEA1 and CEA3 are summarized in Figure 3.21 and 3.22 to provide a concise overview of the overall behavior.



(a) (b)

Figure 3.21: (a) Maximum displacement at 4.14 $[m]$ and (b) maximum base shear for different PGA of CEA1.

The selection of the Rayleigh damping coefficient was motivated by achieving a good fit with the maximum displacement, which is why a favorable alignment between the modelled and experimental values is observed. Maximum base shear such as the stiffness exhibit accurate representation under small PGA. Despite small amount of available data and poor steel ductility, these tests were relatively well-modelled across various PGA levels. The main challenge lies in obtaining an appropriate value for the Rayleigh damping coefficient without experimental data.



(a) (b)

Figure 3.22: (a) Maximum displacement at 4.14 $[m]$ and (b) maximum base shear for different PGA of CEA3.

For UWS1 and UWS2, a damping coefficient value of 1% will be adopted, whereas for CEA1 and CEA3, the coefficients span from 1.5% to 5%. This lower value, on UWS units is assumed because the steel is way more ductile. An important step ahead would be to validate these assumptions and modelling choices against forthcoming experimental results.

This numerical analysis concludes the model validation procedure with a comprehensive dynamic modelling. UWS1 and UWS2 can be effectively modelled with a reasonable level of confidence, although certain aspects such as the SMA model, the impact of rigid elastic elements of the collar, and the value of the Rayleigh damping coefficient may require further refinement. The influence of these aspects will be interesting to analyze after the experimental campaign.

Chapter 4

BTM Analysis of ALL4wALL Units

In this chapter, UWS1 and UWS2 will be subjected to computational analysis under various static and dynamic loading conditions, thereby enabling a thorough comprehension of their structural response and analyse the influence of SMA. The impact of the upper masses' position will also be examined. Finally, the appropriate results for the blind prediction will be developed. Like in Chapter 3, geometrical nonlinearities will be ignored to avoid a misunderstood behavior on ultimate loading. All analysis of this section are only numerical, because the experimental campaign will take place after this thesis.

4.1 Units description and test set up

The central theme of this master thesis is the investigation of UWS1 and UWS2 units under a variety of loading scenarios. To be able to perfect the results, a good understating of the future experimental campaign is necessary. The blind prediction [27], i.e., an open competition to simulate the behavior of UWS1 led by the ALL4wALL team, from which this section is strongly inspired, will be updated as more information becomes available. The current data such as geometry, material properties and loading protocol will be presented in this section. An analysis using beam-truss modelling will be undertaken in the further sections.

4.1.1 Units description

4.1.1.1 Geometry of UWS1 and UWS2

The blind prediction competition [27] outlines the forthcoming design of UWS1. On the other hand, the details of the wall with Shape Memory Alloys (SMAs) at the base of the boundary regions, denoted as UWS2, are not included as the blind prediction if solely pertains to UWS1 (for the moment). Both units have identical wall configurations, the only difference is the SMA rebars. The quantity and placement of SMAs in UWS2 are

still to be finalized in the project, requiring certain assumptions that are presented below.

The UWS1 configuration draws inspiration from UW1, from Hoult et al. (2022) [5] representing a half-scaled core wall. Specifically, the geometric cross-sectional attributes remain unchanged. However, a difference exist in terms of hoop spacing, 50 [mm] for UWS1 compared to 75 [mm] for UW1, and the arrangement of transverse reinforcements, 100 [mm] for UWS1 compared to 150 [mm] for UW1. This deliberate adjustment aims to amplify the level of confinement within the boundary regions of the wall and respect the Eurocode 8 recommendations.

A three-dimensional view of UWS1 is illustrated in Figure 4.1 from the blind prediction document [27] and comprises a foundation, two intermediate slabs with an opening in the centre, and a top collar. The foundation and the collar of the wall are detailed with a high volume of reinforcement using 20 [mm] and 12 [mm] diameter bars, respectively, such that they effectively remain elastic during testing and provide a large stiffness. The size of the foundation is 2100 [mm] x 2100 [mm] x 500 [mm]. The top collar corresponds to an increased wall thickness at the upper extremity of the wall. Four stacks of masses are atop of the collar, they are described in Section 4.1.2 with the test setup

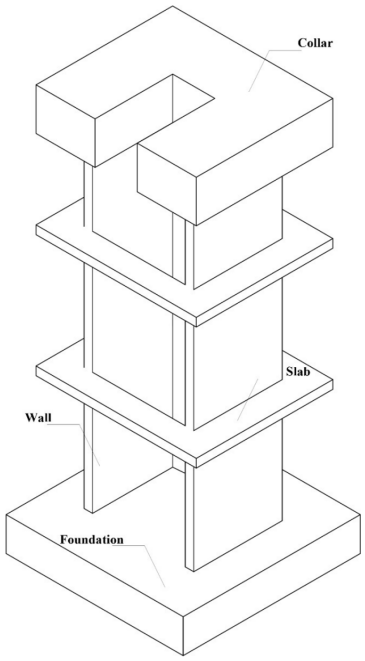


Figure 4.1: Three-dimensional elevation view of UWS1 from Blind Prediction - Test description.

The cross section is visually depicted in Figure 4.2. The length of the flanges is 1050 [mm] and the length of the web is 1300 [mm]. The wall is 100 [mm] thick and has a height of 4 [mm]. To ensure clarity, sectional views will feature a cardinal direction indicator, a compass, which serves to distinguish the flanges and elucidate the loading orientation. In the case of this wall, the compass direction is not aligned with that of the other walls. This divergence in orientation is determined by the setup of the shake table at the LNEC laboratory. The positive conventions are taken from North to South to and from West to East.

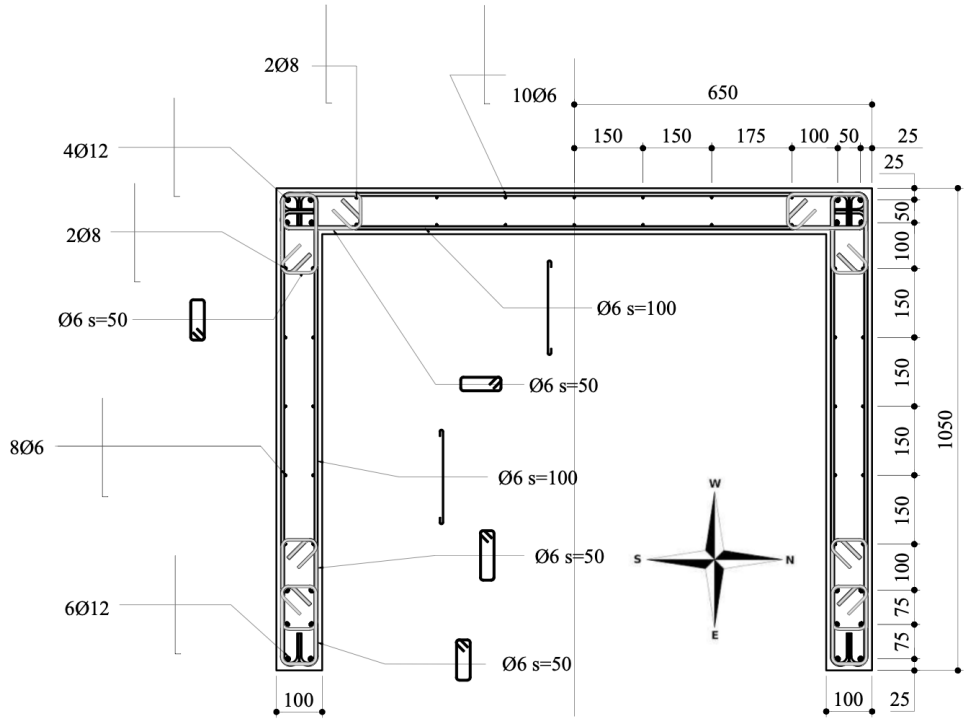


Figure 4.2: Cross section and reinforcement UWS1 and UWS2 [Unit: mm].

Figure 4.2 also illustrates the reinforcement bars. In each flange, there are eight longitudinal rebars with a diameter of 6 [mm] and two longitudinal rebars with a diameter of 8 [mm]. In the web, there are ten longitudinal rebars with a diameter of 6 [mm] and four longitudinal rebars with a diameter of 8 [mm]. At the two intersections between the web and the flanges, i.e, the corners, there are four longitudinal rebars with a diameter of 12 [mm]. Additionally, at each flange boundary, there are six longitudinal rebars with a diameter of 12 [mm].

Regarding the transverse reinforcement, each corner of the wall and flanges boundary

have two sets of hoops with a diameter of 6 $[mm]$. These hoops are spaced 50 $[mm]$ apart. Furthermore, there are two sets of 6 $[mm]$ rebars spaced 100 $[mm]$ apart that cross the full length of the web and flanges. These spaces of the hoops and the rebars are the only difference with UW1 besides the height.

Figure 4.3 represents the plan and elevation view of the beam-truss model for this wall. The section is divided into eleven elements and the height is divided into twelve portions of 320 $[mm]$ and one of 200 $[mm]$. 32 $[cm]$ of SMA was assumed at the bottom regions of the UWS2 unit and are represented in red on 4.3.

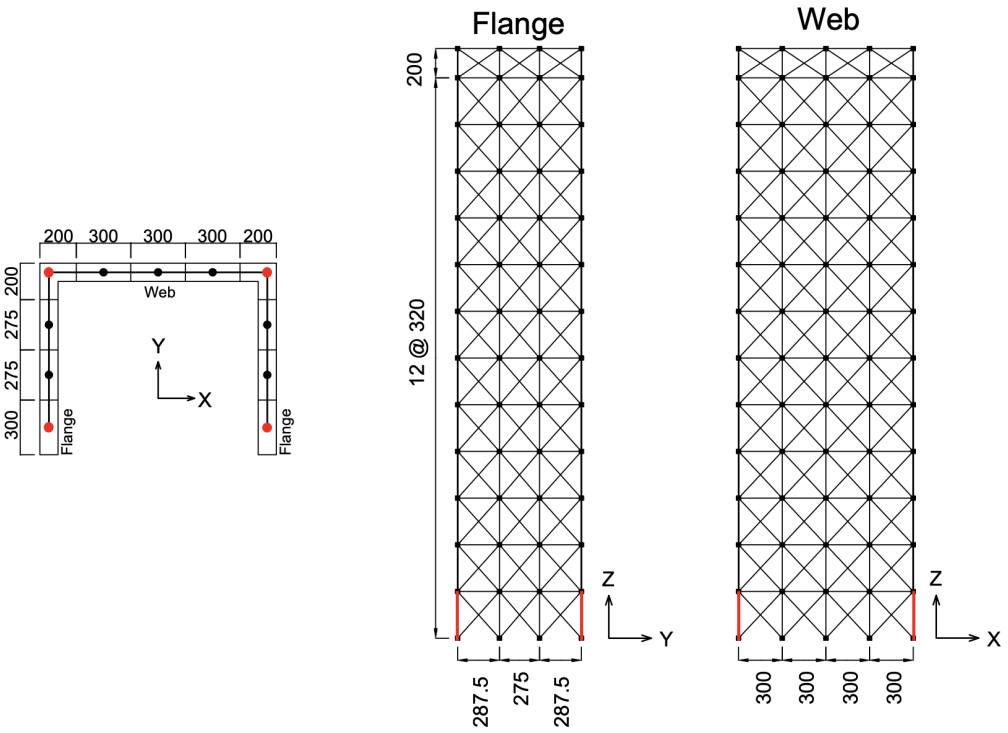


Figure 4.3: Plan and elevation views of the beam-truss model for UWS1 and UWS2 in red [Unit: mm].

Vertical and horizontal elements of the wall are modelled with inelastic displacement-based frame elements whereas the diagonal elements are modelled with nonlinear truss elements. The footing of the wall is not modelled. All elements of the collar and the link between each mass is modelled using elastic frame element with high rigidity, these links are just there to apply loads at the right position and do not influence the results. A three-dimensional visualization of the modelled walls in Seismostruct is illustrated in Appendix B.

4.1.1.2 Material properties

As of the time of this thesis, the experimental tests for these walls had not yet been conducted. Consequently, it becomes necessary to make certain assumptions concerning the actual material strengths. These values will be updated in the forthcoming blind prediction documents. The selected concrete grade for modelling these walls is C30/37, while the steel will mirror that of the UW1 unit, maintaining consistency with the same supplier. The SMA rebars for UWS2 will be assumed with the identical strength than the SMA+RC wall from Almeida et al. (2020) [11]. These parameters employed in the beam-truss model are specified in Table 4.1 for the concrete, Table 4.2 for the rebar steel properties and Table 4.3 for the SMA.

On Seismostruct, only one material can be chosen for the longitudinal reinforcement of one section so all the rebars in the element with SMA will be SMA rather than only the 12 $[mm]$ rebars.

Table 4.1: UWS1 and UWS2 concrete mechanical properties.

Properties	f_c	f_t	E	ϵ	γ
Unit	MPa	MPa	GPa	%	kN/m^3
Value	36	2.9	2.57	0.2	24

Where f_c is the concrete compressive cylinder strength at the day of testing, f_t is the tensile concrete strength, E_c is the concrete elastic modulus, ϵ_c is the strain at peak stress and γ is the specific weight.

Table 4.2: UWS1 and UWS2 steel mechanical properties.

Properties	d	f_y	f_u	E_s	ϵ_y	ϵ_u	α	γ
Unit	mm	MPa	MPa	GPa	%	%	%	kN/m^3
Value	6	550	676	207	0.27	9.5	0.66	78
	8	550	676	207	0.27	9.5	0.66	78
	12	580	690	199	0.29	10.1	0.56	78

Where d is rebar diameter, f_y is the yield tensile strength, f_u is the ultimate strength, E_s is the Young's modulus, ϵ_y is the yield strain, ϵ_u is the ultimate strain, α is the strain hardening parameter (see Formula 2.2) and γ is the specific weight.

Table 4.3: UWS2 shape memory alloy mechanical properties.

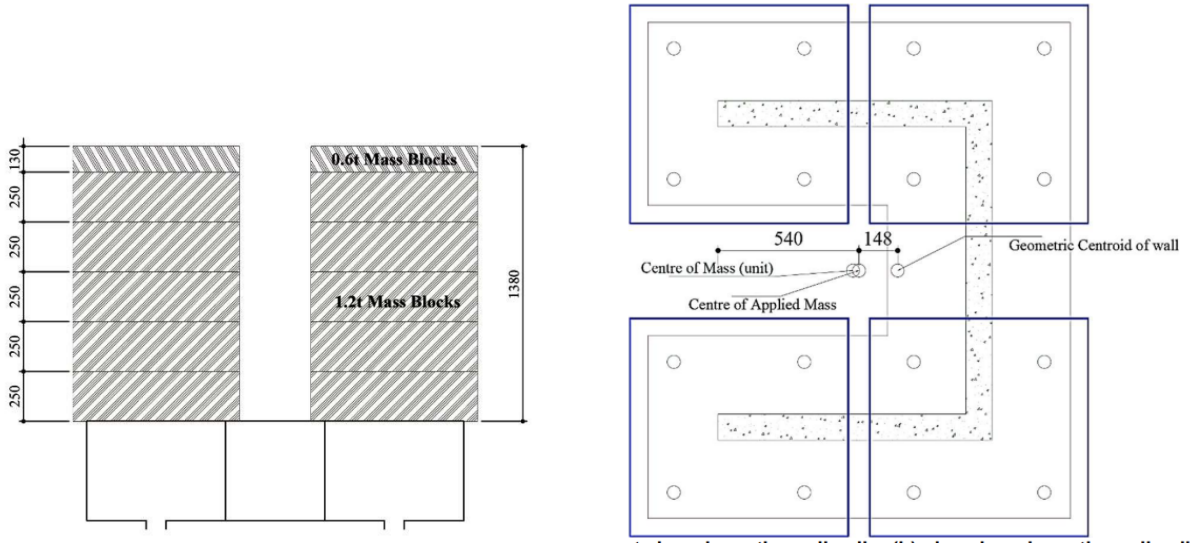
Properties	d	E	σ_{AMs}	σ_{AMf}	σ_{MAs}	σ_{MAf}	γ
Unit	mm	GPa	MPa	MPa	MPa	MPa	kN/m^3
Value	12.7	31	319	349	73	32	65

Where d is rebar diameter, E is the modulus of elasticity, σ_{AMs} is the austenite to martensite start stress, σ_{AMf} is the austenite to martensite finish stress, σ_{MAs} is the martensite to austenite start stress, σ_{MAf} is the martensite to austenite finish stress, and γ is the specific weight.

4.1.2 Test setup and limitation of the table

The wall units will be tested on the large shake table at LNEC. The maximum horizontal capacity of the table's actuators in the East-West (EW) and North-South (NS) directions are 700 [kN] and 500 [kN], respectively. The orientation of the wall with respect to these cardinal directions is shown in Figure 4.2. The maximum displacement and velocity of the table in either direction is ± 200 [mm] and ± 600 [mm/s], respectively. The maximum payload of the shake table is approximately 40 [ton].

Four stacks of masses of 1.13 [ton] and 0.59 [ton], depicted in Figure 4.4 are connected to the collar. Each mass block is 840 [mm] x 840 [mm] in cross section and 250 [mm] or 130 [mm] thick for 1.19 [ton] or 0.59 [ton]. A total of 20 (4x5) 1.13 [ton] mass blocks and four (4x1) 0.59 [ton] mass blocks are placed atop. The combined weight of the four sets of masses is 24.96 [ton], and the weight of the collar is 3.27 [ton], totaling 28.23 [ton] in axial loads. The wall itself weighs approximately 3.23 [ton] without accounting for the intermediate slab. Taking into consideration the non-modelled foundation, the total mass of the specimen is 40 [ton].



(a) (b)

Figure 4.4: (a) Elevation view and (b) plan view of the top of the wall of UWS1 and UWS2 from Blind Prediction - Test description [unit: mm].

The position of the centre of mass, which corresponds to the centre of mass of the U-shaped wall unit above the foundation, and the position of the centre of applied mass, which corresponds to the centre of mass of the 24 mass blocks applied above the collar are depicted in Figure 4.4b. The center of the applied mass is estimated to be around 540 $[mm]$ from the ends of the flange boundary, while the center of mass of the wall unit is calculated to be approximately 516 $[mm]$. An numerical analysis about the influence of the distance between the center of mass and the center of applied mass will conducted in Section 4.6.

The recent updates of the geometry of the masses have led to the modelling of the wall with 1.2 $[ton]$ and 0.6 $[ton]$ masses instead of 1.13 and 0.59. Additionally, the thickness corresponding to the heavier masses has been modelled as 260 $[mm]$ instead of 250 $[mm]$. These modifications exert a negligible influence on the outcomes, with deviations of less than half a percent observed in extreme values during cyclic loading scenarios. In the event of further work being undertaken with this model, it is recommended to reevaluate both the model parameters and the material properties regarding the actual description in the blind prediction [27].

4.1.3 Instrumentation

In order to facilitate a comparison between the experimental behavior of the specimen during quasi-static or dynamic tests and the numerical simulation, an extensive amount of different instrumentation is employed. Measurements of displacement, acceleration, strength, and the overall behavior of the wall are essential. In the context of the ERIES - ALL4wALL project, the following main instrumentation, Discussed in the blind prediction [27] will be employed:

- Potentiometers or **string pots** (SP) are sensors to measure displacement. Two of them will measure the East-West displacement at the end of each flange of the collar at the height of 4.29 $[m]$ from the foundation. They will also be used to measure torsional rotation of the wall with a lever arm of 1.2 $[m]$. Another potentiometer will be used to measure the East-West displacement of the table, such that the relative measurement of the wall can be calculated.

- An **accelerometer** used to measure the acceleration, along both horizontal directions will be placed at 4.29 $[m]$ from the foundation in the center of the collar. This acceleration will be used to calculate the approximate, in-plane, East-West lateral inertial force using the applied mass of 28.23 $[ton]$.

- **Distributed fibre-optic sensors**, (DFOS) will be used to accurately determine the strains of some of the reinforcing bars. This involves creating a small groove, 1 $[mm]$ wide and deep, along the longitudinal ribs of the rebar and inserting an optical distributed sensor into it. The sensor is securely bonded to the fiber using a general-purpose adhesive. This method was successfully used during the UW1 and UW2 experimental campaign like developed in Hoult et al. (2022) [5], this document contains more information about DFOS, their component and results. The use of DFOS is really precise and help understanding the behavior in the rebars and compare it with numerical analysis.

These sensors are not the only ones in use, but they hold a primary role. Their collected data will serve to compare the numerical prediction against the experimental results during the blind prediction phase.

4.1.4 Loading protocol

The ERIES - ALL4wALL team is currently still in the process of selecting the appropriate ground motions (GMs) to use for the dynamic tests. At the time of writing, the likely ground motion that will be used is described in this section and will be employed for the numerical simulation.

An important earthquake with a moment magnitude of M_w 6.5 happened the October 30, 2016, in the center of Italy. Its ground motion will be the base of the input of the dynamic analysis. The data comes from the seismometer station MZ04, located at 23 $[km]$ of the epicenter. The East-West measurement direction is denoted HNE and the North-South measurement direction is denoted HNN. These ground motions will be applied at LNEC respectively in the North-South and the East-West directions of the wall, e.g., the HNN ground motion will act on the weak axis of UWS1, in the East-West direction Refer to the previous Figure 4.2 for a visualization of the cross section with the corresponding directions.

The primary segments of HNN and HNE ground motions were selected and temporally scaled using a factor of $\sqrt{0.5}$, as a recall, the global scaling factor is 0.5. This adjustment led to a change in the time step from 0.005 $[s]$ to 0.003535 $[s]$, in accordance with the similitude law as outlined in Pinho (2000) [25]. The ground motions HNN and HNE are illustrated in Figure 4.5 and Figure 4.6, respectively. The peak ground acceleration (PGA) for these two directions is approximately 0.808 $[g]$ and 0.645 $[g]$.

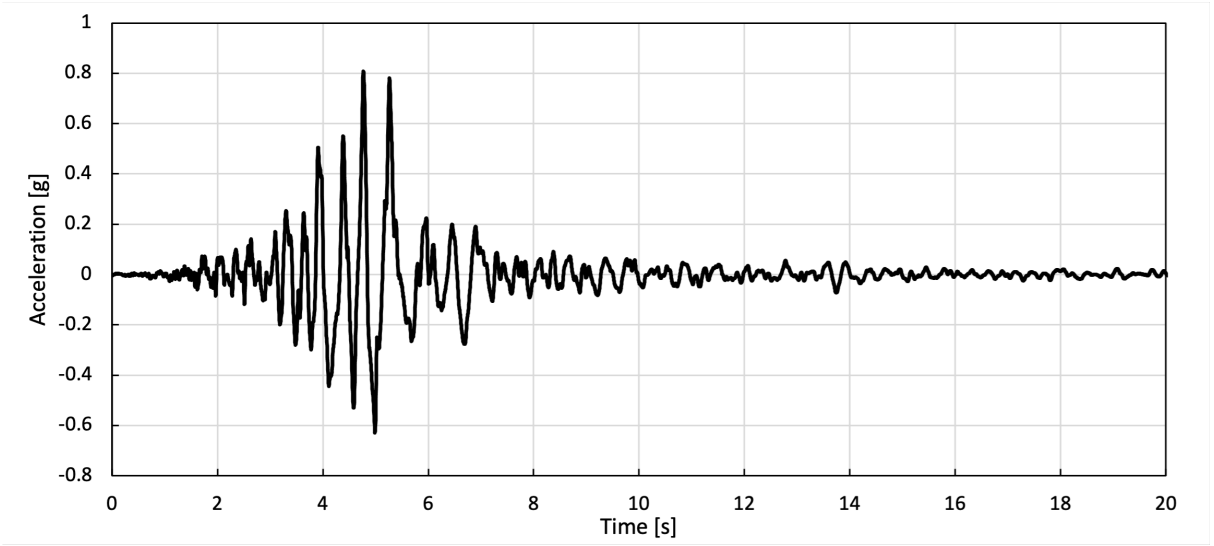


Figure 4.5: Time-acceleration of the HNN ground motion.

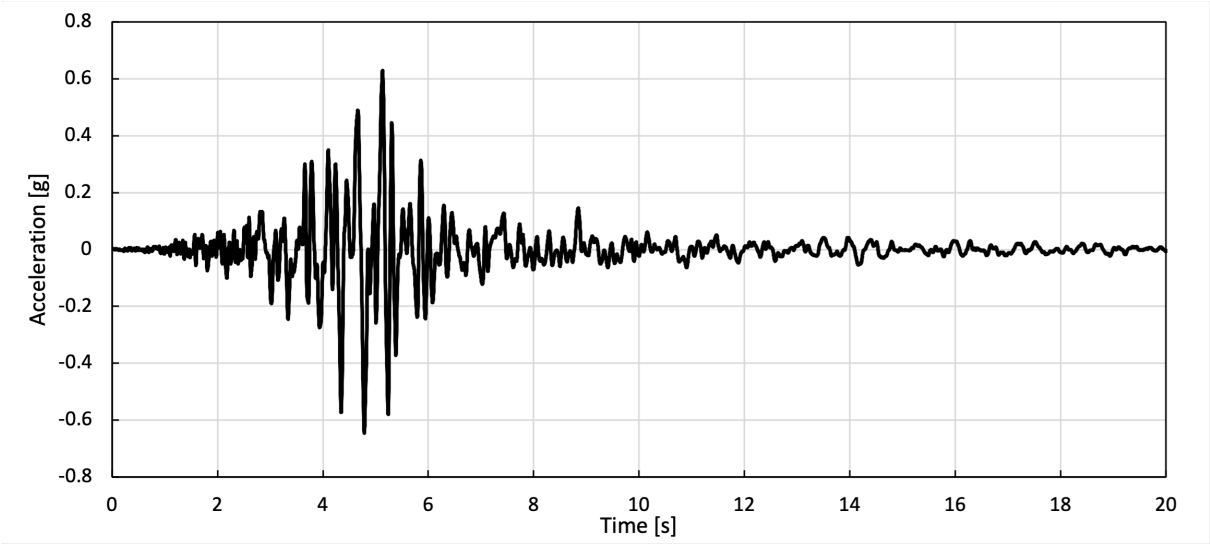


Figure 4.6: Time-acceleration of the HNE ground motion.

This ground motion was selected by Dr. R. Hoult to match the effective period of the wall, ensuring that the unit responds to the ground motion excitation. Additionally, this specific ground motion was chosen due to its relevance as a recent European seismic event.

The proposed dynamic tests of units UWS1 and UWS2 will comprise nine different levels of ground motions (GM0 to GM8). Each ground motion level corresponds to a different scale combination of the HNE and HNN of the Mw 6.5 event recorded on October 30, 2016 by MZ04 seismometer. The HNN ground motions will be used in the East-West shake table direction, and the HNE will be used in the North-South direction. The positive direction of the ground motion corresponds to the positive direction of the shake table as defined above, i.e., from North to South and from West to East.

GM0, the test run, corresponding to only 10% of the EW ground motion will be firstly conducted. Afterwards, odd GMs are only EW ground motions and even GMs will apply acceleration in both directions to induce torsion in the wall. Table 4.4 describes the different GMs stages, while Figure 4.7 and Figure 4.8 illustrate them, respectively in the EW and NS direction, with a 10 $[s]$ gap between each motion to allow the wall to return to its initial position during the numerical modelling. These are the final inputs to proceed to the dynamic analysis in Seismostruct. Note that GM0 is not included in the figures.

Table 4.4: Ground motion scaling factor from blind prediction.

	Scale [%] of HNN	Scale [%] of HNE
GM0	10	0
GM1	25	0
GM2	25	25
GM3	50	0
GM4	50	50
GM5	75	0
GM6	75	75
GM7	100	0
GM8	100	100

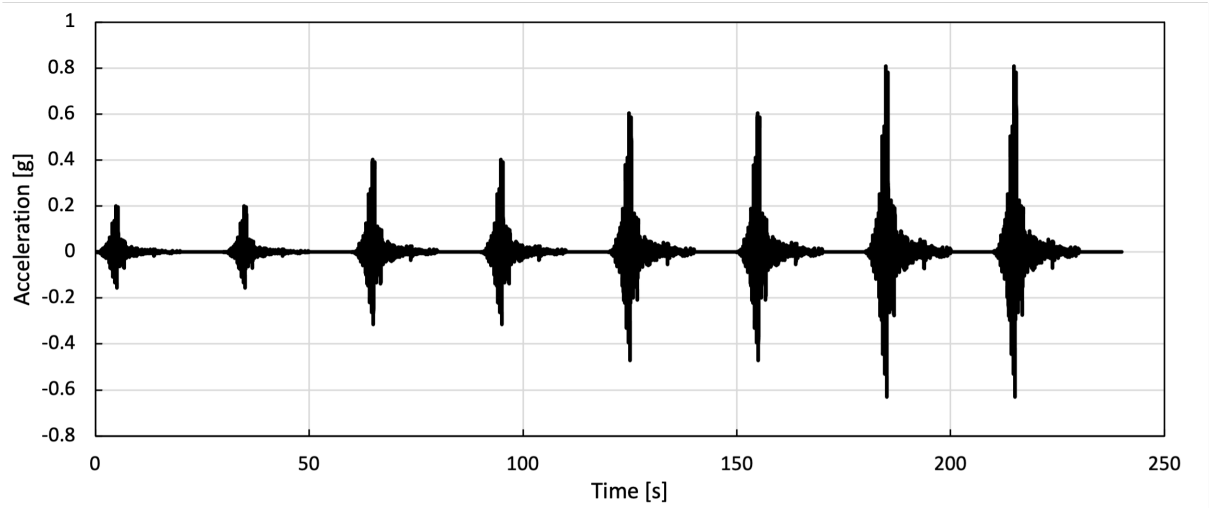


Figure 4.7: Total dynamic loading in the EW direction (HNN).

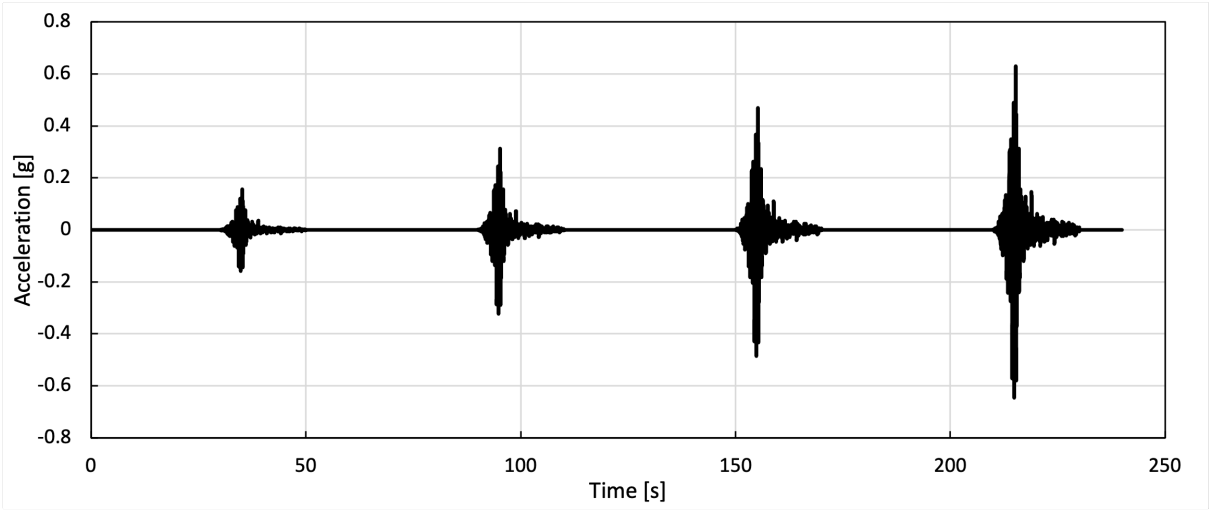


Figure 4.8: Total dynamic loading in the NS direction (HNE).

The objective of employing this loading protocol is to study the torsional effects resulting from dynamic loading in two directions. The approach involves progressively analyzing the residual displacements that arise due to these accelerations.

4.2 Numerical static analysis

Static tests will not be performed during the All4wAll experimental tests, however, these are interesting to have a comprehensive understanding of structural response of the unit.

The numerical simulations were executed until the end of the compilation, but it may not accurately represent the failure modes, performance criteria are employed with specific values developed in Section 2.4.2. As indicated in Chapter 3, the geometrical nonlinearities will be ignored due to the modelling of a misunderstood increasing of strength during large displacements.

Linear pushover analysis will be conducted in each direction before cyclic and torsional loading. These tests provide significant values that can be leveraged to assess the wall's dynamic loading capacity and to facilitate a comparison with UWS2, which incorporates SMA rebars.

4.2.1 Static pushover

4.2.1.1 UWS1

Static displacement incremental pushover analyses of UWS1 are depicted in Figure 4.9 and Figure 4.10 for the EW loading direction, while Figure 4.11 corresponds to the NS loading direction. The displacements are imposed and measured at a height of 4.29 $[m]$, i.e., the middle of the collar.

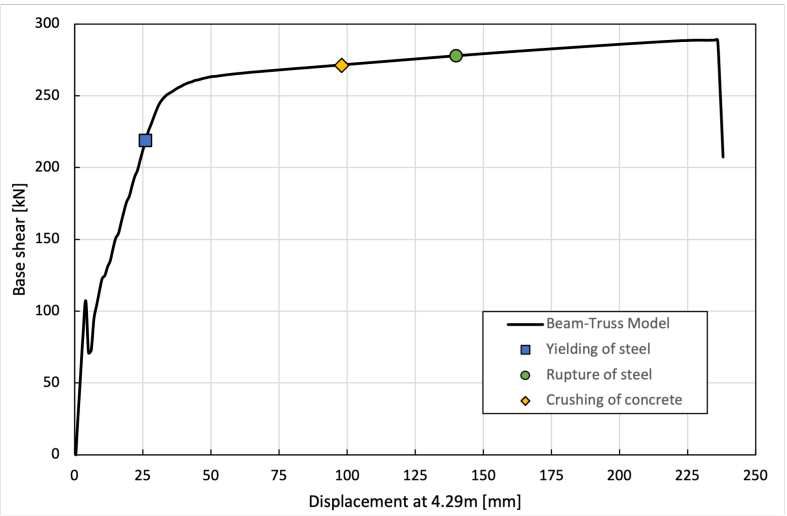


Figure 4.9: Force-displacement relationship of UWS1, West-to-East pushover.

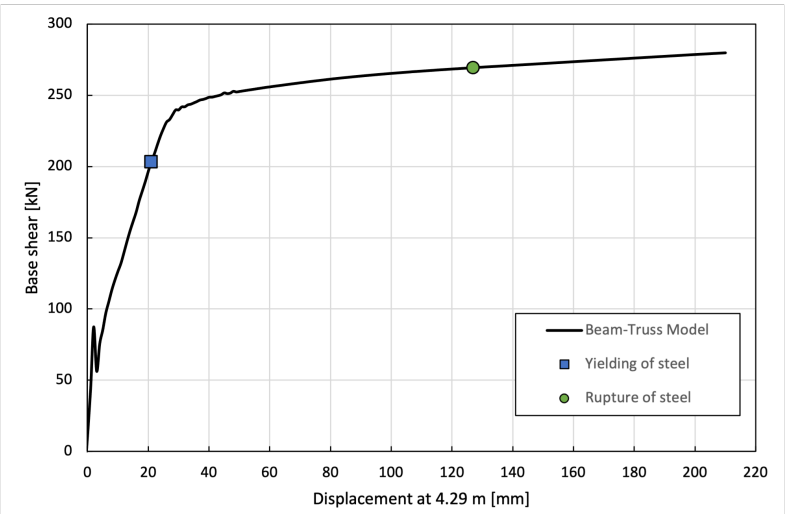


Figure 4.10: Force-displacement relationship of UWS1, East-to-West pushover.

Due to position of the masses, not exactly at the center of mass of the wall, as expounded upon in Section 4.1.1.1, a slight variance becomes apparent between the two directions of applied force. The application of performance criteria helps illuminate the overall behavior of the wall: when subjected to an Eastward force, the wall experiences predominantly compression, whereas pushing it in the Westward direction induces tension.

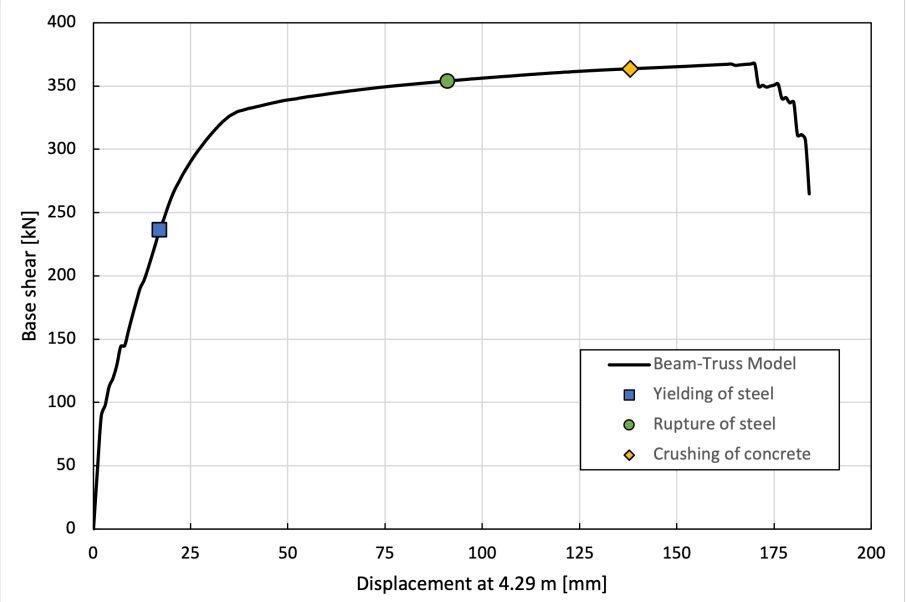


Figure 4.11: Force-displacement relationship of UWS1, North-South pushover.

The inherent symmetry of the wall engenders equivalent outcomes in both direction (North-to-South and South-to-North). Notably, this particular loading direction exhibits greater structural strength compared to the EW direction, thereby warranting its characterization as the "major/strong axis".

4.2.1.2 UWS2

Static displacement incremental pushover analyses of UWS2 are depicted in Figure 4.12 and 4.13 for the East-West loading direction, while Figure 4.14 corresponds to the North-South loading direction. The displacements are imposed and measured at a height of 4.29 $[m]$, i.e., the middle of the collar.

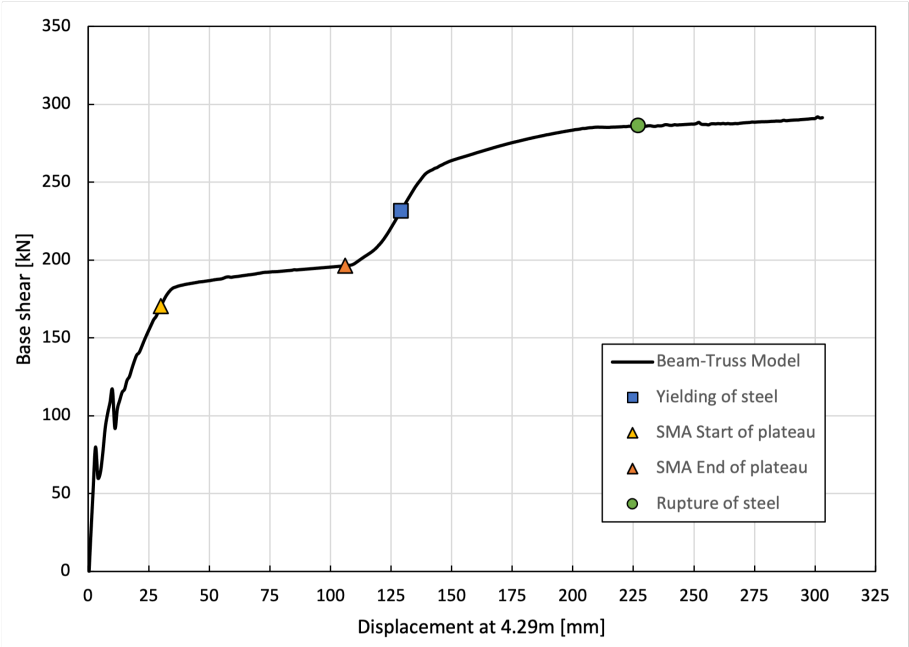


Figure 4.12: Force-displacement relationship of UWS2, West-to-East pushover.

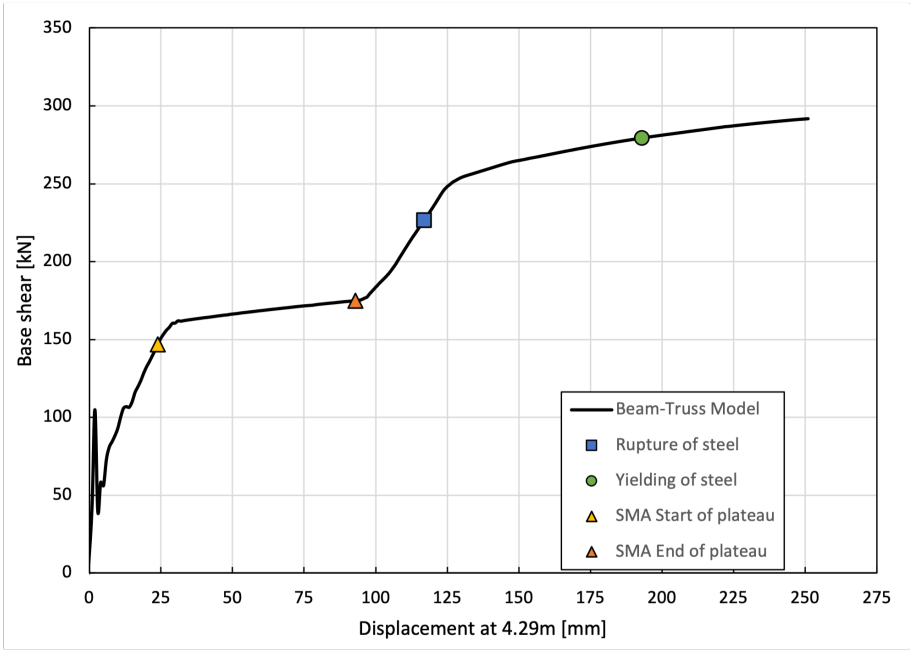


Figure 4.13: Force-displacement relationship of UWS2, East-to-West pushover.

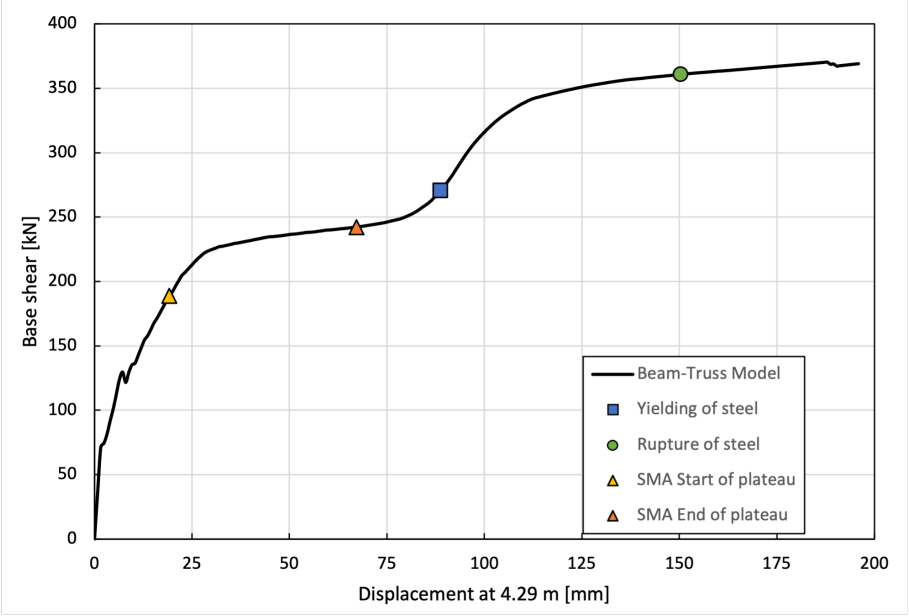


Figure 4.14: Force-displacement relationship of UWS2, South-North pushover.

The specific shape of SMA pushover can be observed with a second plateau after the performance criteria "SMA End of plateau". Comparison between UWS1 and UWS2 will be conducted in the next section with cyclic loading.

4.2.2 Torsional analysis

The response of UWS1 to torsional loading is depicted in Figure 4.15. The results exhibit symmetry in both directions so only one rotation sens is represented. The rotation in $[mrad]$ and the torque in $[kNm]$ are obtained with the exact same method than UW2 in Section 3.1.4. The formula for the rotation is:

$$\theta = \frac{\delta_1 - \delta_2}{1.2} \tag{4.1}$$

where δ_1 and δ_2, in $[mm]$ correspond to the displacement of the West and East flange at 4.29 $[m]$, and the 1.2 on the denominator is the lever arm distance (in $[m]$) between the two flanges (centre-to-centre); the resulting θ is in milliradian, $[mrad]$.

The torque (T, in $[kNm]$) was calculated using Equation 4.2.

$$T = \frac{F_W - F_E}{2} \times 1.2 \tag{4.2}$$

where F_W and F_E are the forces, in $[kN]$, measured by the actuators from the flange to the West and East separated by a 1.2 $[m]$ lever arm in the model.

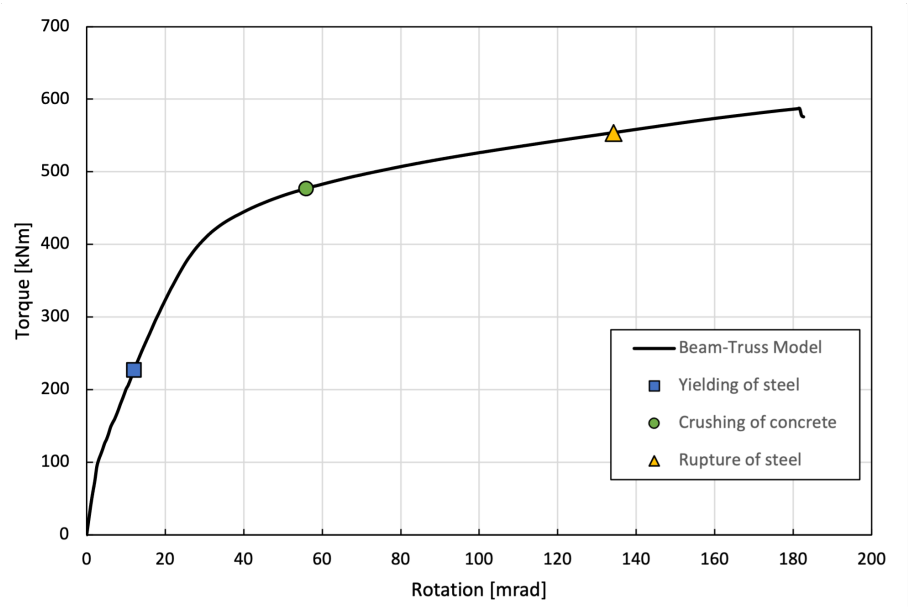


Figure 4.15: Rotation-torque relationship of UWS1, torsional loading.

The observed response closely aligns with that of UW2 in Section 3.1.4. The increased reinforcement refinement in UWS1 has led to enhanced strength, and due to the application of torsion at a higher location compared to UW2, a greater rotational capacity can be accommodated.

Interestingly, unlike the UW2 unit, the stiffness of the links modelled with elastic frame elements, which are employed to represent the collar and the connections between masses, did not appear to influence the resisting torque of the wall. It might be worthwhile to conduct further investigation into the calibration of torsion using beam-truss modelling and the use of rigid elements for the collar.

The response of UWS2 to torsional loading is depicted in Figure 4.16.

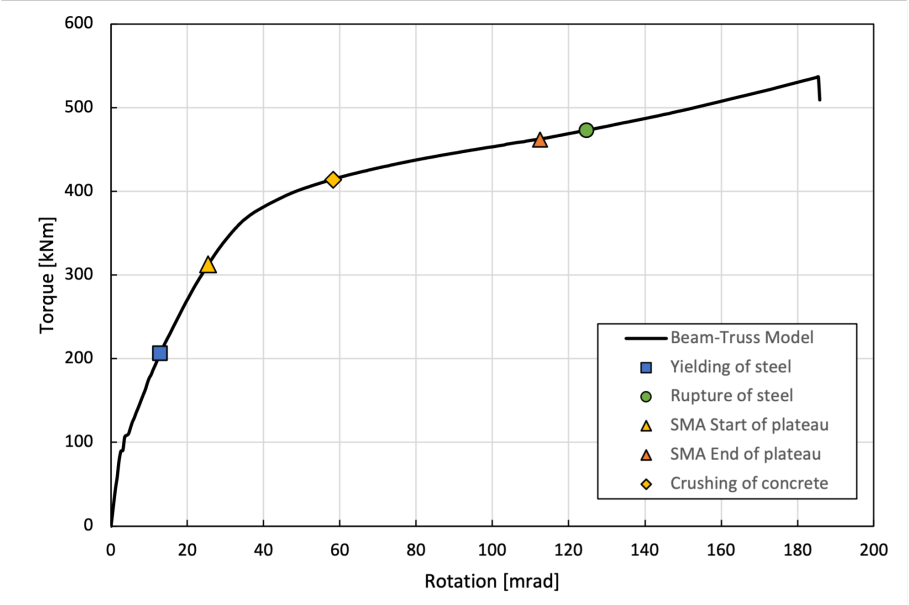


Figure 4.16: Rotation-torque relationship of UWS2, torsional loading.

Unlike bending, where forces are concentrated at the bottom of the wall, torsion distributes shear forces throughout the entire wall. As a result, the influence of the SMA, only located at the bottom of the wall, is not pronounced in torsional behavior.

4.2.3 Cyclic loading

One of the final objective of the All4wAll project is to observe the influence of the SMA at the bottom boundary of the wall under dynamic loading. The final design of the unit is not completed at the time of writing this thesis, so the size of SMA rebars is assumed of 32 cm, i.e., the high of a vertical element of the beam-truss modelling.

Static displacement incremental cyclic analysis of UWS1 and UWS2 are presented in Figure 4.17 in East-West loading directions. The convention of positive displacement corresponds to pushing toward the East direction. The displacements are imposed and measured at a height of 4.29 $[m]$, i.e., the middle of the collar. Figure 4.18 describe the residual drift after the different loading cycles. The drift is the ratio between the top displacement and the height of the wall, e.g., a displacement of 100 $[mm]$ at the center of the collar, at 4.29$[m]$ corresponds to $\frac{100}{4290} = 2.34\%$.

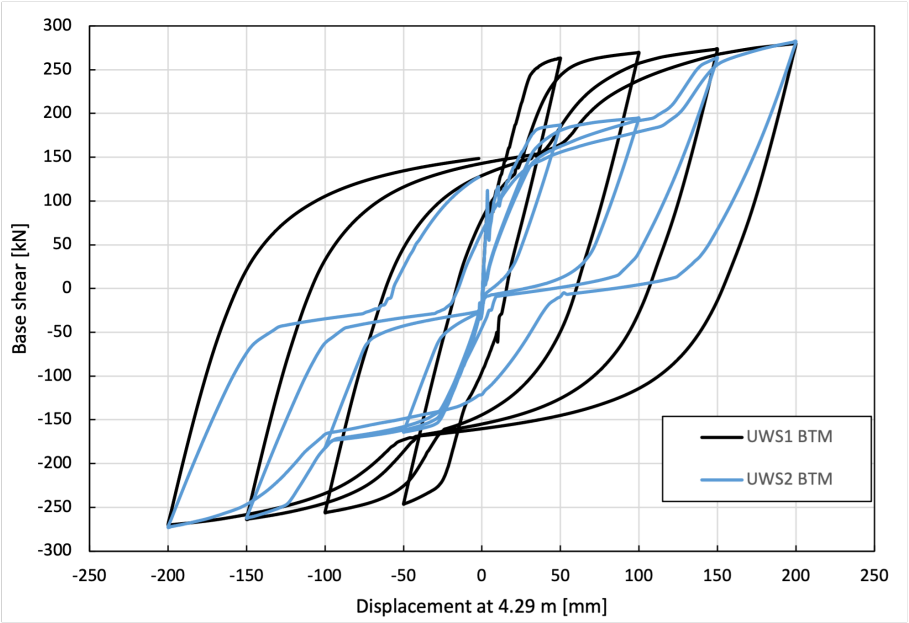


Figure 4.17: Force-displacement relationship of UWS1 and UWS2, EW cyclic loading.

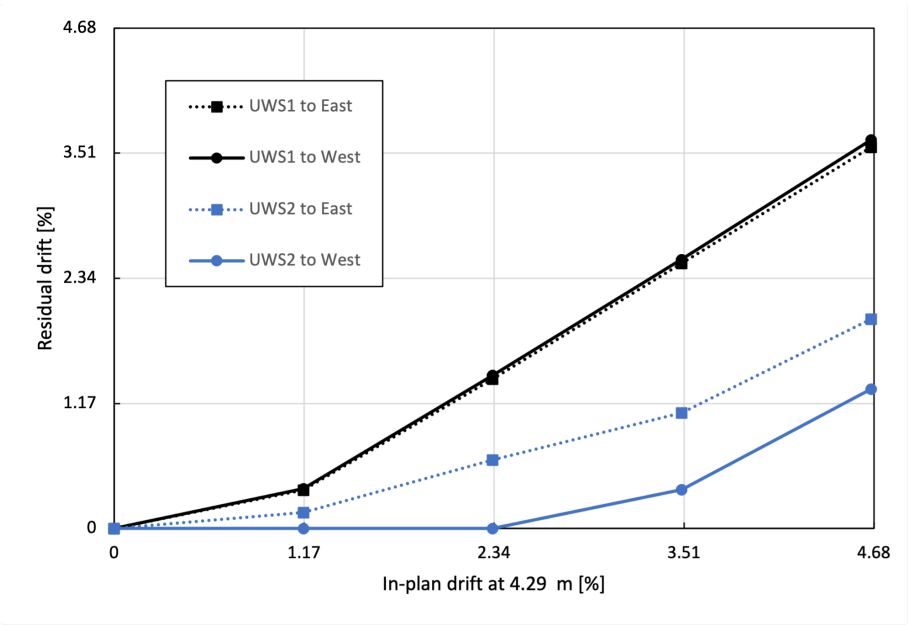


Figure 4.18: Residual drift regarding in-plan drift at 4.29 [m].

Static displacement incremental cyclic analysis of UWS1 and UWS2 are presented in Figure 4.19 in EW loading directions. The convention of positive displacement corresponds

to pushing toward the South direction. The displacements are imposed and measured at a height of 4.29 $[m]$, i.e., the middle of the collar. Figure 4.20 describe the residual drift after the different loading cycles.

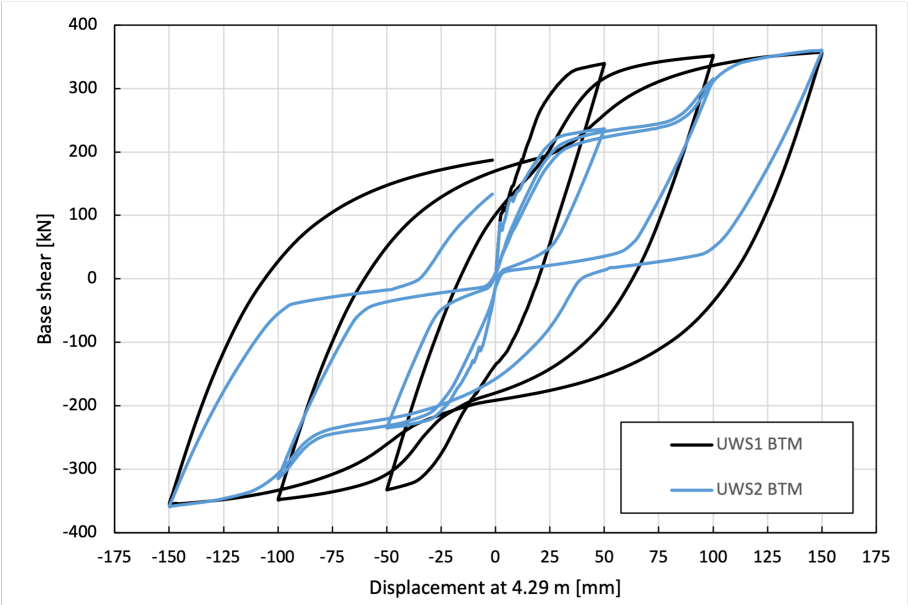


Figure 4.19: Force-displacement response of UWS1 and UWS2, NS cyclic loading.

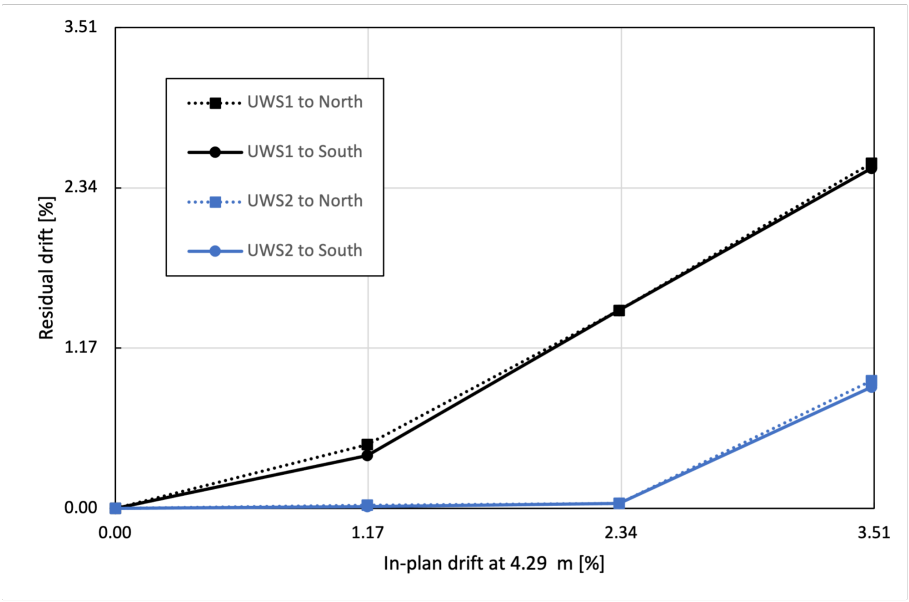


Figure 4.20: Residual drift regarding in-plan drift at 4.29 [m].

During quasi-static loading, SMAs exhibit a notable impact in diminishing residual displacement, while their influence on final maximum displacement and base shear is minimal. However, as discussed in Section 3.3 and evidenced by the RC+SMA unit, the reliability of the SMA model in predicting residual displacement is limited. The outcomes of this analysis hold significant value for future comparisons with upcoming experimental tests.

4.3 Nonlinear static analysis

Before going threw dynamic loading, a nonlinear static analysis, the N2 method proposed by Fajfar (2000) [28] was conducted. It has been described during the course "Earthquake Engineering" given by Prof. Almeida [29] and "Nonlinear response analysis" given by Dr. António Correia and Prof. Almeida [30]. A key departure from the course's methodology lies in the fact that this analysis is not aimed at designing the wall, as the design aspect is already established. The objective is to use a Eurocode 8 [3] method, the N2 method, to estimate the maximum displacement of the wall under cyclic loading.

4.3.1 Bilinearization

The first step of the procedure entails to bilinearize a static pushover analysis, loading the unit at the center of gravity, unlike previous tests where the horizontal loading was applied on the collar. The yield point of the steel is employed to define the effective stiffness, i.e., the slope of the elastic section of the graph, while the plateau is determined through the principle of equivalent energy, ensuring that each curve encompasses an identical area beneath it. In the future version of the Eurocode 8, an alternative method can be utilized to bilinearize the curve but it will not be employed in this study. This curve represents the capacity of the wall and is denoted as the capacity curve.

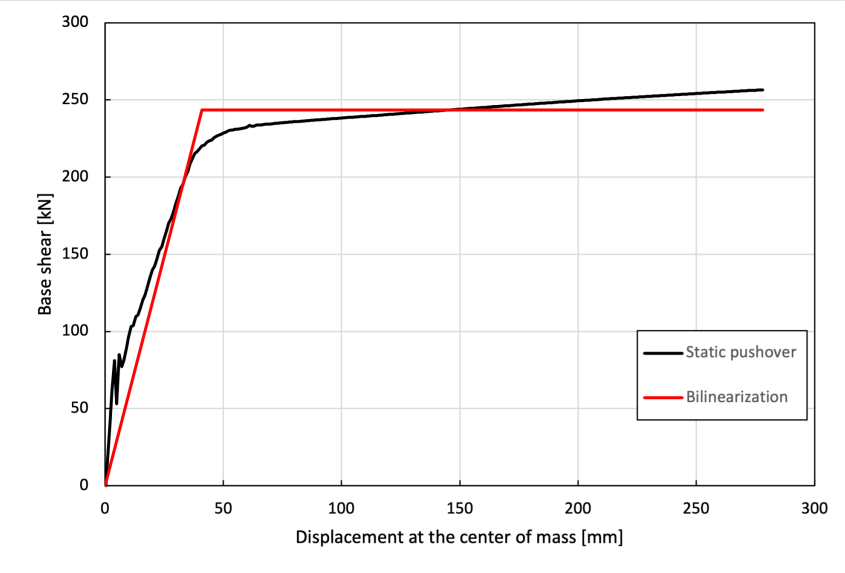


Figure 4.21: Bilinear representation of a static pushover analysis.

After constructing the capacity curve, the seismic demand represented with a design spectra has to be selected employing the methodology outlined in Eurocode 8. The decision was made to opt for an elastic design spectrum with 5% damping, characterized by a type 1 A ground type and an importance class of II. Utilizing a Peak Ground Acceleration (PGA) value of 0.8 $[g]$, coherent with the selected ground motion (GM) for the All4wAll project, Figure 4.22 visually portrays the design elastic spectrum and the GM of the project. Another criterion for the spectra was to have its peak of excitation near 0.46 $[s]$, the effective period of the wall. The effective period can be obtained with the formula 4.3.

$$T_{eff} = 2\pi\sqrt{\frac{m}{k_{eff}}} \tag{4.3}$$

where m is the mass of the wall, 31.46 $[ton]$ and k_{eff} is the effective stiffness.

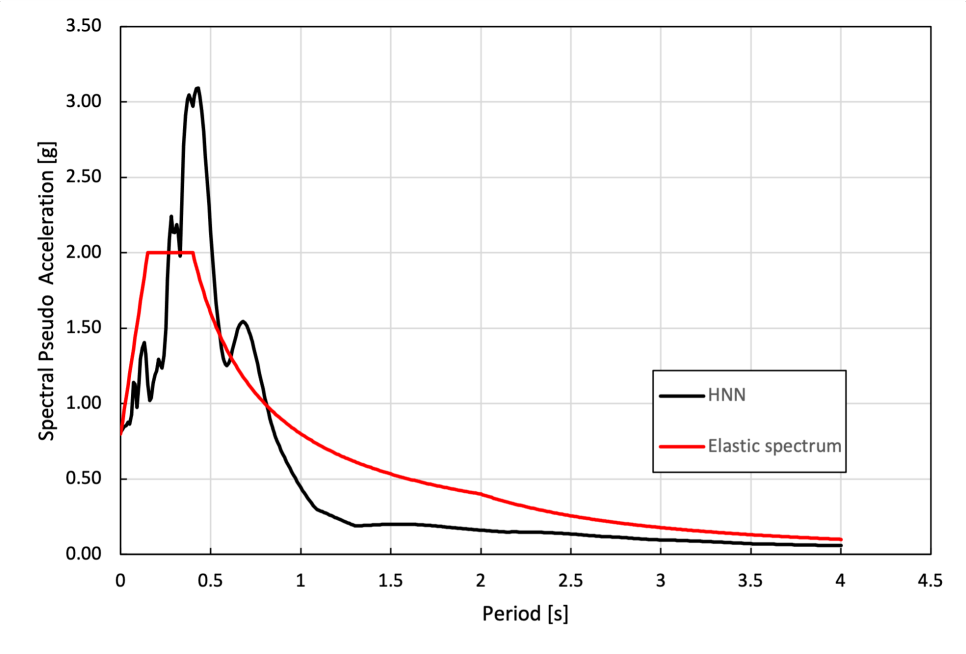


Figure 4.22: Elastic spectra of HNN and design elastic spectra from Eurocode 8.

4.3.2 N2 method and performance point

A non-linear procedure allows to confront the demand for deformation caused by the seismic event represented by a response spectrum and the capacity of the structure, represented by the capacity curve defined above to find an intersection representing the performance point, that is the presumed deformation state of the structure.

The non-linear procedure recommended in Eurocode 8 is the N2 procedure developed by Fajfar in 2000 [28]. The aim is to determine the performance point of the structure for a given seismic action, i.e. to determine the maximum relative displacement caused by a seismic excitation, as close as possible to reality.

The target displacement, or operating point of the structure, is evaluated by comparing the seismic demand and its capacity curve as described previously. A common way of representing these curves is in the Acceleration Displacement Response Spectrum (ADRS) format, with displacements on the abscissa and accelerations on the ordinate. Since pseudo acceleration and displacement are linked by a fundamental relationship depending on the frequency of vibration ω: $S_{pa} = \omega^2 \times S_d$.

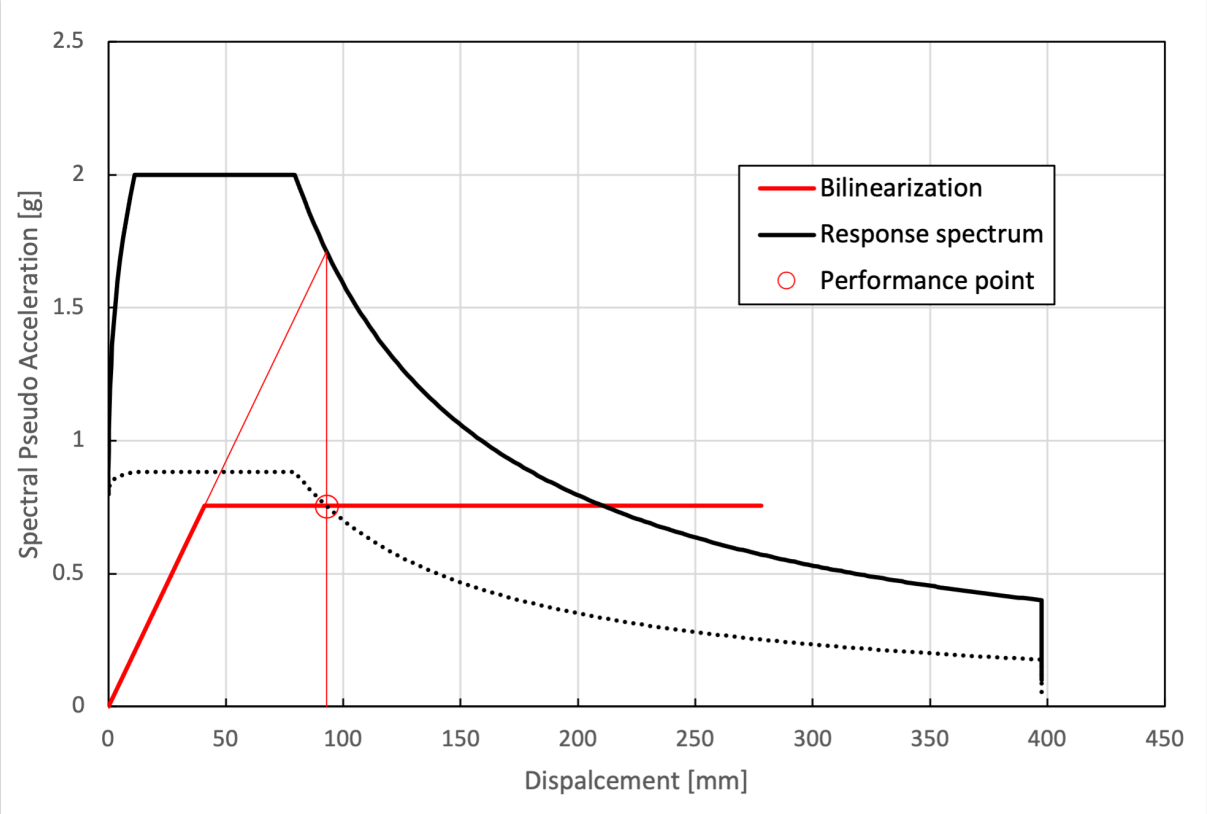


Figure 4.23: Performance Point Determination with the N2 Method.

In practical terms, designing for purely elastic behavior under strong seismic forces would lead to oversizing and increased costs. The preferred approach allows controlled plastic deformation, using a behavior factor to reduce elastic design forces. This ensures structural ductility and load-bearing capacity while managing damage within acceptable limits. Additional details about this methodology and its literature review can be found in the Earthquake Engineering course [29].

The expected inelastic demand at the performance point is 93 $[mm]$ with a ductility demand of 2.27. This value is close to the further results of numerical dynamic analyses without cumulative GM: 89 $[mm]$. This value was computed with a unidirectional dynamic loading using HNN in the EW direction with 100% of amplitude (PGA of 0.8 $[g]$).

4.4 Dynamic characterization

The last step before performing dynamic nonlinear analysis is to do an eigenvalue analysis on Seismostruct to obtain the main vibration modes and their frequency.

The three main vibration modes of UWS1 and their period are the following:

- EW direction along the weak axis: 0.21 $[s]$
- NS direction along the strong axis: 0.20 $[s]$
- Torsion: 0.08 $[s]$

The three main vibration modes of UWS2 and their period are the following:

- EW direction along the weak axis: 0.21 $[s]$
- NS direction along the strong axis: 0.17 $[s]$
- Torsion: 0.07 $[s]$

The marginal difference observed can be attributed solely to the distinct material properties, as this represents the sole disparity between the two models. These values will be employed to use the Rayleigh damping model discuss in the next section.

4.5 Nonlinear dynamic analysis

Dynamic analyses mirror the forthcoming experimental campaign. To manage the multitude of parameters, a judicious selection process was necessary. The aim was to identify critical variables that effectively encapsulate the overall behavior of the two walls, facilitating inter-comparison and alignment with experimental outcomes. Additional parameters required for the blind prediction task will be developed in Section 4.7.

4.5.1 Damping model

In nonlinear dynamic analysis, structures dissipate energy from earthquakes through both hysteretic and non-hysteretic damping. While the former is accounted for in the model, the latter involves factors like friction between structural parts, cracked concrete friction, and energy radiation. According to Chopra (2012) [31] and the "Earthquake Engineering" course of Prof. Almeida [29], the damping that is not explicitly modelled, can be approximated using Rayleigh damping, with damping coefficient ranging from 1%

to 8%, dependent on various factors.

Since UWS1 and UWS2 are essentially core walls without any significant interfering elements for damping, a small damping coefficient of 1% will be employed using the two periods of 0.21 $[s]$ from the weak axis and 0.08 $[s]$ from torsion for UWS1 and using the two periods of 0.2 $[s]$ from the weak axis and 0.07 $[s]$ from torsion for UWS2.

4.5.2 Comparison of dynamic loading with static pushover

In the inaugural nonlinear dynamic analysis, the HNN and HNE ground motions will be applied in the EW and NS directions, respectively. The loading protocol is depicted in Figure 4.7 and Figure 4.8 encompassing GM1 to GM8 as developed in Table 4.4.

The primary objective of this analysis is to juxtapose the results of the static pushover analysis, where displacement is applied at the center of the wall's mass, with those of the dynamic analysis for UWS1. Both direction displacements, in $[mm]$, are measured at the middle of the collar, at 4.29 $[m]$ from the foundation and are illustrated in Figure 4.24 for the EW and in Figure 4.25 for the NS direction.

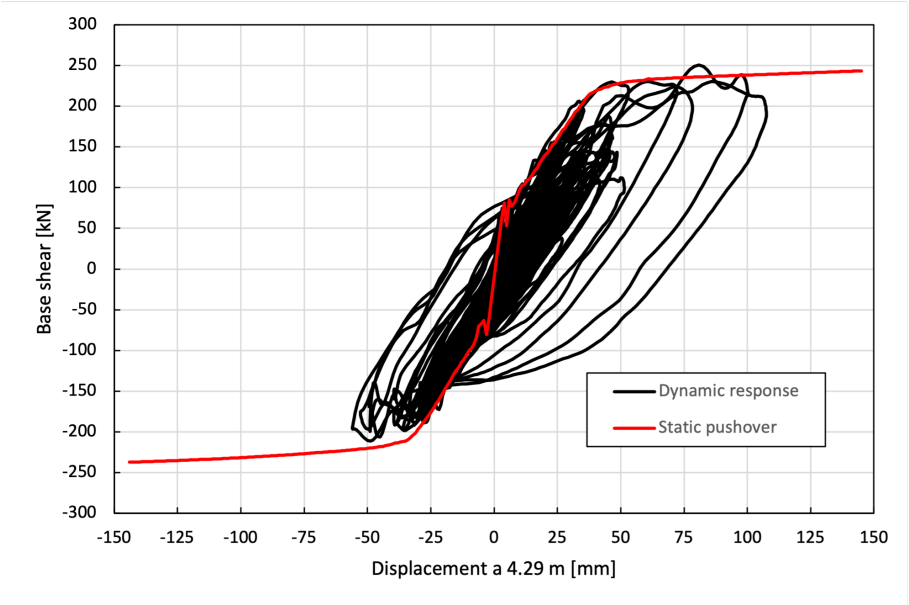


Figure 4.24: Force-displacement relationship of UWS1, EW static pushover and dynamic response.

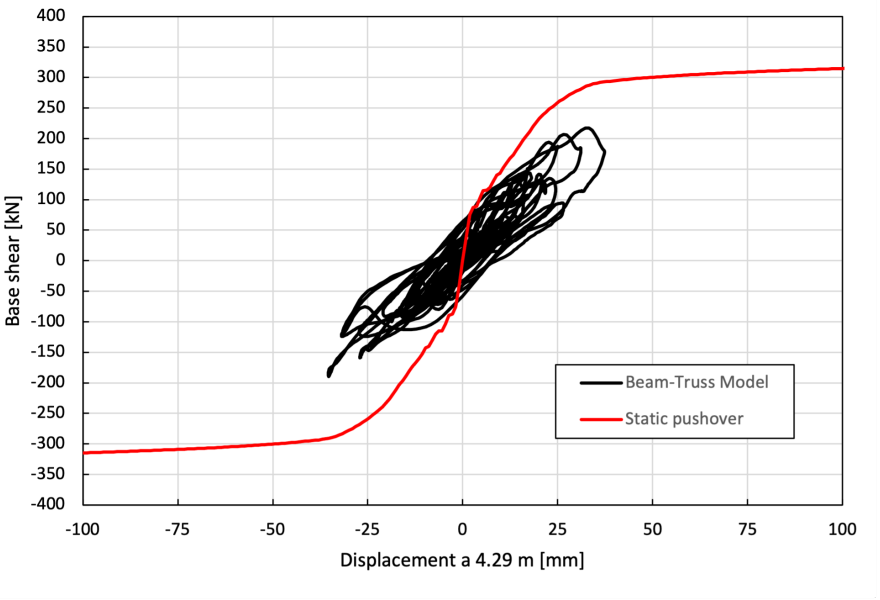


Figure 4.25: Force-displacement relationship of UWS1, NS static pushover and dynamic response.

The first Figure 4.24, illustrates some high displacements in the EW direction, a noteworthy observation as the goal of the experimental campaign is to assess wall failure. The second Figure 4.25, displays a smaller response regarding the capacity of the wall. The variation in stiffness within the dynamic loading regime might be attributed to torsional actions that influence the stiffness profile of the curve.

4.5.3 Dynamic analysis

The full response over time under dynamic loading scenarios GM1 to GM8 is visually depicted in Figures 4.26 and 4.28 for the displacement in the EW direction for UWS1 and UWS2, respectively. Correspondingly, Figures 4.29 and 4.29 portray the evolution of base shear for the EW direction.

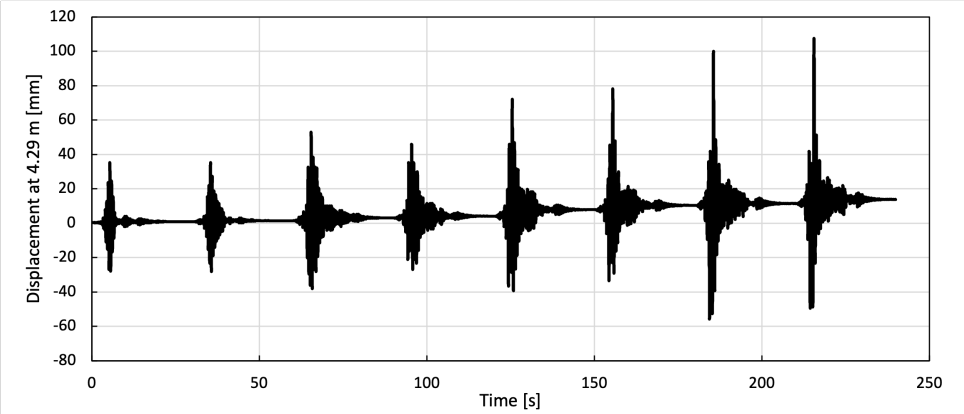


Figure 4.26: Relative displacement-time relationship of UWS1, full dynamic response in EW direction.

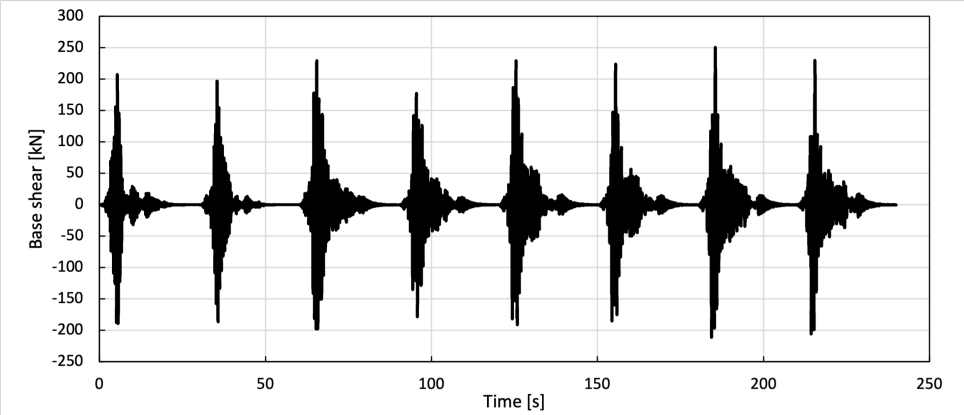


Figure 4.27: Base shear-time relationship of UWS1, full dynamic response in EW direction.

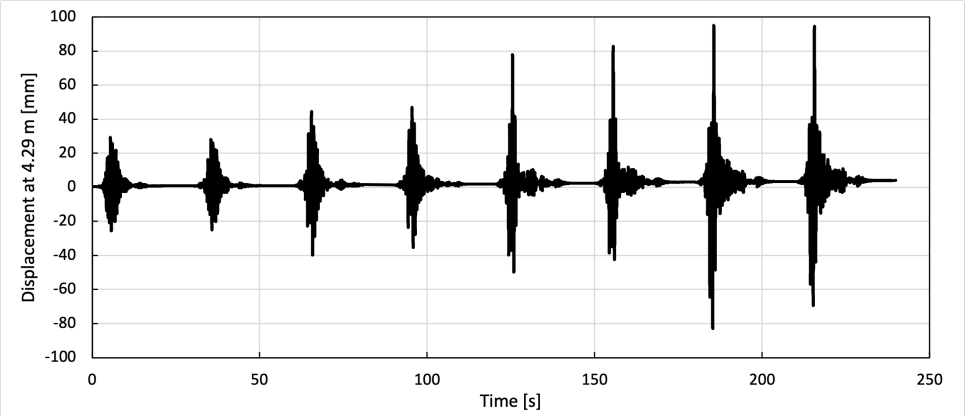


Figure 4.28: Relative displacement-time relationship of UWS2, full dynamic response in EW direction.

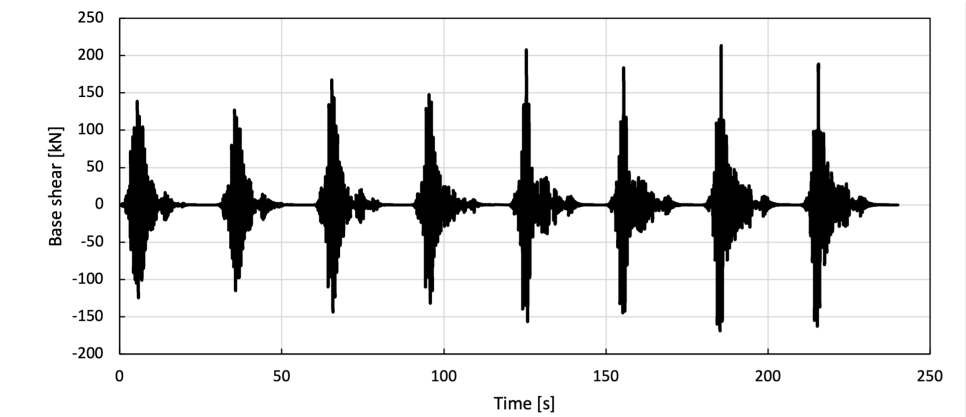


Figure 4.29: Base shear-time relationship of UWS2, full dynamic response in EW direction.

Various amount of parameters to represent the behavior of the wall are available in Seismostruct but only a few will be discussed. Section 4.7 will outline the criteria of the blind prediction competition aimed at an open competition to numerically model the wall without relying on the experimental results.

To facilitate in-depth analysis, specific key parameters have been identified: maximum relative displacement, maximum base shear and residual displacement. They will be depicted in Figures 4.30 and 4.31 for the EW direction, while in Figures 4.32 and 4.33 for the NS direction. Both UWS1 and UWS2 units are represented. All these values are absolute and the previously described GM scenario was applied to have the accumulation effect.

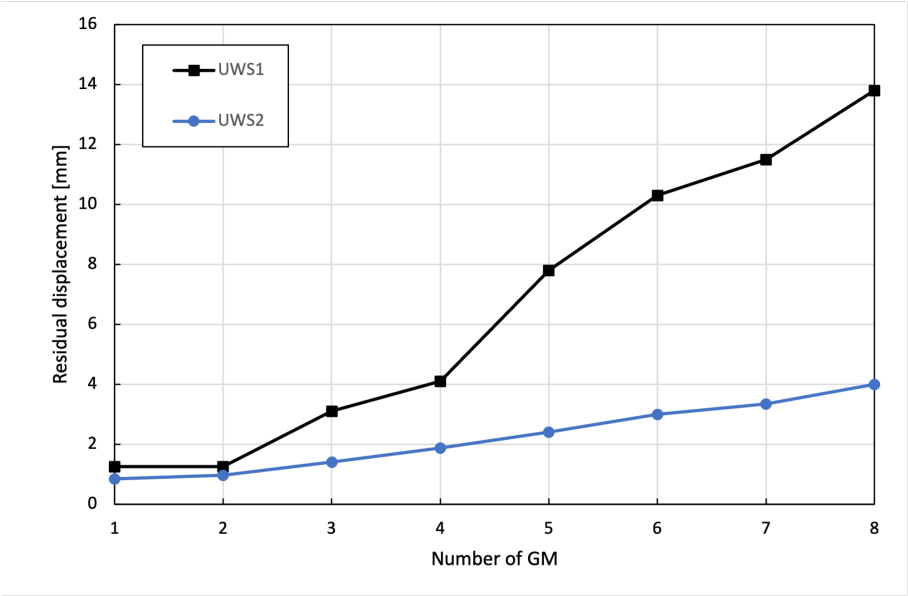
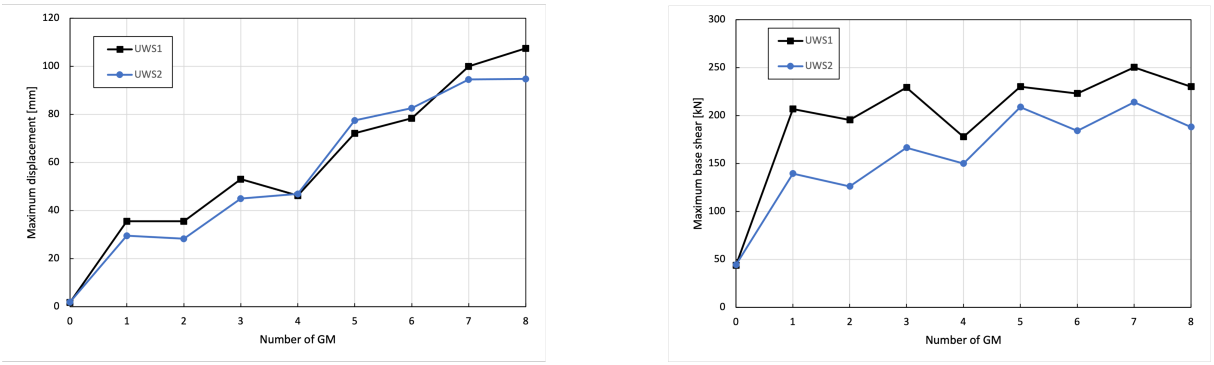


Figure 4.30: Evolution of residual displacement in EW direction of UWS1 and UWS2.



(a) (b)

Figure 4.31: Evolution of (a) maximum displacement and (b) maximum base shear in EW direction of UWS1 and UWS2.

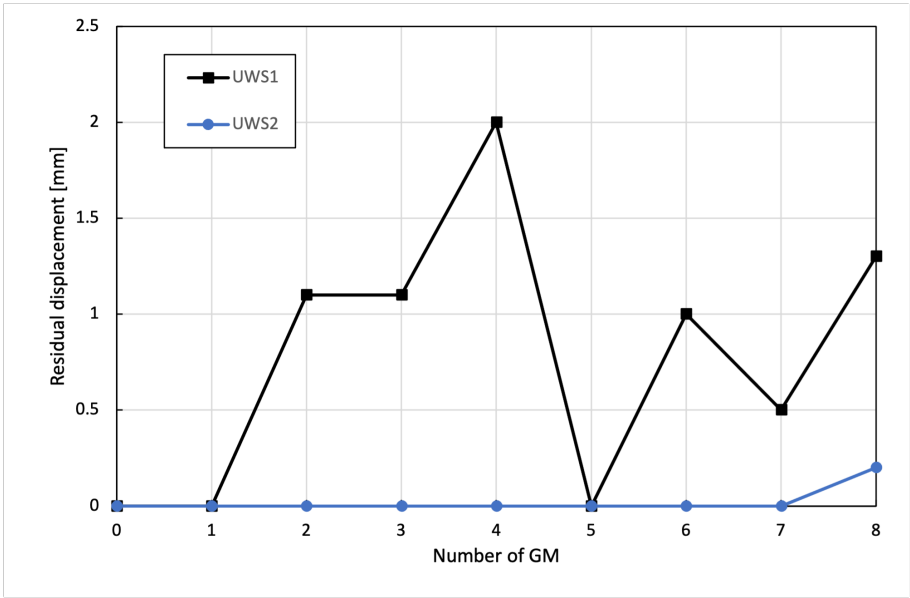
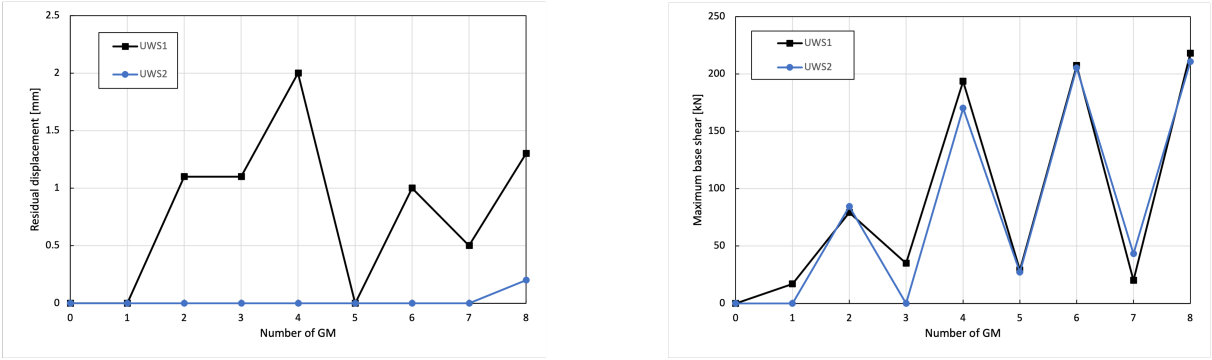


Figure 4.32: Evolution of residual displacement in NS direction of UWS1 and UWS2.



(a) (b)

Figure 4.33: Evolution of (a) maximum displacement and (b) maximum base shear in NS direction of UWS1 and UWS2

Similar to the behavior observed in quasi-static loading, SMAs demonstrate a significant effect in reducing residual displacement under dynamic loading conditions. However, their influence on maximum displacement and base shear is negligible. As discussed in Section 3.3 and evidenced by the RC+SMA model validation, the reliability of the SMA model in predicting residual displacement is limited.

After the final GM, a substantial reduction of 71% in residual displacement was observed. As a comparison, the static test from Almeida et al. (2020) developed in Section 2.2.3.1,

exhibited a 67% reduction in residual displacement between the RC and RC+SMA walls. The results obtained from this dynamic analysis and the influence of SMA are of substantial importance for future comparisons with forthcoming experimental tests.

4.5.4 Torsional dynamic analysis

A main aspect of the ALL4wALL campaign is to analyse the torsion under biaxial dynamic loading. The rotation in $[mrad]$ and the torque in $[kNm]$ are obtained with the exact same formula of Equation 3.1 and 3.2 of UW2 in Section 3.1.4. The torsional response of UWS1 and UWS2 are depicted respectively in Figures 4.34 and 4.35.

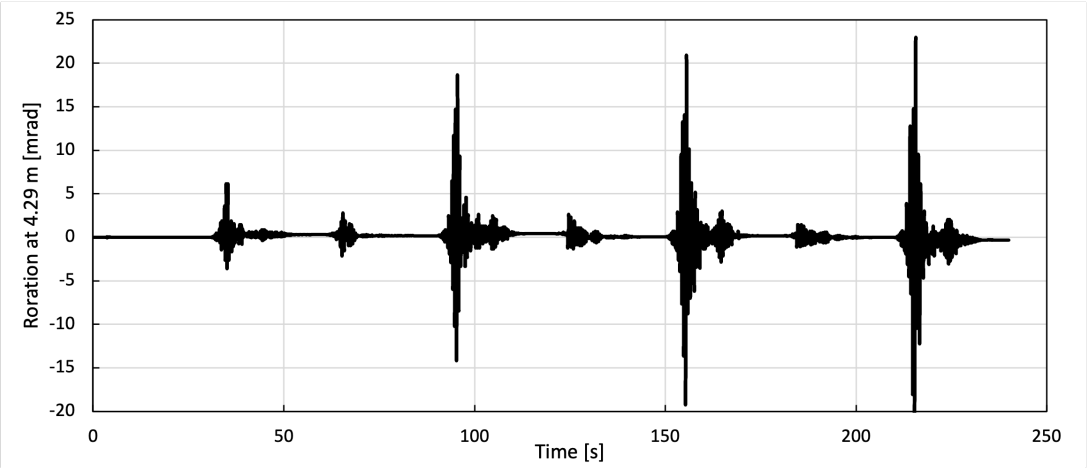


Figure 4.34: Time-rotation response at 4.29 $[m]$ response of UWS1.

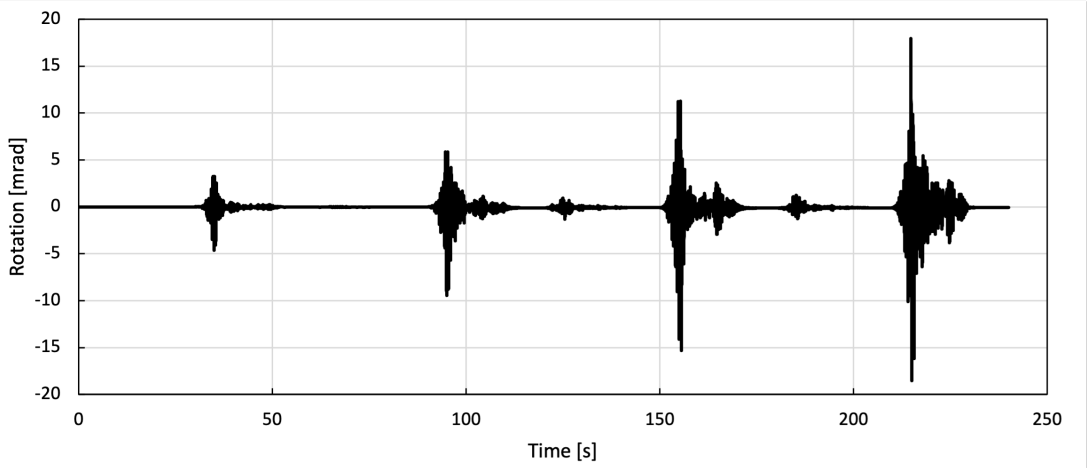


Figure 4.35: Time-rotation response at 4.29 $[m]$ response of UWS2.

The objective of inducing torsion using two ground motions in both horizontal axes has been achieved, with a maximum demand of 23 [$mrad$] for UWS1 and 18 [$mrad$] for UWS2. During the torsional analysis of UWS1 and UWS2, no discernible impact of the collar rigidity was observed, unlike the case of UW2. This disparity in behavior might be attributed to factors such as the presence of the intermediate slab, a different collar or distinct wall dimensions that could also potentially introduce inaccuracies into the results. Further exploration of torsion and beam-truss modelling is warranted as additional torsion tests become available. A summary of the predicted results for the blind prediction is provided in Section 4.7.

4.6 Influence of mass position

The UW1 experimental results, developed in Section 3.1, were influenced by the position of the application of the axial forces. The purpose of this section is to discern the influence of the center of applied mass position on results such as maximum displacement, base shear, and residual displacement during both quasi-static and dynamic loading. The analysis will be conducted with the RC wall UWS1.

4.6.1 Static analysis

Figure 4.36 depicts various static pushover analyses conducted in the East direction, maintaining the previously established modelling approach while introducing top mass displacement within the range of -200 to +200 [mm] (West-to-East direction considered positive).

For instance, with the UWS1 wall, an offset of 148 [mm] was introduced for the applied center of mass in relation to the center of mass of the wall, as illustrated previously in Figure 4.4b. In the simulation labeled "+100 [mm]," the wall was modelled with all stacks of masses shifted 100 [mm] to the East, the center of the applied mass offset was 248 [mm].

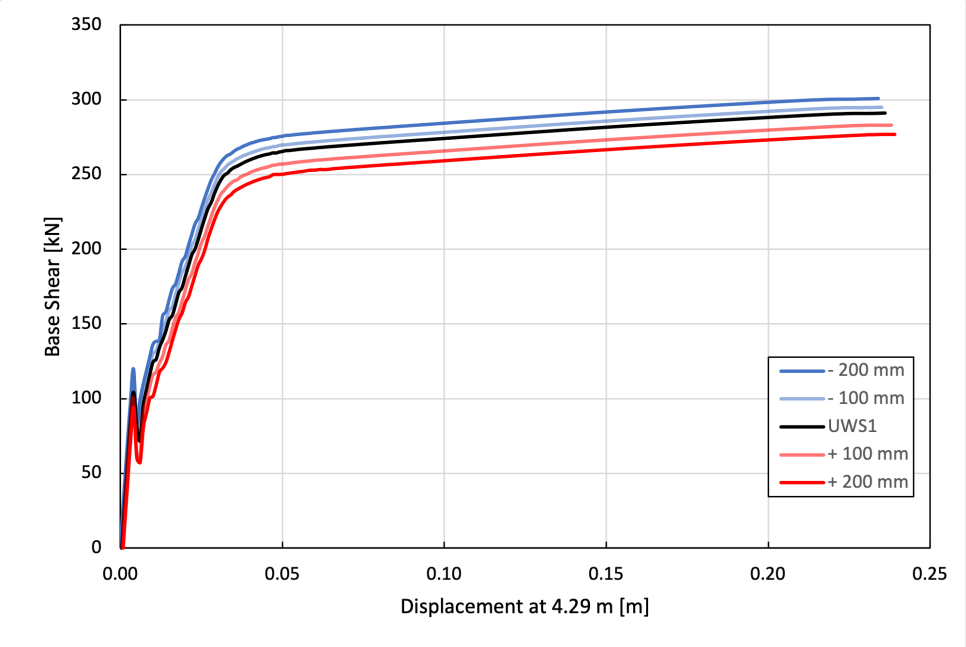


Figure 4.36: Force-displacement response of UWS1 with various positions of the top masses, West-to-East static pushover.

A conspicuous trend emerges, revealing a reduction in base shear strength as the positive offset increases. This analysis exhibits analogous behavior but in the opposite direction when the wall is pushing to the West (not represented), the base shear strength increases as the positive offset increases.

4.6.2 Dynamic analysis

A dynamic loading in the EW direction was simulated using the HNN MZ04, described in Section 4.1.4, with 100% of the amplitude (PGA of 0.808 $[g]$). No acceleration was applied in the NS direction. Adequate time was allotted for the wall to revert to its initial position, facilitating the measurement of residual displacement. The maximum displacement was measured at the middle of the collar, at 4.29 $[m]$.

The evolution of residual displacement is depicted in Figure 4.37, while the trends for maximum displacement and base shear are respectively illustrated in Figures 4.38a and 4.38b.

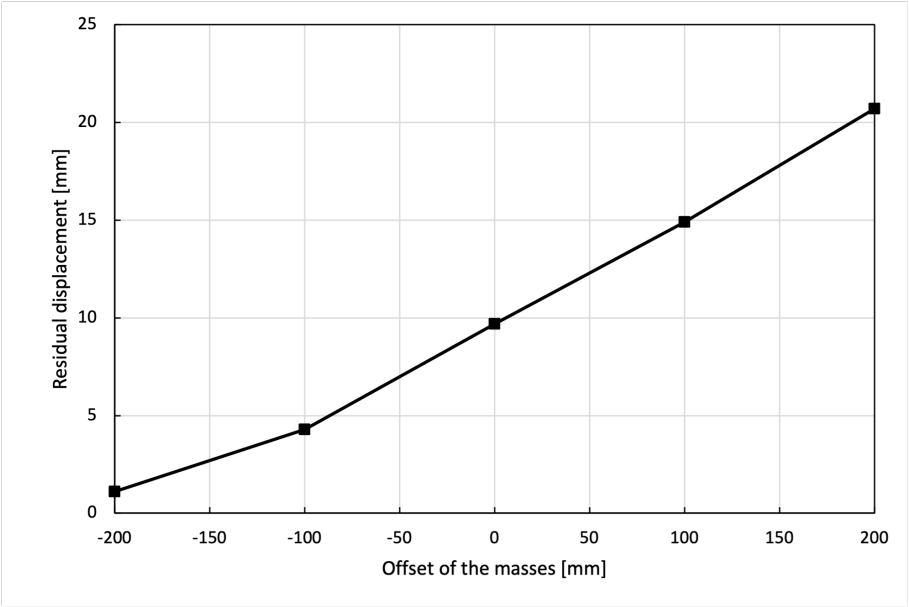
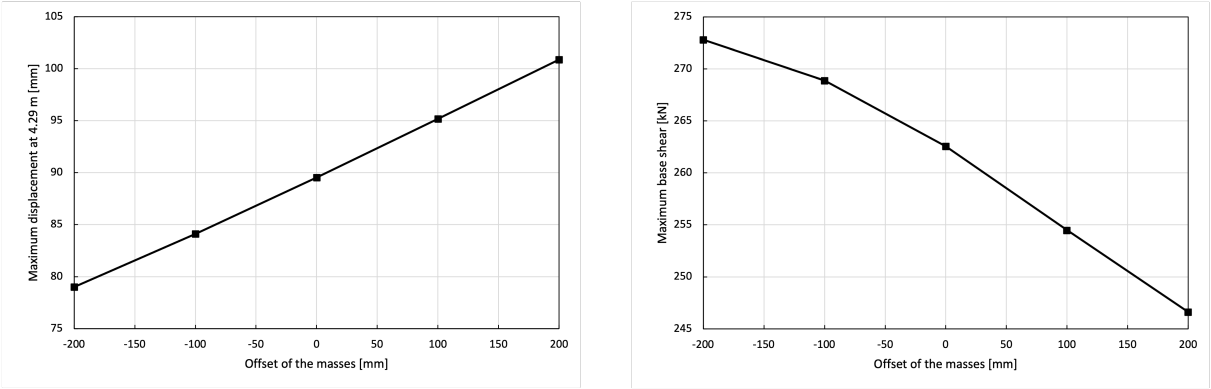


Figure 4.37: Evolution of residual displacement regarding the position of the axial load, dynamic analysis.



(a) (b)

Figure 4.38: Evolution of (a) maximum displacement and (b) maximum base shear regarding the position of the axial load, dynamic analysis.

An impressive linear relation between the position of the wall and the residual displacement can be observed. Shifting the equivalent axial force closer to the wall's web results in reduced residual displacement, as well as decreased maximum displacement and an increase of maximum base shear strength, resulting in a wall with improved performance. In practical applications involving taller core walls, this influence might become even more pronounced. While conducting further investigations and experimental studies in this area could yield valuable insights, it falls beyond the scope of the current study's defined objectives.

4.7 Blind prediction

The documents pertaining to the blind prediction competition [27] provide comprehensive details about the wall and elucidate the distinct criteria used to score points based on the precision of comparisons with future tests. The accumulation of points reflects the accuracy of the model's predictions. The author has endeavored to provide the best possible predictions across these various criteria. It's important to note that the blind prediction will be updated with real material strength, a new ground motion and a new blind prediction for UWS2 might go out. The objective in this section is to have a general overview of the values to compare them in the future with real experimental results and ascertain the model's accuracy. The criteria for UWS1 and UWS2 are presented in the to following sub-sections.

4.7.1 UWS1 prediction

- Failure mode: due to the inaccurate use of performance criteria, the author prefers not assume this answer. The performance criteria did not predict a failure even if the confined concrete was close to crushing (91%).
- Max displacement in the EW direction at 4.29 $[m]$: 107.5 $[mm]$.
- Max lateral EW inertial force, obtained by multiplying the maximum acceleration at 4.29 $[m]$ and the imposed mass on wall unit: 8.2 $[m/s^2]$ x 28.23 $[ton]$ = 229.8 $[kN]$.
- Maximum tensile strain experienced by the rebar in the flange end: 2.14%.
- Maximum residual displacement at 4.29 $[m]$: 13.8 $[mm]$.
- Energy Dissipated: no studied.
- Maximum yielding height experienced by the rebar in the flange end: 1.6 $[m]$.
- Relative displacement-time history at h = 4290 $[mm]$: as depicted in Figure 4.26.
- Relative torsional rotation time history at h = 4290 $[mm]$: as depicted in Figure 4.34.

4.7.2 UWS2 prediction

These results were predicted with 32 [cm] of SMA in the corners and flange ends, as described in Chapter 4

- Failure mode: Due to the inaccurate use of performance criteria, the author prefers not assume this answer. These performance criterion did not predict a failure, the crushing of confined concrete was only at 55% from its reached point.
- Max displacement in the EW direction at 4.29 [m]: 94 [mm].
- Max lateral EW inertial force, obtained by multiplying the maximum acceleration at 4.29 [m] and the imposed mass on wall unit: 7.6X [m/s^2] x 28.23 [ton] = 229.8 [kN].
- Maximum tensile strain experienced by the rebar in the flange end: 5.4%.
- Maximum residual displacement at 4.29 [m]: 4 [mm], although this prediction is based on the inaccurate SMA model for representing residual displacement, it may not be accurate.
- Energy Dissipated: not studied.
- Maximum yielding height experienced by the rebar in the flange end: 1.6 [m].
- Relative displacement-time history at h = 4290 [mm]: as depicted in Figure 4.28 .
- Relative torsional rotation time history at h = 4290 [mm]: as depicted in Figure 4.35.

These values hold significance when compared to future measurements or other modelling approaches, which will aid researchers in the context of the ALL4wALL project. Should the reader seek further details about the numerical results, feel free to reach out to the author.

Chapter 5

Conclusion and Further Developments

The objective of the master thesis has been dedicated to the numerical modelling of two RC U-shaped walls, UWS1 and UWS2, integral to the ALL4wALL project, an expansive European experimental campaign. These non-planar walls, each weighing 40 tons and measuring over 6 meters in height, will be tested under dynamic conditions on the LNEC 3D shake table in Lisbon, following the completion of this thesis. The aim of this project is to analyses the influence of shape memory alloy (SMA) on residual displacement, observe the influence of torsion during bidirectional loading and increase the database of large-scale experimental tests. To realize this multifaceted aim, the experimental campaign will involve the testing of two distinct wall units. The first unit, UWS1, will be constructed using conventional reinforced concrete (RC) materials, while the second unit, UWS2, will incorporate the application of shape memory alloy (SMA), a superelastic material.

The methodology employed to numerically simulate the behavior of the units was beam-truss modelling (BTM), which entails the creation of a mesh comprising beams for vertical and horizontal elements, as well as trusses for diagonal components. The first objective was to understand BTM, study previous experimental campaigns, analyse material models, and learn Seismostruct through a literature review.

Afterward, to refine and calibrate the numerical model, validation was performed. It consists to analyse previous experimental testing and study the difference between the model and the experimental results. UWS2 will be the first U-shaped wall with SMA ever tested under dynamic loading, so various types of walls were modelled to calibrate its model: two U-shaped walls under static bending loading, a U-shaped wall under torsional static loading, a planar wall with SMA under static loading and a U-shaped wall under dynamic loading.

The outcomes of this study unveiled the strengths and limitations of the beam-truss modeling approach. It demonstrated commendable accuracy in capturing stiffness, maximum displacement, and deformation profiles in both dynamic and static scenarios. Furthermore, the model's adaptability and user-friendly interface of Seismostruct facilitated calibration and manipulation.

However, a misunderstanding of the behavior in the diagonal elements during ultimate displacement in static pushover led to omitting geometrical nonlinearities. This affects slightly the behavior of slender walls. The only SMA material model from the software does not accurately represent the residual displacements. The torsion was also a challenge to model, the use of elastic rigid elements to represent the collar of walls seems to influence the torsional response. Moreover, the additional damping during dynamic analyses, represented by the Rayleigh damping model is difficult to assume and should be calibrated using experimental data, which is not always possible. The use of not complete performance criteria, the failure of the walls was inaccurately simulated.

Despite these challenges, a promising numerical simulation of the UWS1 and UWS2 units was conducted: a static pushover and cyclic loading; a good prediction of the wall inelastic demand using the N2 method from the Eurocode 8; a dynamic analysis employing a ground motion of the 30 October 2016, central Italy earthquake, increasing its PGA step by step in the two horizontal directions, to observe the evolution of the maximum displacement, the maximum shear force and the residual displacement. The use of two directions of loading induced torsion in the wall. This numerical analysis was performed on both walls to observe the impact of the SMA at the bottom of the boundary elements of UWS2.

The use of SMA involves an impressive reduction of residual displacement, around 40% of reduction on static loading and 70% dynamic loading. Torsion is also minimized, while the relative maximum displacement and the base shear stay identical. These analyses are made with caution because the SMA material model was not perfectly accurate. If this assumption is true, SMA could improve the structural behavior of medium to high buildings in seismic regions. Another analyse conclude that shifting the position of application of the axial load would reduce the maximum relative displacements and the residual displacements of the wall under dynamic loading. This series of analyses is concluded by a summary of the predicted behavior of the UWS1 and UWS2 for the ALL4wALL blind prediction competition.

This master thesis was the opportunity to validate BTM for non-planar walls under static and dynamic loading and to observe the influence of SMA. The overarching goal was to contribute valuable insights to the researchers in the ALL4wALL project by providing them a dataset to analyse and to adapt the future test that will be performed at the LNEC 3D shake table.

Further developments include post-experimental calibration of the model, incorporating final modifications and conducting comparative analyses. The examination will encompass the influence of the limitations developed before. A final investigation about beam-truss modelling could be useful to understand where the problem of geometrical nonlinearity comes from; if a better material model provides an accurate simulation of the residual displacements and if so, is it a real breakthrough for earthquake engineers; if the torsion in non-planar RC walls could be modelled without uncertainties and validate with forthcoming tests.

From a personal perspective, I have gained significant insights through the completion of this master thesis. The opportunity to engage in my inaugural international research project, interact with esteemed professors, and enhance my English writing and presentation proficiencies over the course of the year has been invaluable. While my direct involvement with this subject concludes here, I intend to maintain a keen interest and follow its progress closely. I aspire to remain abreast of developments, to contribute to the ongoing transformation of the construction realm. This master thesis will serve as a stepping stone toward a future marked by enhanced understanding, innovation, and resilience in the realm of structural engineering.

Appendix A

Literature Experimental Results

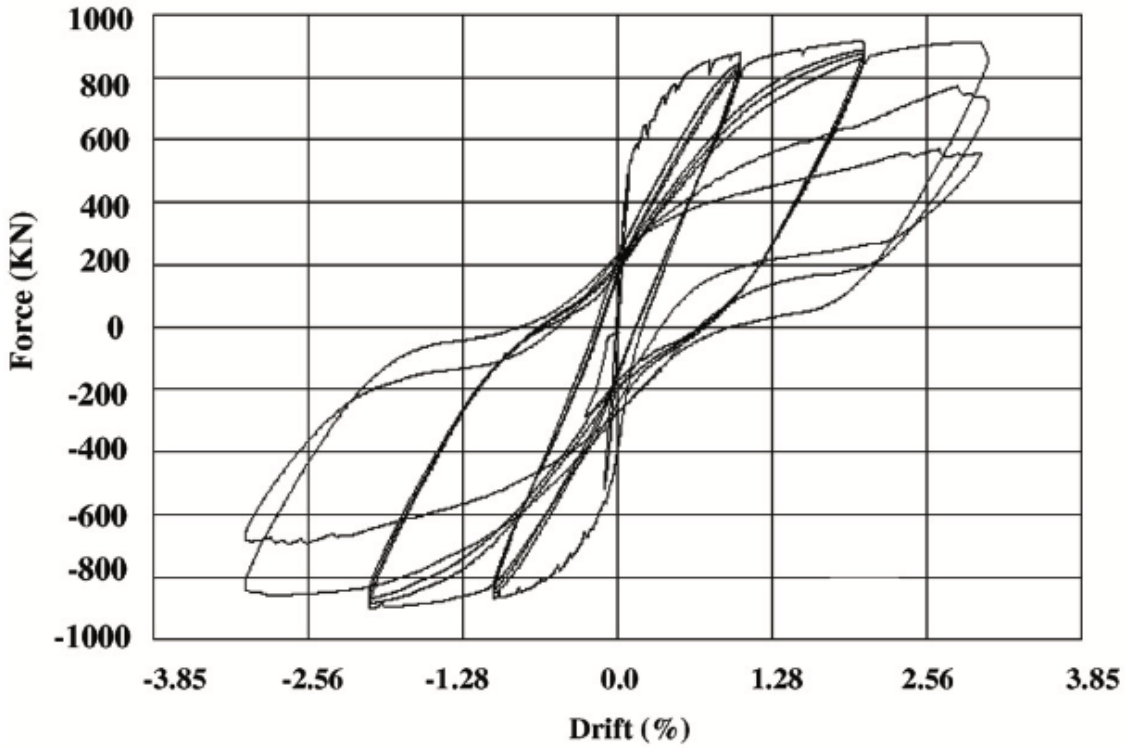


Figure A.1: "Total force versus average drift, X (EW) direction test" from Ile and Reynouard (2005).

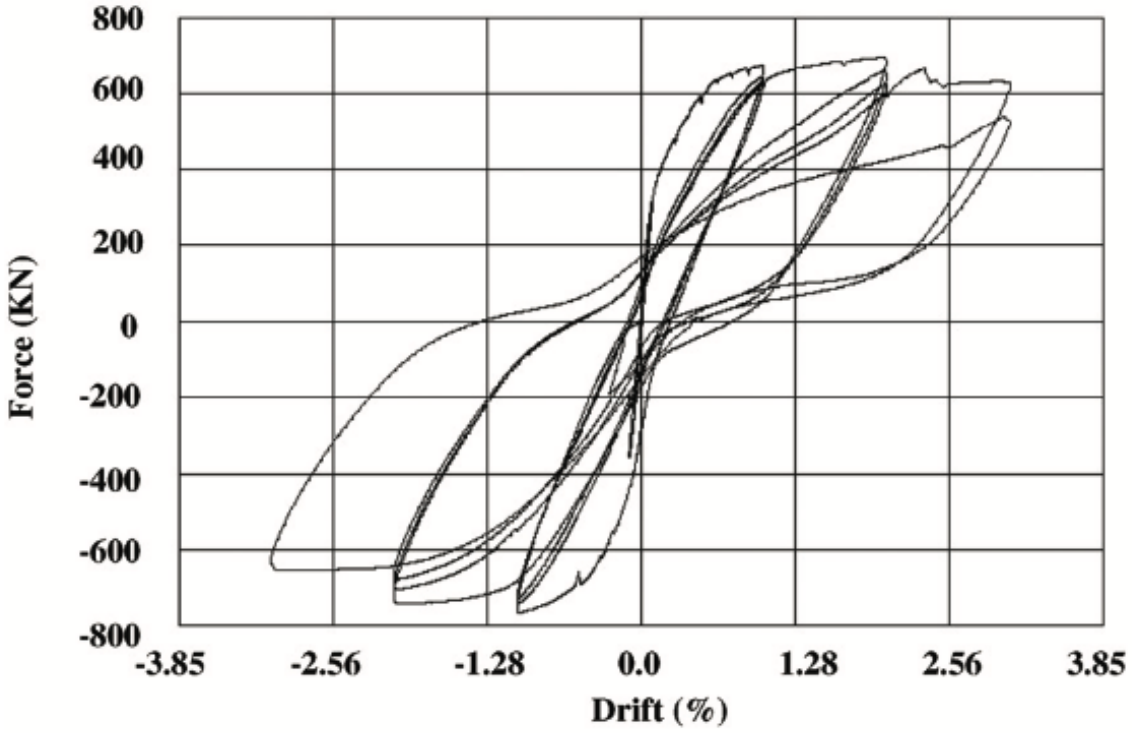


Figure A.2: "Total force versus average drift, Y (NS) direction test" from Ile and Reynouard (2005).

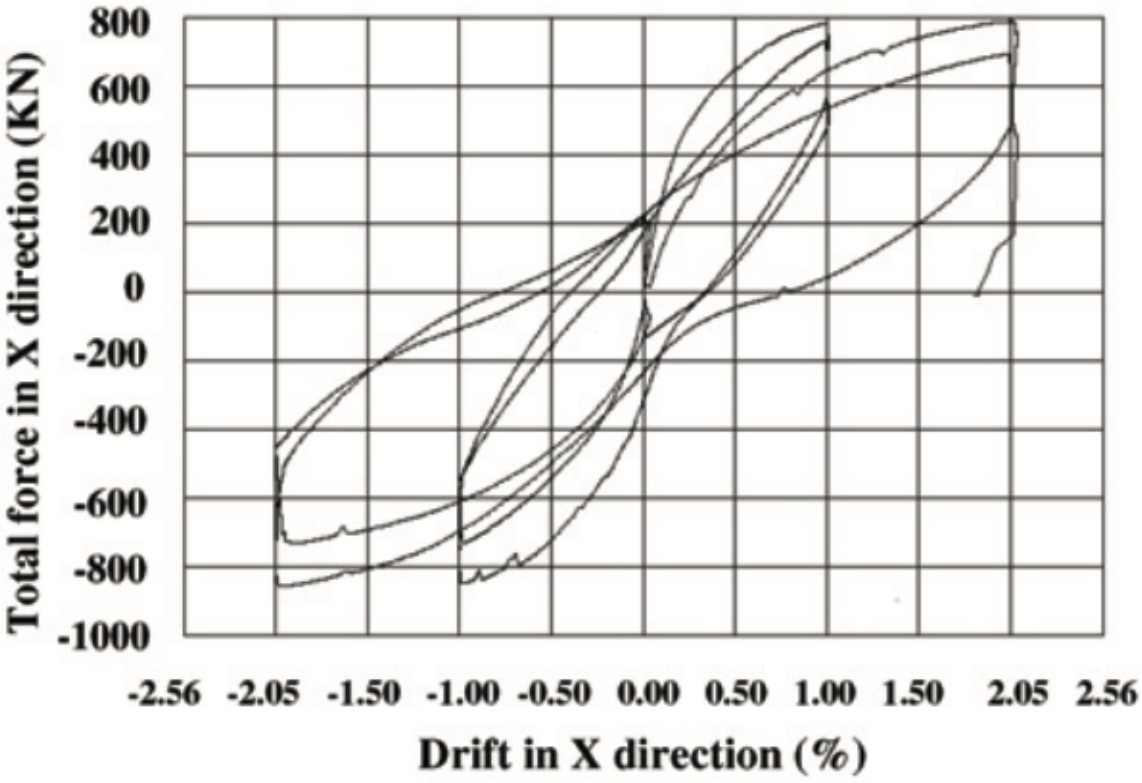


Figure A.3: "Total horizontal force versus drift - X (EW), XY direction test" from Ile and Reynouard (2005).

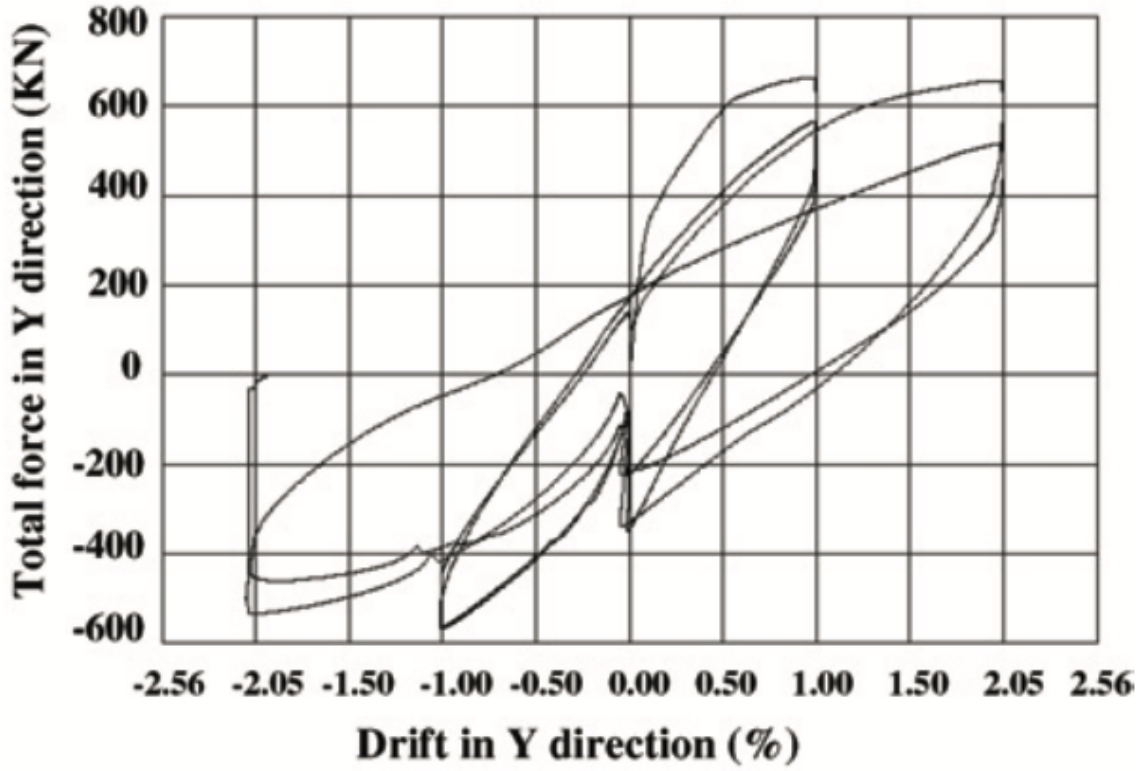


Figure A.4: "Total horizontal force versus drift - Y (NS), XY direction test" from Ile and Reynouard (2005).

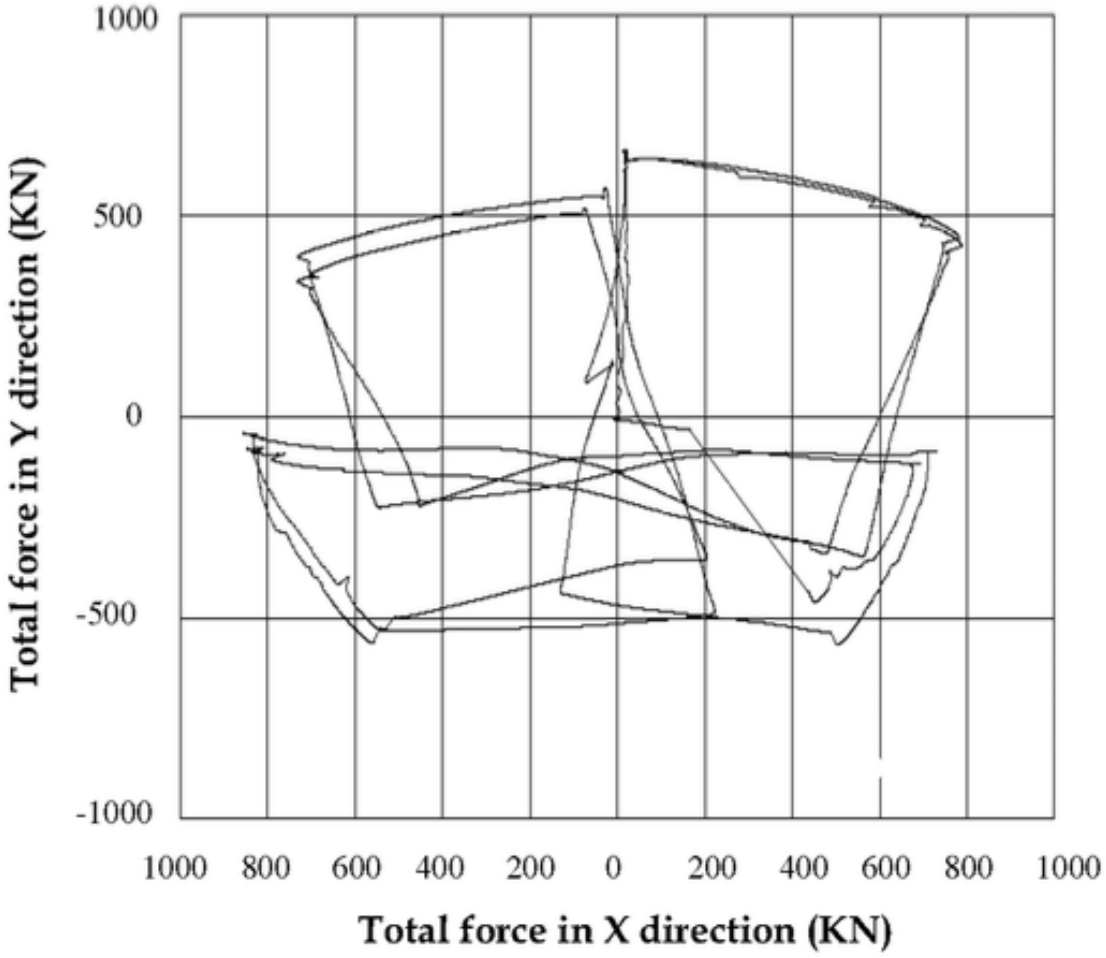


Figure A.5: "X (EW) and Y (NS) loads, XY direction test" from Ile and Reynouard (2005).

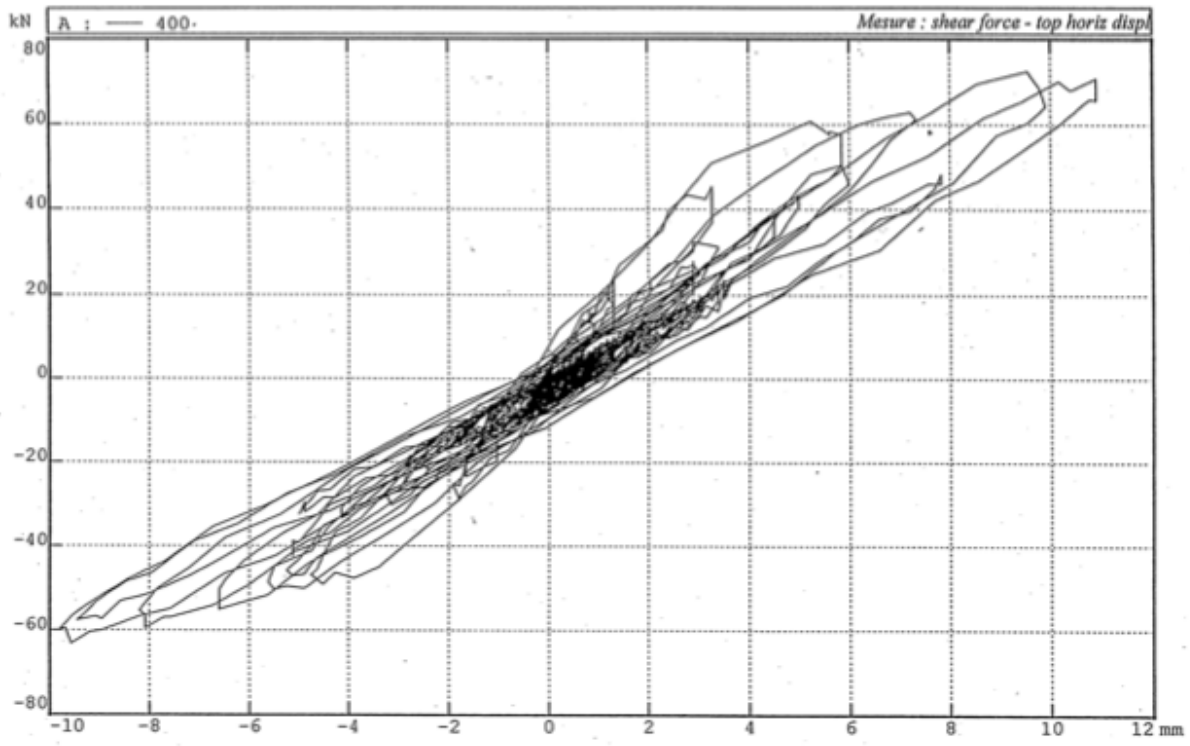


Figure A.6: "Measure : shear force-top horiz displ, wall 1 test 1" from Combescure et al. (1999).

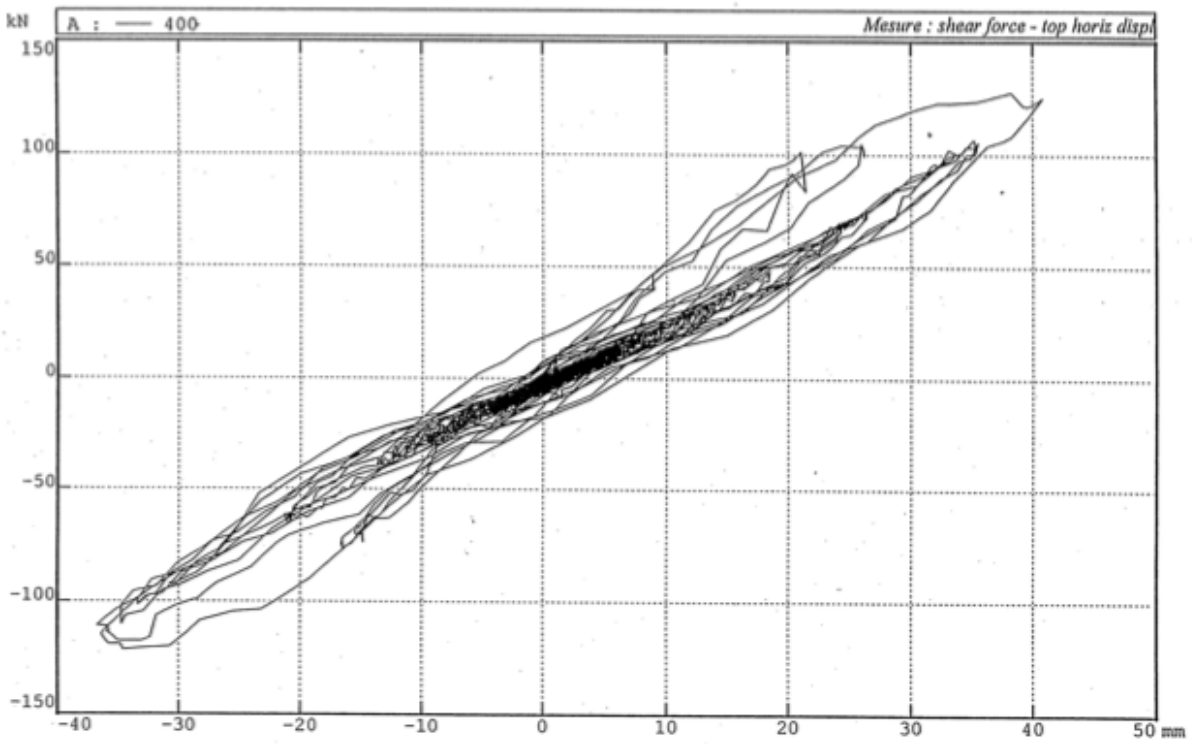


Figure A.7: "Measure : shear force-top horiz displ, wall 1 test 3" from Combescure et al. (1999).

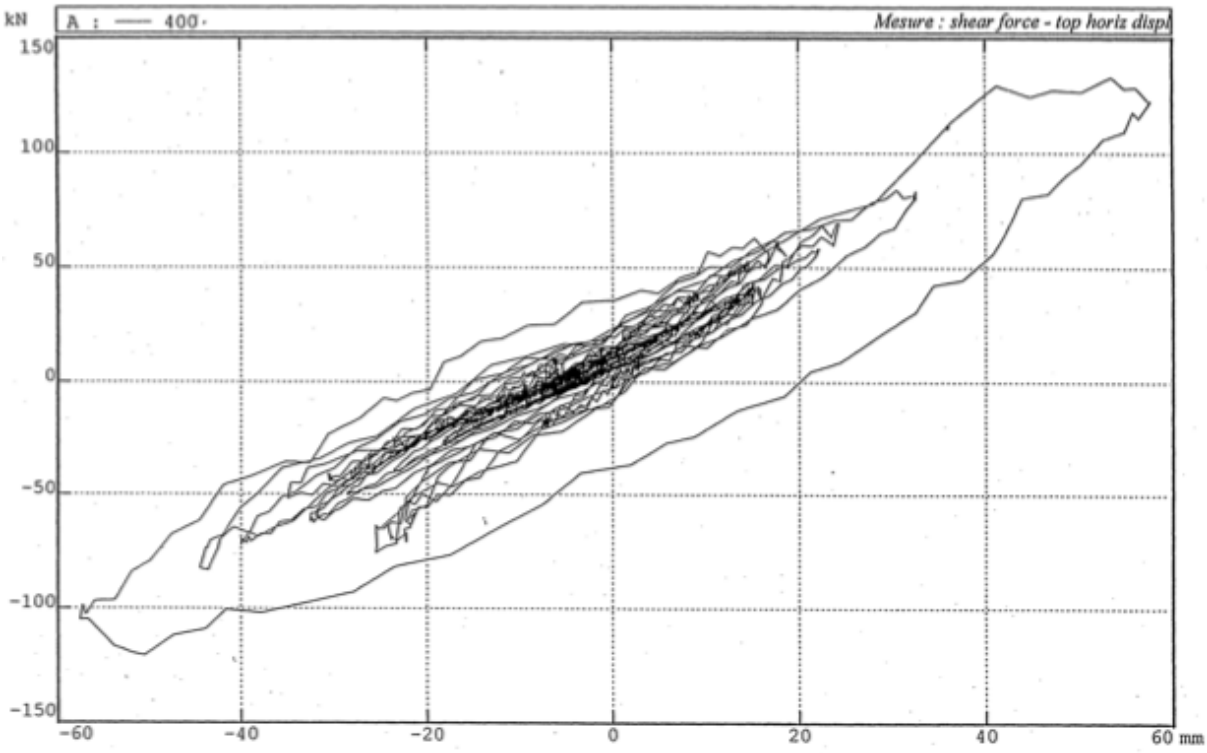


Figure A.8: "Measure : shear force-top horiz displ, wall 1 test 4" from Combescure et al. (1999).

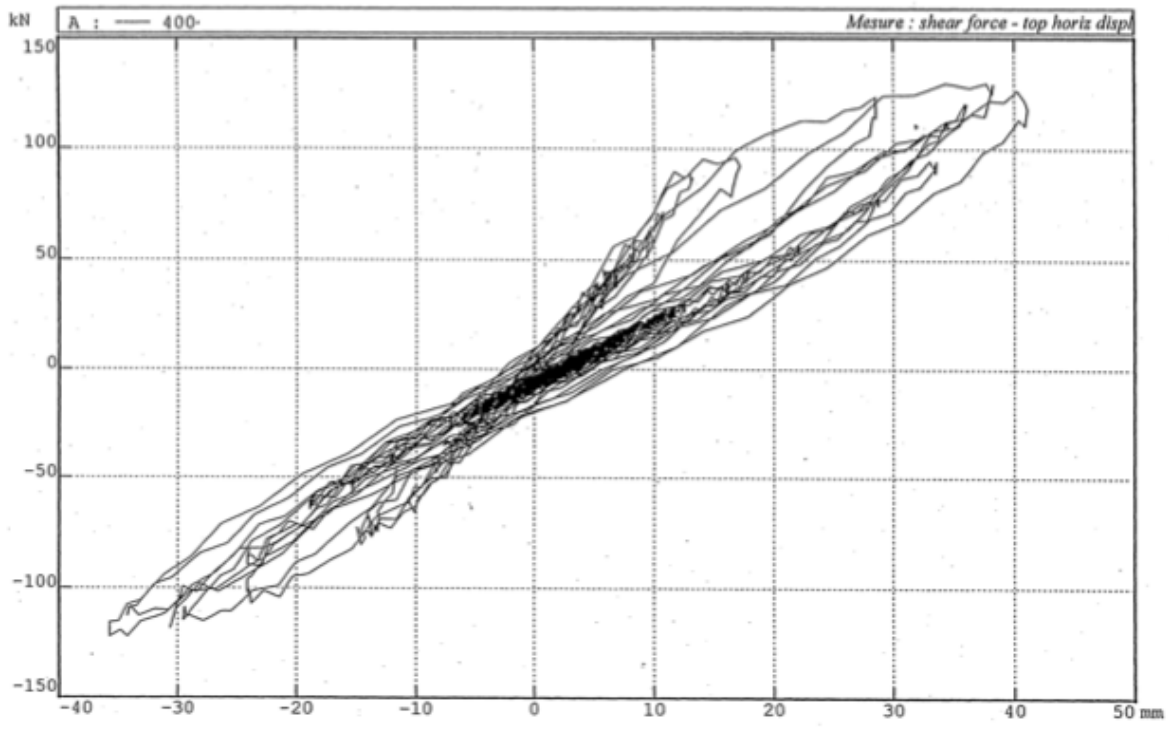


Figure A.9: "Measure : shear force-top horiz displ, wall 3 test 3" from Combescure et al. (1999).

Appendix B

Seismostruct 3D Model

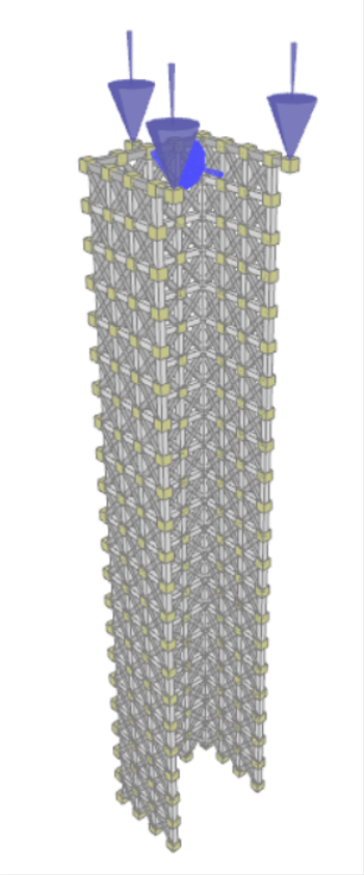


Figure B.1: Beam-truss model of UW1, Seismostruct 3D view.

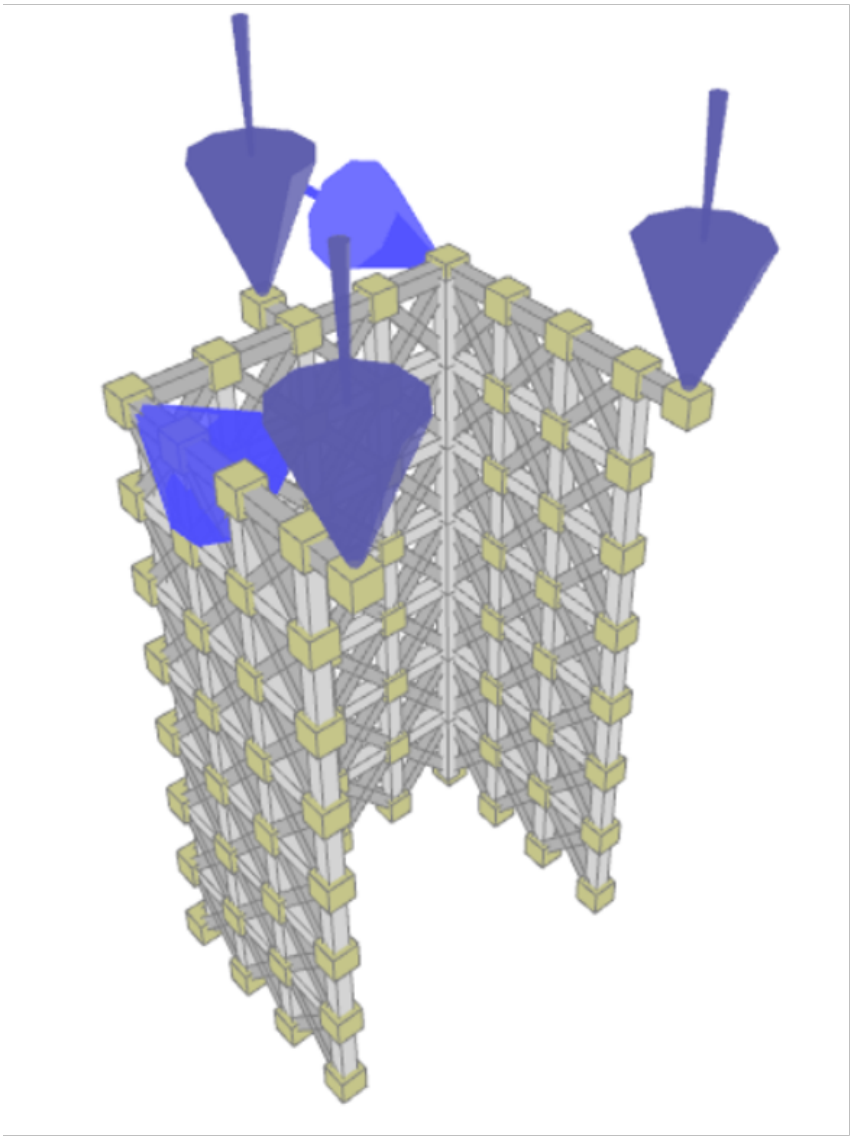


Figure B.2: Beam-truss model of UW2, Seismostruct 3D view.

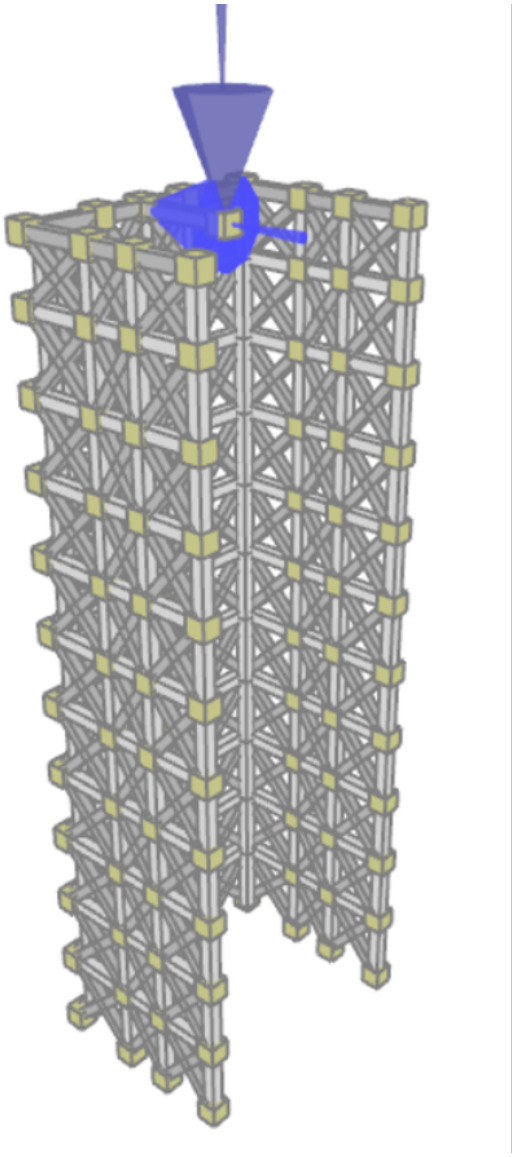


Figure B.3: Beam-truss model of IR, Seismostruct 3D view.

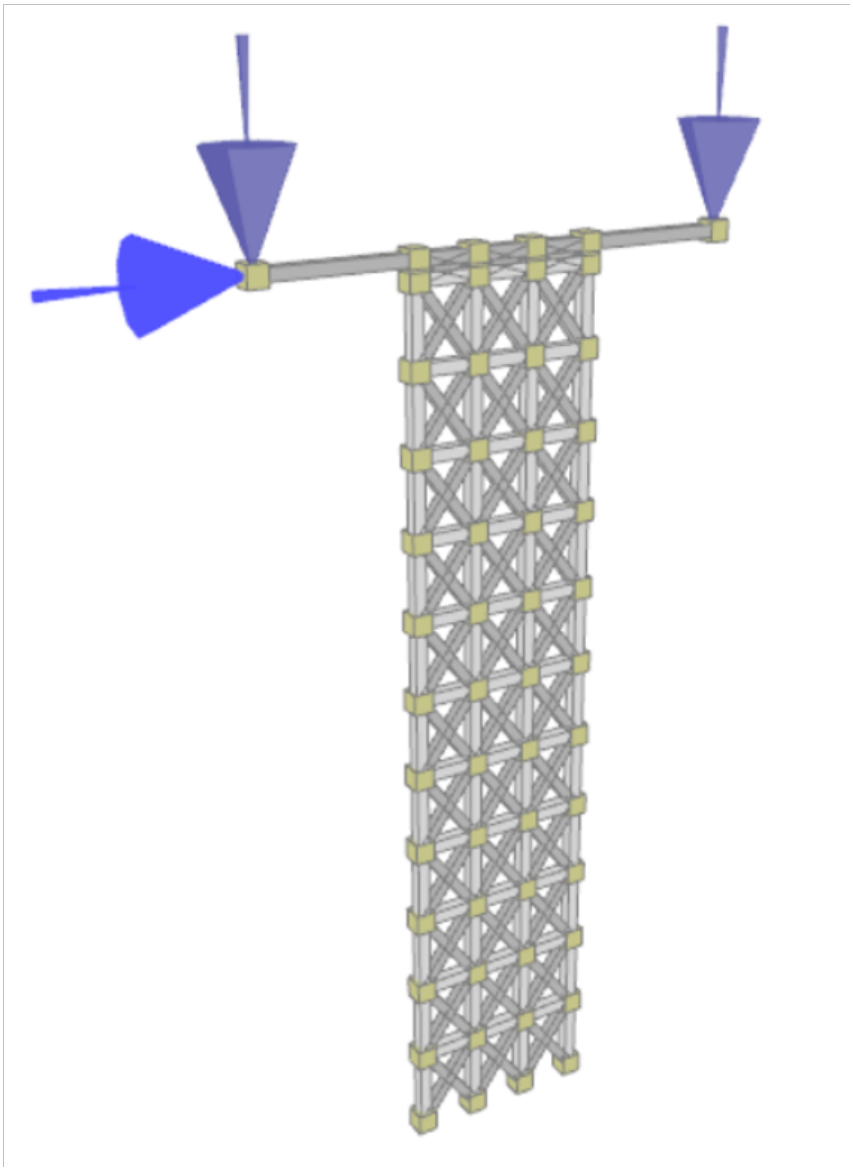


Figure B.4: Beam-truss model of RC+SMA, Seismostruct 3D view.

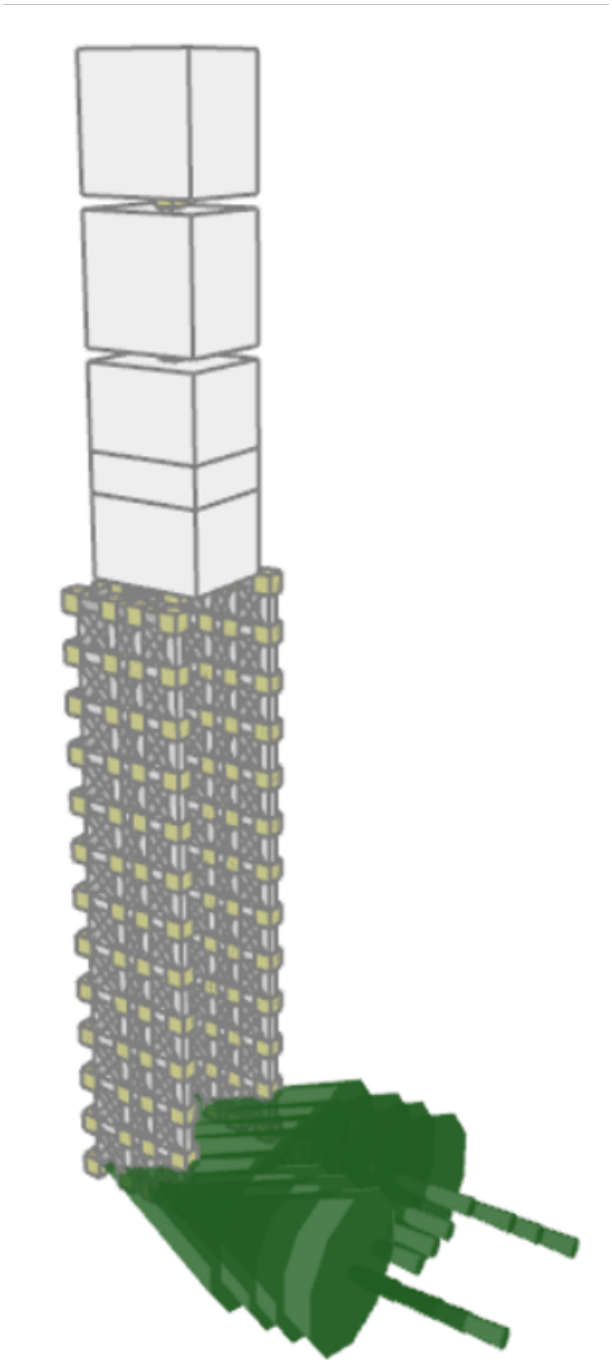


Figure B.5: Beam-truss model of CEA, Seismostruct 3D view.

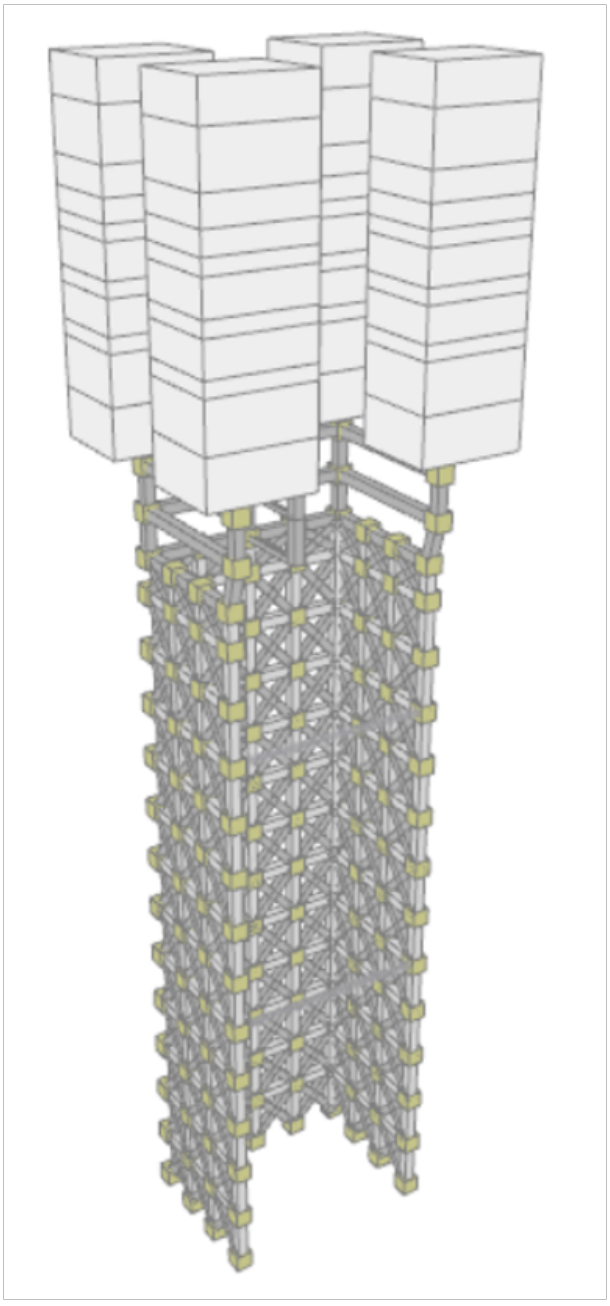


Figure B.6: Beam-truss model of UWS1/UWS2, Seismostruct 3D view.

Bibliography

[1] UN Envirpnment, ""global status report 2017,"." www.globalabc.org., 2017.

[2] Seismosoft, *Seismostruct academic version*, 2023. Available online at https://seismosoft.com/products/seismostruct/.

[3] European Committee for Standardization, Brussels, Belgium, *EN 1998. Eurocode 8: Design of structures for earthquake resistance*, 2004.

[4] "Eries website." https://eries.eu/. Accessed on 2023-06.

[5] R. Hoult, C. Doneux, and J. P. de Almeida, "Tests on reinforced concrete u-shaped walls subjected to torsion and flexure," *Earthquake Spectra*, 2022.

[6] R. Park, "Evaluation of ductility of structures and structural assemblages from laboratory testing," *Bulletin of the New Zealand National Society for earthquake engineering*, vol. 22(3), 1989.

[7] João Pacheco de Almeida et al., *Transnational Access User Project Application Form*, 2022.

[8] "Lnec website." https://www.lnec.pt/en/research/research-infrastructures/shaking-tables/. Accessed on 2023-07.

[9] N. Ile and J. Reynouard, "Behaviour of u-shaped walls subjected to uniaxial and biaxial cyclic lateral loading," *Journal of Earthquake Engineering*, vol. 90, pp. 67–94, 2005.

[10] D. Combescure, T. Chaudat, and A. Moutafidou, "Seismic tests of icons u-shaped walls," *Rapport DTM*, 1999.

[11] J. P. de Almeida, M. Steinmetz, F. Rigot, and S. de Cock, "Shape-memory niti alloy rebars in flexural-controlled large-scale reinforced t concrete walls: Experimental investigation on self-centring and damage limitation," *Engineering Structures*, vol. 220, 2020. Experimental openly data available at DOI: 10.14428/DVN/2QBQVJ.

[12] C. A. C. Noguez and M. S. Saiidi, "Shake-table studies of a four-span bridge model with advanced materials," *Journal of Structural Engineering*, vol. 138(2), 2012.

[13] M. Keirle, "Effective stiffness of non-rectangular reinforced concrete structural walls and wide-column models in seismic design and analysis," *MA thesis*, 2022.

[14] I. T. and F. M., "Assessment of a force–displacement based multiple-vertical-line element to simulate the non-linear axial–shear–flexure interaction behaviour of reinforced concrete walls," *Bull. Earthq. Eng*, vol. 17, pp. 6369–6389, 2019.

[15] "Vector3." `http://vectoranalysisgroup.com/vector3.html`. Accessed on 2023-08.

[16] P. K. and L. P., "Nonlinear seismic modeling of reinforced concrete cores including torsion," *Eng. Struct.*, vol. 136, pp. 380–392, 2017.

[17] K. Beyer, A. Dazio, and M. Priestley, "Inelastic wide-column models for u-shaped reinforced concrete walls," *Journal of earthquake engineering*, vol. 12(S1), pp. 1–33, 2008.

[18] C. Saegerman, "Influence of axial load ratio and eccentricity on the cyclic response of non-rectangular walls through beam-truss models," *MA thesis*, 2023.

[19] L. Y. and P. M, "Three-dimensional cyclic beam-truss model for nonplanar reinforced concrete walls," *Journal of Structural Engineering*, vol. 140, 2014.

[20] R. Hoult, A. A. Correia, and J. P. de Almeida, "Beam-truss models to simulate the axial-flexural-torsional performance of rc u-shaped wall buildings," *CivilEng*, vol. 4, pp. 292–320, 2023.

[21] L. Y., P. M, and K. I, "Three-dimensional beam-truss model for reinforced concrete walls and slabs—part 1: Modeling approach, validation, and parametric study for individual reinforced concrete walls," *Earthq. Eng. Struc.*, vol. 45, p. 1495–1513, 2016.

[22] M. J., P. N., and P. R., "Theoretical stress-strain model for confined concrete," *J. Struct. Eng.*, vol. 114, p. 1804–1826, 03 1988.

[23] M. M. and P. P.E., "Method of analysis for cyclically loaded rc plane frames including changes in geometry and non-elastic behavior of elements under combined normal force and bending," *Symposium on the Resistance and Ultimate Deformability of Structures Acted on by Well Defined Repeated Loads*, pp. 15–22, 1973.

[24] T. Paulay and M. J. N. Priestley, "Seismic design of reinforced concrete and masonry buildings," *Wiley New York*, vol. 768, 1992.

[25] R. Pinho, "Shaking table testing of rc walls," *ISET Journal of Earthquake Technology*, vol. 37(4), pp. 119–142, 2000.

[26] "Webplotdigitizer." `https://apps.automeris.io/wpd/`. Accessed on 2023-06.

[27] Institute of Mechanics, Materials and Civil Engineering (iMMC), *UCLouvain 2023 Blind Prediction Competition: Shake-table Response of 40-ton RC U-shaped Wall*, 2023.

[28] P. Fajfar, "A nonlinear analysis method for performance-based seismic design," *Earthq Spectra*, vol. 16, pp. 573–592, 2000.

[29] J.P. de Almeida, *LGCIV2042 Earthquake Engineering*, 2023.

[30] Joao Pachero de Almeida and Antõnio Correia, *Nonlinear Response Analysis*, 2023.

[31] A. Chopra, *Dynamics of Structures: Theory and Applications to Earthquake Engineering*. Civil Engineering and Engineering Mechanics Series, Prentice Hall, 2012.

UNIVERSITÉ CATHOLIQUE DE LOUVAIN
École polytechnique de Louvain
Rue Archimède, 1 bte L6.11.01, 1348 Louvain-la-Neuve, Belgique | **www.uclouvain.be/epl**